



AFRL-RH-WP-TR-2009-0044

Biological Interactions of Nanomaterials

**Saber M. Hussain
Laura K. Braydich-Stolle
Janice L. Speshock
Kyung O. Yu
Amanda M. Schrand
Christin M. Grabinski
Nicole M. Schaeublin
Richard C. Murdock
Alicia B. Castle
Michael C. Moulton
Elizabeth I. Maurer
Cataleya NMI Carlson
Samantha J. Kunzelman
Krista L. Hess
Rochelle L. Jones**

**Biosciences and Protection Division
Applied Biotechnology Branch**

December 2008

Final Report for October 2007 – November 2008

•
•

Approved for public release;
Distribution unlimited.

**Air Force Research Laboratory
711th Human Performance Wing
Human Effectiveness Directorate
Biosciences and Protection Division
Applied Biotechnology Branch
Wright-Patterson AFB OH 45433**

NOTICE

Using Government drawings, specifications, or other data included in this document for any purpose other than Government procurement does not in any way obligate the U.S. Government. The fact that the Government formulated or supplied the drawings, specifications, or other data does not license the holder or any other person or corporation; or convey any rights or permission to manufacture, use, or sell any patented invention that may relate to them.

This report was cleared for public release by the 88th Air Base Wing Public Affairs Office and is available to the general public, including foreign nationals. Copies may be obtained from the Defense Technical Information Center (DTIC) (<http://www.dtic.mil>).

AFRL-RH-WP-TR-2009-0044

THIS REPORT HAS BEEN REVIEWED AND IS APPROVED FOR PUBLICATION IN
ACCORDANCE WITH ASSIGNED DISTRIBUTION STATEMENT.

//SIGNED//

SABER M. HUSSAIN, Work Unit Manager
Applied Biotechnology Branch

//SIGNED//

MARK M. HOFFMAN, Deputy Chief
Biosciences and Protection Division
Human Effectiveness Directorate
711th Human Performance Wing
Air Force Research Laboratory

This report is published in the interest of scientific and technical information exchange, and its publication does not constitute the Government's approval or disapproval of its ideas or findings.

REPORT DOCUMENTATION PAGE				Form Approved OMB No. 0704-0188	
<small>Public reporting burden for this collection of information is estimated to average 1 hour per response, including the time for reviewing instructions, searching data sources, gathering and maintaining the data needed, and completing and reviewing the collection of information. Send comments regarding this burden estimate or any other aspect of this collection of information, including suggestions for reducing this burden to Washington Headquarters Service, Directorate for Information Operations and Reports, 1215 Jefferson Davis Highway, Suite 1204, Arlington, VA 22202-4302, and to the Office of Management and Budget, Paperwork Reduction Project (0704-0188) Washington, DC 20503.</small>					
PLEASE DO NOT RETURN YOUR FORM TO THE ABOVE ADDRESS.					
1. REPORT DATE (DD-MM-YYYY) December 2008		2. REPORT TYPE Final		3. DATES COVERED (From - To) 1-Oct-07 – 30-Nov-08	
4. TITLE AND SUBTITLE Biological Interactions of Nanomaterials				5a. CONTRACT NUMBER In-House	
				5b. GRANT NUMBER NA	
				5c. PROGRAM ELEMENT NUMBER 62202F	
6. AUTHOR(S) Saber M. Hussain, Laura K. Braydich-Stolle, Janice L. Speshock, Kyung O. Yu, Amanda M. Schrand, Christin M. Grabinski, Nicole M. Schaeublin, Richard C. Murdock, Alicia B. Castle, Michael C. Moulton, Elizabeth I. Maurer, Cataleya NMI Carlson, Samantha J. Kunzelman, Krista L. Hess, Rochelle L. Jones				5d. PROJECT NUMBER 2312	
				5e. TASK NUMBER A2	
				5f. WORK UNIT NUMBER 2312A214	
7. PERFORMING ORGANIZATION NAME(S) AND ADDRESS(ES)				8. PERFORMING ORGANIZATION REPORT NUMBER	
9. SPONSORING/MONITORING AGENCY NAME(S) AND ADDRESS(ES) Air Force Materiel Command Air Force Research Laboratory 711 th Human Performance Wing Human Effectiveness Directorate Biosciences and Protection Division Applied Biotechnology Branch Wright-Patterson AFB OH 45433-5707				10. SPONSOR/MONITOR'S ACRONYM(S) 711 HPW/RHPB	
				11. SPONSORING/MONITORING AGENCY REPORT NUMBER AFRL-RH-WP-TR-2009-0044	
12. DISTRIBUTION AVAILABILITY STATEMENT Approved for public release; distribution unlimited.					
13. SUPPLEMENTARY NOTES SAF/PAO cleared 28Jul09, SAF/PAO-09-0379. (88ABW-09-2629/AFMC-09-0093)					
14. ABSTRACT The Biological Interactions of Nanomaterials project focuses on biological characterization of nanomaterials of particular interest to the Air Force. This report describes the basic mechanism of biological interactions of engineered nanomaterials, and explains potential toxicities arising from physicochemical properties uniquely associated with nano-scale structures, including size, shape, surface charge, surface composition, and in some cases surface structure. This research acquired the fundamental knowledge needed to improve understanding of nano-bio interaction mechanisms and provided in-depth analyses of corresponding effects on biological systems. This knowledge will help to improve nanomaterial safety strategies for the protection of both human and environmental health, and help to apply advanced nanobiotechnology to the development of future weapon systems. As we end the Biological Interactions of Nanomaterials project, we look to the future to transition the knowledge gained during the time on this project toward applications, such as using nanomaterials to design biosensors for the detection of biomolecules. Detection may be accomplished at the intra-cellular levels, external to the body, or at any level in between. One of our future aims is to be able to exploit the unique properties of certain nanomaterials for the purpose of stand-off detection or control.					
15. SUBJECT TERMS Nanomaterials, toxicity, <i>in vitro</i>					
16. SECURITY CLASSIFICATION OF:			17. LIMITATION OF ABSTRACT SAR	18. NUMBER OF PAGES 127	19a. NAME OF RESPONSIBLE PERSON Saber M. Hussain
a. REPORT U	b. ABSTRACT U	c. THIS PAGE U			19b. TELEPHONE NUMBER (Include area code)

THIS PAGE INTENTIONALLY LEFT BLANK

TABLE OF CONTENTS

INTRODUCTION	1
General Background	1
Introduction by Study	1
Immune suppression in MRSA- infected human alveolar co-cultures treated with Al, Al ₂ O ₃ , and Al-OA nanoparticles	1
Crystal structure mediates mode of cell death in TiO ₂ nanotoxicity.....	2
The role of nanoparticle charge in gold nanotoxicity	3
Shape matters: Differential cytotoxicity observed in gold nanospheres and nanorods	4
Toxicity of amorphous silica nanoparticles in mouse keratinocytes	4
Unique cellular interaction of silver nanoparticles: Size dependent generation of reactive oxygen species.....	4
Silver nanoparticles disrupt GDNF signaling in spermatogonial stem cells independent of nanoparticle size and coating	5
Characterization and biocompatibility of “green” synthesized silver nanoparticles	6
<i>In vitro</i> biocompatibility of silver nanoparticles anchored on multi-walled carbon nanotubes	7
Biocompatibility of carbon foam substrates for osteoblast growth	8
MATERIALS AND METHODS.....	9
General Background	9
Nanomaterial characterization	9
Characterization of biological interactions with Nanomaterials.....	10
Materials and Methods by Study	11

Immune suppression in MRSA- infected human alveolar co-cultures treated with Al, Al ₂ O ₃ , and Al-OA nanoparticles	11
Crystal structure mediates mode of cell death in TiO ₂ nanotoxicity.....	11
The role of nanoparticle charge in gold nanotoxicity	12
Shape matters: Differential cytotoxicity observed in gold nanospheres and nanorods	12
Toxicity of amorphous silica nanoparticles in mouse keratinocytes	12
Unique cellular interaction of silver nanoparticles: Size dependent generation of reactive oxygen species.....	13
Silver nanoparticles disrupt GDNF signaling in spermatogonial stem cells independent of nanoparticle size and coating	13
Characterization and biocompatibility of “green” synthesized silver nanoparticles	16
<i>In vitro</i> biocompatibility of silver nanoparticles anchored on multi-walled carbon nanotubes	17
Biocompatibility of carbon foam substrates for osteoblast growth	18
RESULTS AND DISCUSSION	19
Results by Study	19
Immune suppression in MRSA- infected human alveolar co-cultures treated with Al, Al ₂ O ₃ , and Al-OA nanoparticles	19
Crystal structure mediates mode of cell death in TiO ₂ nanotoxicity.....	28
The role of nanoparticle charge in gold nanotoxicity	37
Shape matters: Differential cytotoxicity observed in gold nanospheres and nanorods	43
Toxicity of amorphous silica nanoparticles in mouse keratinocytes	50
Unique cellular interaction of silver nanoparticles: Size dependent generation of reactive oxygen species.....	56

Silver nanoparticles disrupt GDNF signaling in spermatogonial stem cells independent of nanoparticle size and coating	60
Characterization and biocompatibility of “green” synthesized silver nanoparticles	71
<i>In vitro</i> biocompatibility of silver nanoparticles anchored on multi-walled carbon nanotubes	79
Biocompatibility of carbon foam substrates for osteoblast growth	84
CONCLUSIONS.....	86
BIN TRANSITIONS AND FUTURE WORK.....	88
External control of bio-functionalized nanoparticles for control of cell processes and signaling.....	88
Modulation of the immune system using electromagnetic nanoparticles: Potential application to reverse sleep deprivation and increase human performance.....	92
REFERENCES	98
LIST OF ABBREVIATIONS.....	107

LIST OF FIGURES

1. Aluminum nanoparticle characterization	19
2. Cell viability in the alveolar cells when cultured separately	20
3. Cell viability in the lung co-cultures following exposure to the aluminum nanoparticles	21
4. Phagocytic activity of human macrophages following exposure to aluminum nanoparticles and the bacteria MRSA	22
5. NFκB gene expression after treatment with aluminum nanoparticles and exposure to MRSA.....	23
6. Activation of inflammatory response genes following exposure to aluminum nanoparticles and MRSA.....	24
7. Activation of apoptotic genes after exposure to aluminum nanoparticles and MRSA.....	25
8. Secretion of pro-inflammatory cytokines from the lung co-cultures exposed to MRSA in the presence of aluminum nanoparticles	26
9. Secretion of anti-inflammatory cytokine IL-8 from the lung co-cultures exposed to MRSA in the presence of aluminum nanoparticles	27
10. Secretion of chemokine IL-10 from the lung co-cultures exposed to MRSA in the presence of aluminum nanoparticles	27
11. TEM images of the titanium dioxide nanoparticles.....	29
12. Uptake and localization of titanium dioxide nanoparticles in mouse keratinocytes.....	31
13. Cell proliferation in mouse keratinocytes treated with titanium dioxide nanoparticles	32
14. Membrane leakage in mouse keratinocytes treated with titanium dioxide nanoparticles	33
15. Acellular reactive oxygen species formation in titanium dioxide particles.....	34
16. Reactive oxygen species production in mouse keratinocytes treated with titanium dioxide particles	35
17. Cell proliferation in mouse keratinocytes treated with titanium dioxide nanoparticles and the antioxidant N-Acetyl-L-Cysteine	36

18. CytoViva images of gold nanoparticles in HaCaT cells	38
19. Cell proliferation in HaCaT cells treated with various gold nanoparticles for 24 hours	39
20. Membrane leakage in HaCaT cells treated with various gold nanoparticles for 24 hours	40
21. ROS generated in HaCaT cells treated with various gold nanoparticles for 24 hours	41
22. Changes in gene expression of DNA damage genes after 24h exposure to 1.5 nm Au nanoparticles.....	42
23. TEM images of the nanospheres	43
24. TEM images of the gold nanorods	44
25. CytoViva images of gold nanospheres	45
26. CytoViva images of gold nanorods.....	46
27. Cell viability after 24 hour exposure to Au nanospheres.....	47
28. Cell proliferation in HaCaT cells after 24 hour exposure to Au nanorods	47
29. Membrane leakage in HaCaT cells after 24 hour exposure to Au nanospheres	48
30. Membrane leakage in HaCaT cells after 24 hour exposure to Au nanorods	48
31. ROS generated in human keratinocytes after 24 hour exposure to Au nanospheres	49
32. ROS generated in human keratinocytes after 24 hour exposure to Au nanorods	49
33. Transmission electron microscopy of SiO ₂ spheres.....	51
34. The average particle size (<i>d</i>) and the standard deviation determined using TEM by analyzing over 300 particles	51
35. Transmission electron microscopy of HEL-30 cells incubated with 100 µg/mL of silica nanoparticles for 24 hours showing internalization of all sizes used in this study	52
36. Effect of SiO ₂ on LDH leakage into media (% control)	53
37. Effect of silica nanoparticles on MTT reduction (% control).....	54
38. Correlation between LDH and MTT in various sizes of silica nanoparticles at 200 µg/mL ..	54
39. Effect of silica nanoparticles on GSH levels (% control)	55

40. Time course study of effect of silica nanoparticles on ROS formation (fold of increase compared with the control).....	56
41. Effect of Ag and TiO ₂ nanoparticles on mitochondrial function in macrophages.....	57
42. Effect of Ag nanoparticles on membrane integrity in macrophages.....	57
43. Effect of Ag nanoparticles on reactive oxygen species generation in macrophages	58
44. Assessment of mitochondrial membrane potential in macrophages.....	59
45. Qualitative assessment of macrophages exposed to silver to distinguish normal cells versus apoptotic cells by confocal microscopy	59
46. Characterization data for the Ag 25-HC and Ag 10-PS.....	61
47. Characterization of Ag-HC and Ag-PS nanoparticles.....	63
48. Demonstration of surface binding, internalization, and localization of Ag nanoparticles by germ-line stem cells.....	66
49. Proliferation of C18-4 cells treated with coated silver nanoparticles	67
50. Effect of silver nanoparticles on the extracellular components of the GDNF signaling pathway	68
51. Fyn kinase phosphorylation and activation in the presence of coated silver nanoparticles....	69
52. Mechanism of GDNF disruption by silver nanoparticles in C18-4 cells.....	70
53. Epinephrine synthesized Ag nanoparticle cytotoxicity assays in MAC and HaCaT cell lines	73
54. Tea Extract synthesized Ag nanoparticle cytotoxicity assays in MAC and HaCaT cell lines leakage.....	74
55. Cyto viva images of MAC cell interactions with Ag nanoparticles	75
56. Cyto viva images of HaCaT cell interactions with Ag nanoparticles.....	76
57. Cyto viva images of MAC cell interactions with Ag nanoparticles in MAC cells	77
58. Cyto viva images of HaCaT cell interactions with Ag nanoparticles in MAC cells	78
59. SEM images (A, B, D, E, G, H) and particle size determined via DLS (C, F, I)	79
60. CNx-MWNTs/Ag-S composite characterization.....	80

61. X-ray diffraction patterns of CNTs/Ag composites	80
62. TEM images of MWNTs/Ag composites	81
63. MTS results	82
64. Control HaCaT cells at different time points	83
65. Exposed cells at different time points	83
66. Osteoblast growth on carbon foams imaged via SEM	84
67. Fluorescent images of osteoblasts on carbon foam	85
68. Mitochondrial function of human fetal osteoblasts as a measure of cell viability	85
69. Color shift observed with increasing agglomeration of Au NPs	88
70. Gold NPs functionalized with aptamers	89
71. Representation of nano-biocontrol project	90
72. Magnetic field lines for a solenoid	90
73. The stimulatory and inhibitory receptors on the surface of NK cells and the signaling pathways involved with their activation	95
74. FcR receptor mediated phagocytosis and the effects on gene expression and inflammatory cytokine production	96

LIST OF TABLES

1. Methods for Characterizing Nanoparticles	9
2. Methods for Characterizing Biological Interactions with Nanomaterials	10
3. Titanium Dioxide Nanoparticle Diameter, Composition, and Source	28
4. Titanium Dioxide Nanoparticle Characterization in Solution	30
5. Compilation of Nanomaterial Characterization and Cellular Assay Data	36
6. List of DNA Damage Genes Up and Down-Regulated and Their Functions	42
7. Gold Nanospheres with Different Ligands and Their Concentrations.....	43
8. Gold Nanorods with Different Ligands and Their Concentrations.....	43
9. Particle Sizes of Silicon Dioxide in Water and Dosing Media	50
10. Nanoparticle Parameters Used to Determine Dosing Metric.....	65
11. “Green” Synthesized Nanoparticles with Their Average Sizes as Powders and in Different Dispersants	72
12. Ag Particle Size on Different Types of CNTs	81

SUMMARY

The Biological Interactions of Nanomaterials (BIN) project focuses on biological characterization of nanomaterials of particular interest to the Air Force. This report describes the basic mechanism of biological interactions of engineered nanomaterials, including potential toxicities arising from the physicochemical properties uniquely associated with nano-scale structures. Two key areas of immediate military relevance include propulsion and munitions systems, where there is a growing need for nanoenergetics and other novel technologies to satisfy the increasing performance demands. This research acquired the fundamental knowledge needed to improve understanding of nano-bio interaction mechanisms and provided in-depth analyses of corresponding effects on biological systems. The transition from 6.1 to 6.2 research will yield development not only of theoretical predictive bioresponse models, but of nanobiotechnology tools such as biosensors. This knowledge will help to improve nanomaterial safety strategies for the protection of both human and environmental health, and help to apply advanced nanobiotechnology to the development of future weapon systems. The technology is transitioning into development of a database, the web-interfaced nanotechnology environmental, safety and health (ESH) guidance system, for predicting health effects in operational scenarios. The USAF Aeronautical System Center (ASC) has shown great interest in utilizing such a database. This program transitioned into Air Force 711 HPW/RH, also interested in using this knowledge to develop nano-biosensors. This program also transitioned into the AFRL-NST program to develop tools to address Environment and Health Effects of Nanoenergetics.

Research objectives regarding the BIN project are as follows:

- Identify the exposure concentrations of nanoparticles that are lethal to specific cell types representing the liver and immune system, as well as the cellular effects generated post-exposure.
- Assess the cellular mechanisms generated from exposure to these nanoparticles at non-lethal doses, which is more representative of an occupational exposure.
- Collaborate with the AFOSR Multidisciplinary Research Initiative (MURI) Nanotoxicology Group to build a comprehensive foundation to efficiently predict the multiple biologic effects that nanomaterials assert on living organisms.

THIS PAGE INTENTIONALLY LEFT BLANK

INTRODUCTION

General Background

Currently, the field of nanotechnology is growing at an exponential rate and engineered nanomaterials are being incorporated into all aspects of life. Nanomaterials, which demonstrate one dimension in 1-100 nm range, possess novel physical and chemical properties that have been used or are proposed to be used to create unique devices [1]. In medicine, proposed uses for nanomaterials include: drug delivery, imaging, and the formation of bone composites [2-5]. Furthermore, companies in the food and cosmetics industries have incorporated nanomaterials to enhance the quality of their products [6]. Most importantly, these nano scale materials will be useful for military applications such as portable battlefield remote devices to monitor, control and improve soldier performance, munitions, and energetic/reactive systems involved with the advancement of propulsion technology [7].

Unique quantum properties of nanomaterials strongly influence their physico-chemical properties, conferring electrical, optical and magnetic properties not present in corresponding bulk materials at a larger scale. For example, nanomaterials have a much larger surface area to volume ratio than their larger corresponding particle therefore making them more reactive. This change in surface area is just one of the many ways that the nanoparticle (NP) can affect biological interactions. Other features of NPs to take into consideration include size, shape, aggregation, solubility and surface chemistry (charge). These properties are dependent on the method of synthesis, environment and sample preparation and can vary from batch to batch. Thus all NPs are not created equal.

Recent observations in biological systems suggest that the physical parameters of NPs can affect their nonspecific uptake in cells, with potential to induce cellular responses. However, it is not known how engineered NPs of different size, structure, shape and geometries interact with cells and the molecular events involved in NP– membrane receptor binding, endocytosis and subsequent signaling activation. The following studies demonstrate the effect of nanomaterial properties on toxicity and provide insight into the mechanisms through which cells interact with nanomaterials.

Introduction by Study

Immune suppression in MRSA- infected human alveolar co-cultures treated with Al, Al₂O₃, and Al-OA nanoparticles

There were two main objectives for the BIN group this past year, including 1) to standardize characterization methods for biological testing of NPs using aluminum as benchmark material and 2) to complete development of *in vitro* models for toxicity testing. The first objective was addressed by extensively characterizing nanomaterials prior to and during exposure using various characterization techniques, which will be described in the Materials and Methods section. In addition, dispersion agents were varied to study the effect that a solvent has on NP size and toxicity. Because aluminum-based NPs are commonly used in jet fuels and munitions, the second objective was achieved by using the human alveolar epithelial cell line, A549, and the human alveolar macrophage cell line, U937, as an *in vitro* model for inhalation.

The type I epithelial cells are responsible for forming the structure of the alveoli, and the macrophages are the immune cells which protect the epithelial cells. They are also type II cells which are responsible for secreting a pulmonary surfactant. To mimic the alveoli microenvironment the A549 epithelial cells were co-cultured with the U937 cells in a 3:1 (A549:U937) ratio and dispersed the NPs in an artificial lung surfactant prior to exposure [8,9]. Once the toxicity of the NPs was determined using viability assays, a low non-toxic concentration of NPs was selected for future studies. Since the immune cells in the lung protect the epithelial cells, the co-cultures were exposed to aluminum NPs and then infected with bacteria and changes in gene expression and cytokine secretion were assessed. The bacteria we chose to study were the USA 300 community-associated Methicillin-resistant *Staphylococcus aureus* (MRSA) because it is a respiratory pathogen, and military recruits were identified by the Centers for Disease Control as one of the “at-risk” groups for this type of infection [10]. MRSA causes necrotizing pneumonia, necrotizing fasciitis, and toxic shock syndrome in otherwise healthy individuals.

Crystal structure mediates mode of cell death in TiO₂ nanotoxicity

One of the key nanomaterials that has been immersed in the market place is titanium dioxide (TiO₂). When TiO₂ is synthesized in the NP form, these materials have properties of high transparency to visible light and high ultra-violet (UV) absorption, and some components of visible light are reflected and refracted differentially, which leads to an iridescent quality. These properties have generated widespread use of TiO₂ in products such as pearlescent or “metallic” paint formulations used in cosmetics, hard coatings, plastics, and self-cleaning additives for porcelain, ceramics, and specialty coatings. Other TiO₂ applications include filters that exhibit strong germicidal properties and remove odors, and TiO₂ has been used in conjunction with silver as an anti-microbial agent [11]. Furthermore, due to its photocatalytic activity, TiO₂ has been used in waste water treatments. This photocatalytic activity is influenced by the crystal structure (anatase and/or rutile), surface area, size distribution, porosity, surface, and hydroxyl group density [12].

TiO₂ occurs in four forms, but the two main crystal structure forms, which occur naturally and are used in industry, are anatase and rutile [12]. Nanotoxicity studies examining the effects of TiO₂ have shown induction of inflammatory responses, cytotoxicity, and reactive oxygen species (ROS) formation in a variety of cell types and tissues [13-18]. However, these early nanotoxicity studies have yielded conflicting data which identify either size or crystal structure as the mediating property for nano-TiO₂ toxicity. Ultrafine TiO₂ particles (29 nm) increased inflammation and altered macrophage chemotactic responses in rat lungs, when compared to TiO₂ particles that were 250 nm [13]. In addition, TiO₂ particles induce oxidative damage in a human bronchial epithelial cell-line in a size dependent manner [27]. In contrast, other studies have shown that exposure to nanoscale TiO₂ rods/dots produced inflammatory responses that were not different from pulmonary effects of larger TiO₂ particles in rats, and that composition of nanoscale titania correlates to cytotoxicity, with the anatase TiO₂ being more toxic than the rutile TiO₂ [14,16]. However, it is important to note that none of these studies examined size with the crystal structure composition controlled for or examined crystal structure while controlling the size. In the study by Renwick et al. [13], the crystal structure composition of the two different types of TiO₂ particles is not identified, and in the study by Gurr et al. [17], three of the particles are anatase while the fourth is rutile. In the study by Warheit et al. [14], which contradicted the size dependent study, 300 nm rutile NPs were compared to TiO₂ rods that

were 200 nm x 35 nm and 10 nm anatase dots. The size and shape of these materials were not controlled for both of which are defined as characteristics which need to be evaluated prior to toxicity studies, therefore, an accurate crystal structure assessment cannot be made [19-22]. Additionally, the study by Sayes et al. [16] did not consider size based on the formation of aggregates, yet Nel and colleagues identified aggregates as one of the biokinetic properties of nanomaterials that must be taken into consideration [22].

The goal of this study was to evaluate the role of size in TiO₂ nanotoxicity with NPs composed of the same crystal structure and to evaluate crystal structure in TiO₂ nanotoxicity with NPs of a similar diameter. We chose to use the a mouse keratinocyte cell-line (HEL-30) as a model for dermal exposure since nano-TiO₂ is used in cosmetics and sunscreens. In the size dependent studies, all the NPs are 100 percent anatase and aggregate sizes were determined in order to take into account the effect of agglomeration on size dependent toxicity. In addition, varying crystal structures were assessed while the size of the particles was controlled.

The role of nanoparticle charge in gold nanotoxicity

A multitude of NPs are being examined for biomedical probes in applications such as purification, sensing, imaging, and drug delivery. One main metal that has been typically used in the field of medicine is gold (Au). Gold has been used for its healing properties for over 5,000 years. The earliest uses date back to the Chinese in 2500 B.C. who used it to cure any number of ailments. The ancient Egyptians used gold in dentistry and ingested it for mental, spiritual and bodily purification, and gold salves were used in ancient Rome to treat skin diseases. The famous medieval German physician and alchemist Paracelsus developed a gold colloidal solution that he called “aurum potable” that he claimed was a cure all of all illness. Today gold is still widely used in the medical field, mostly in the form of NPs. Specifically, gold NPs are being used as novel gene and drug-delivery agents to kill cancer cells, as a contrast agent in medical imaging, and as biological sensors.

There are conflicting reports on the toxicity of gold NPs. For example, Shukla et al. [23] show that 3.5 nm gold NPs are non-toxic to macrophages and do not initiate stress-induced secretions of pro-inflammatory cytokines TNF α or IL-1 β , and Connor et al. [24] also show gold NPs (4, 12, and 18 nm with different surface-modifications) are non-toxic to human cells. Murphy et al. gave a good review of other studies that show gold NP biocompatibility [25]. However, Pan and colleagues [26] recently published a study demonstrating a size dependant toxicity of gold NPs with 1.4 nm particles being the most toxic and Pernodet and co-workers [27] illustrate that 14 nm gold particles cause abnormal actin and extracellular matrix in dermal fibroblasts. These abnormal proteins in turn cause a major decrease in cell proliferation, adhesion and motility. Lastly, Goodman et al. [28] have shown that the charge of the NP also plays a role in toxicity. Their studies show cationic gold NPs to be moderately toxic, while anionic gold NPs of the same size are non-toxic. Clearly, these conflicting results show that more work needs to be done in this field on any NP that is being considered for use in the human body.

This study was designed to determine the biocompatibility of gold NPs using human keratinocyte cell-line (HaCaT) as a model. We evaluated the cytotoxicity of gold NPs with different ligands (MEEE which makes the particles neutral, MES which makes the particles anionic, and TMAT which makes the particles cationic) with diameters of 0.8 nm, 1.5 nm and 10 nm.

Shape matters: Differential cytotoxicity observed in gold nanospheres and nanorods

Gold NPs are being used in sensing, imaging, and treatment of certain cancers and as novel gene and drug delivery agents due to their unique physical and chemical properties. Despite being easily accessible and found in a wide range of consumer products, the cytotoxicity of these nanomaterials has not been thoroughly examined. Many of the unique properties that must be evaluated prior to making claims of biocompatibility are size, surface area, morphology, shape, surface charge, and crystal structure. The majority of nanotoxicity studies have focused on size and very few have assessed the role that shape plays in determining NP toxicity. This study evaluated the cytotoxicity of gold NPs with different shapes. Gold nanorods 51 nm in length with varying diameters were compared to gold nanospheres 12 nm in size and toxicity was assessed in the HaCaT cell-line. Cells were treated with varying concentrations (0-100 $\mu\text{g/mL}$) of the gold nanomaterials for 24 h, and biocompatibility was tested using cell viability, membrane integrity, and ROS as endpoints.

Toxicity of amorphous silica nanoparticles in mouse keratinocytes

Silica (silicon dioxide, SiO_2) NPs demonstrate great practical importance in the fabrication of electric and thermal insulators, catalyst supports, drug carriers [29], gene delivery [30], and coating processes, and are also used as adsorbents, molecular sieves, and filler materials [31]. Colloidal silica crystals with periodicity within the optical wavelength scales also have a photonic band gap and thus have electronic applications ranging from microwave to optical devices [32]. The interests of silica ordered particle arrays lie in the fact that it is possible to induce wavelength coalescence with the close packed structure. These particle arrays can diffract light in the UV, visible and near infrared regions in a manner analogous to x-ray diffraction (XRD) from ordinary mineral crystals [32-33]. Many aspects related to the size of these materials have raised safety concerns during production, their use in consumer products and their eventual deposition into the environment. These aspects include biological availability, kinetics and dynamics of movement, and their general acute and chronic effects. Though many engineered NPs could provide benefits to society, their interaction with biological system and potential toxic/bioeffects are not well addressed [34-37].

NPs can enter the body via different routes such as the gastrointestinal tract [38], lungs [39-40], and passage through skin [21]. The epidermis, is an excellent barrier to protect the body from external insult, however NPs can penetrate through the broken or flexed skin [21]. NPs such as TiO_2 or ZnO in sun screens can penetrate the human stratum corneum and into some hair follicles, but not in deep layer of skin. Therefore, although the skin has been reported as non-permeable to allow passage to the organism [31,41], the skin and its cellular components do retain the full burden of the nanoparticulate exposure. The objective of this study was to illustrate the acute effects of well-dispersed and different sizes of silica NPs in upper layers of the skin using mouse skin epidermal cells or keratinocytes. The objective of this study was to illustrate the acute effects of well dispersed and different sizes of silica NPs in a mouse keratinocyte cell-line (HEL-30). These particles were studied for determining cellular uptake, changes in mitochondria-based viability, membrane leakage, and oxidative stress.

Unique cellular interaction of silver nanoparticles: Size dependent generation of reactive oxygen species

Recent studies have demonstrated the importance of silver NPs for anti-microbial uses [42-44]. Silver NPs in the sub-50 nanometer range exhibit increased efficacy in killing a wide

range of bacteria and fungi. Although silver nanomaterials are currently widely utilized in modern technology, a concrete assessment concerning the human health and environmental implications of manufactured nanomaterials is lacking. Due to the strong affinity of silver with –SH groups [45], it is likely that nano-silver may pose a great potential threat to human health. The toxicity of silver exhibited in liver cells was shown to be mediated by oxidative stress [46]. In addition, silver NPs induced toxicity in germ line stem cells [47]. There is a tremendous lack of information on the basic toxicity of nano-sized silver and its interactions with cellular receptors, extra/intra-cellular proteins, organelles and DNA, which needs to be addressed. The major toxicological concern is derived from redox reactive nature of some manufactured nanomaterials [48] and their ability to cross cell membranes into critical organelles such as mitochondria [49].

In vivo exposure to NPs is likely to occur through inhalation, dermal contact, and ingestion. Deposition of inhaled particulate matter has been found to be dependent on size; consequently silver NPs are likely to have an effect on the deep regions of the lung; in specific, the alveolar region [50]. Therefore, in the present study rat alveolar macrophages were selected as a model cell line to assess the degree of toxicity and explore possible biomechanisms of toxicity after possible inhalation. Macrophages are generally a population of ubiquitously distributed mononuclear phagocytes responsible for numerous homeostatic, immunological, and inflammatory processes. Their primary function is to act as scavengers, roaming the lungs, engulfing foreign and potentially dangerous matter. Alveolar macrophages are known to be extremely effective in the clearance of foreign matter by internalizing particulates via phagocytosis and endocytosis [51,52]. The current study is designed to model NP exposure via inhalation by utilizing rat alveolar macrophages and provide a general evaluation of silver NP toxicity [53,54]. In addition, several cellular mechanisms stemming from NP-induced toxicity, including oxidative stress, inflammatory, and immunological responses were evaluated.

Silver nanoparticles disrupt GDNF signaling in spermatogonial stem cells independent of nanoparticle size and coating

Silver is unique among antimicrobial agents in that it has a broad spectrum of action against approximately 650 different types of disease-causing organisms [55,56]. Current antimicrobial uses include coating of wound dressings and catheters with silver, which effectively reduces bacterial infections [57,58]. While this metal is non-toxic to humans and animals in its bulk chemical form [56], it is unclear what impact nano-sized silver has on biological systems. With the advancement of nanotechnology, silver NPs have been synthesized and shown to be effective antimicrobial agents due to their ability to bind to proteins and interfere with bacterial and viral processes [59,60]. Therefore, nano-sized silver has found antimicrobial uses in bandages, in coatings on clothing and other surfaces, and in paints [55-68]. Perhaps one of the most interesting potential applications is the ability of silver NPs to bind to HIV-1 and prevent the virus from infecting host cells [64]. Because silver NPs bind with high affinity to proteins and glycoproteins, the cellular interactions of these NPs with human tissues must be considered.

Because the production of viable sperm is essential for a species to produce offspring, the germ cells of the testis must be protected from damage. Spermatogenesis is a complex process that is highly sensitive to environmental injury [69]. Much like brain cells are protected by the blood-brain barrier, the cells of the germ-line are protected by a blood-testis barrier [70-75], which NPs are capable of penetrating [76]. We have recently demonstrated that mammalian

spermatogonial stem cells are particularly sensitive to silver NPs (15 nm), which induce a significant decline in their proliferation. The molecular mechanisms leading to this decrease are not known, although membrane leakage and apoptosis generally appear with metal NP concentrations higher than 10 $\mu\text{g/mL}$ [77].

The growth factor glial cell line-derived neurotrophic factor (GDNF) is essential for spermatogonial stem cell self-renewal *in vivo*, and mice over expressing GDNF develop germ cell tumors, while GDNF-null mice show depletion of spermatogonial stem cells [78]. In addition, GDNF also promotes spermatogonial stem cell proliferation *in vitro* via the Src family kinase (SFK)/phosphoinositide 3 (PI3)-kinase/Akt pathway [79-84]. Because NPs can directly interact with proteins [85], we sought to examine whether silver NPs at concentrations considered non-cytotoxic in standard assays can interact with components of the GDNF signaling pathway in spermatogonial stem cells, thus elucidating the molecular basis of growth inhibition. Several studies have shown that altering the surface chemistry of NPs is effective in preventing toxicity from the core nanomaterial [86-91].

In this study, we also have evaluated the role of size and surface chemistry in the biological interactions of silver NPs. We used silver NPs of different sizes and surface coatings, such as hydrocarbon-coated silver (Ag-HC) NPs of 15 nm, 25 nm, and 80 nm diameters, and polysaccharide-coated silver (Ag-PS) NPs of 10 nm, 25-30 nm, and 80 nm diameter. Ag 130 nm particles were used as a control. The polysaccharide coating was used to promote a better dispersion of the NPs and to make them more biocompatible [92].

Characterization and biocompatibility of “green” synthesized silver nanoparticles

Nanostructured noble metals have found widespread use in several technological applications [93-97] and various methods have been exploited to meet the demands [98-105]. Synthesizing metal and semiconductor NPs is gaining interest due to their extraordinary properties which differ from when they are in bulk and recently, there is a renewed interest in applying green chemistry principles in producing the same [25,106-116]. For example, silver and gold NPs produced from vegetable oil can be used as antibacterial paints [116]. Green chemistry is the design, development, and implementation of chemical products and processes to reduce or eliminate the use and generation of substances hazardous to human health and the environment [117]. Strategies to address mounting environmental concerns with current approaches include the use of environmentally benign solvents, biodegradable polymers, and nontoxic chemicals. In the synthesis of metal NPs by reduction of the corresponding metal ion salt solutions, there are three areas of opportunity to engage in green chemistry: (i) choice of solvent, (ii) the reducing agent employed, and (iii) the capping agent (or dispersing agent) used. In this area, there has also been increasing interest in identifying environmentally friendly materials that are multifunctional. For example, the tea used in this study functions both as a reducing and capping agent for Ag nanospheres. In addition to its high water solubility, low toxicity, and biodegradability, tea is the most widely used behaviorally active drug in the world. However, until recently [118], there are no reports on the preparation of noble metals using tea extract.

With the growing concerns on the biological and environmental impacts of nanomaterials, the focus of creating nontoxic, “green” NPs has increased significantly [92-96]. It is well known that the ancient Greeks and Romans took advantage of silver’s anti-microbial effects and used silver particles to fight infections. Our previous studies have indicated that silver NPs have a size dependent cytotoxicity where the smaller particles are the most toxic; in

addition, the mechanism of toxicity is ROS [99]. Furthermore it has been shown that silver NPs exhibit an increase in cytotoxic effects with increased concentrations [25]. However, it has also been shown that surface modifications of silver NPs can dramatically alter the toxicity [100]. Therefore, the goal of this study was to synthesize biocompatible and environmentally friendly silver NPs and test their cytotoxicity. We chose to use rat alveolar macrophages (MACs) and HaCaT as *in vitro* models of exposure.

In-vitro biocompatibility of silver nanoparticles anchored on multi-walled carbon nanotubes

Biological functionalization of nanomaterials has come to be of significant interest in the recent years due to the potential for developing sensitive imaging and signaling pathway detection systems [119] as well as possible drug delivery systems [120]. The biofunctionalization of nanomaterial surfaces can result in aqueous soluble materials which can be further modified with active molecules making them compatible, active, specific capture field agents and useful in the biological systems.

One NP with possible use in functionalization is silver (Ag). Nano-silver possesses a high extinction coefficient, high surface plasmon resonance and anti-microbial properties which are less toxic than the bulk form [121,90]. Silver nanomaterials have shown a variety of uses in everyday consumer's lives such as: nanosilver infused storage containers [122], nanosilver coated surfaces of medical devices to reduce hospital related infections [123], bandages [124], footwear [125], and countless household items which claim to be anti-microbial. Nanosilver is a popular additive in many health products as listed above due to its unique ability to fight infectious diseases, slow the growth of bacterium, mold and germs. While all of these properties appear to make nanosilver the new "wonder-drug" of the nanotechnology world, problems arise. The problem with nanosilver is it has been shown to be toxic in a size dependent manner according to Carlson et. al [126]. The toxicity in the size dependent manner is shown to be due to ROS production. In the treatment of Macs, the toxicity is size and dose dependent with the most toxicity occurring with Ag 15 nm followed by Ag 55 nm and Ag 130 nm. It was also found that the smaller sizes (Ag 15-30 nm) caused decreases in mitochondrial function and membrane integrity. A decrease in the membrane integrity allows the leakage of the ROS outside the cell leading to apoptosis [126]. Toxicity of silver NPs is believed to be due to the strong affinity of silver to thiol groups [45]. Silver has also been shown to interact with DNA and cause it to lose its ability to replicate [127], which shows another possible mechanism for the toxicity of silver NPs.

In an effort to make silver NPs less toxic Schrand et. al. studied the toxicity of the silver NPs with a polysaccharide coating. The polysaccharide coated particles show less agglomeration and it is therefore easier to get into the cells. The N2A (neuronal) cells show greater reduction in viability in the Ag 25 uncoated particles versus the Ag 25 polysaccharide coated particles; therefore determining the coating reduces the toxicity of the Ag NPs. Overtime the coating dissolves in the body again rendering the cell to the toxic properties of the silver NPs [128].

In order to use the therapeutic properties of the silver NPs they need to be determined non-toxic. One possible method for reducing the toxicity of silver NPs is to functionalize them on multi-walled carbon nanotubes (MWCNT). Multi-walled carbon nanotubes consist of multiple layers of graphite rolled up to form a tube with a length to diameter ratio greater than 1,000,000. Two models exist for MWCNT, including the Russian Doll Model and the Parchment model. The Russian doll model consists of concentric graphite cylinders placed one

inside of the next. The parchment model is a sheet of graphite rolled up such as in a parchment scroll. Carbon nanotubes have many distinct properties such as strength 10-100 times greater than the strongest steel, but with a fraction of the weight due to sp^2 bonds. They also possess exceptional thermal and electrical properties making them useful for several devices such as field-emission displays [129], microscopy [130], microelectronics [131] and possibly drug delivery [120].

Multi-walled nanotubes have the possibility for use in drug delivery systems due to their chemical structure and unique ability to be functionalized. Functionalization of single walled nanotubes (SWCNT) leads to breakage of C=C bonds leaving holes in the structure causing changes in properties of the nanotubes. Unlike the SWCNTs, MWCNTs do not have bond breakage and therefore there are no holes in the tube and they maintain their unique properties. Along with losing their chemical properties SWCNTs have shown toxicity in HaCaT cells [132]. Upon exposure to the SWCNTs, the HaCaT cells showed an increase in oxidative stress as well as morphological changes, which are attributed to the iron catalyst within the SWCNT. The response of the keratinocytes to the SWCNTs is similar to dermatological disorders including pigmentation changes, inflammation, porphyrias and some skin cancers and is often referred to as carbon fiber dermatitis.

Information about the dermal toxicity of MWCNTs is unknown and contradictory at this time. However, MWCNTs have been shown to be biocompatible with neuronal cells such as in the study by Hu et al. [133]. This study demonstrated the ability of astrocytes to bind to the tubes leading to a reduction in scar tissue normally found with the implantation of neuronal devices. Biocompatibility of MWCNTs has also been shown in osteoblasts. A study by Elias et al. [134] showed osteoblasts were able to proliferate at higher rates on the nanotubes indicating a non-toxic possibility for bone regeneration.

A previous report about the toxicity of MWCNTs in mouse keratinocytes by Grabinski et al. showed high levels of ROS production upon exposure to MWCNTs [135]. The report also states the toxicity shown by the MWCNTs is likely due to the iron impurities found in the MWCNTs. Therefore, pure MWCNTs show promise for a biocompatible interaction with human keratinocytes. MWCNTs could be the answer to gaining the anti-microbial benefit of silver NPs. This study will determine if the functionalization of silver NPs on MWCNTs could be used in future drug delivery systems by delivering silver to the cell in a non-toxic, non-invasive method.

Biocompatibility of carbon foam substrates for osteoblast growth

Carbon is available in many forms, such as solid graphite, diamond, as well as nanotubes, nano-plates, and buckyballs. A relatively new structure currently being studied is microcellular carbon foam. It can be used in an array of applications such as heat exchangers, radiators, composite cores, as well as in products that require controlled electrical and thermal properties in porous materials. Though graphite is known to be a bio-compatible material, not much research has been done on the possibility of using microcellular foams as scaffolding for in-vitro tissue and cell growth. This study aims at investigating the influence of various surface topography and modifications on osteoblast and neuroblastoma cell-lines. Recent focus is on cell proliferation and viability on foam grafted with carbon nanotubes which may direct growth directions. This study will potentially lead to methods of speeding and controlling cell growth related to bio-sensing and tissue healing.

MATERIALS AND METHODS

General Background

Nanomaterial characterization

In recent years, it has become evident that it is necessary to systematically and accurately define particle characteristics in correlation to potential toxicity of NPs in a biological system to ensure that results are reproducible [1,8]. NP affects on biological activity are unknown at this point; therefore accurate characterization of these materials is essential to provide the basis for understanding the properties of NPs that determine their biological effects [9]. There are unique properties that lend themselves to nanomaterials and differentiate them from their bulk counterparts. However, the burden of testing the same parameters for bulk materials before conducting a nanotoxicity study would be overwhelming and costly to researchers. Therefore, certain characteristics have been identified which must be considered for the characterization of nanomaterials prior to study and these properties are: size, shape, dispersion, physical and chemical properties, surface area, and surface chemistry [9-12]. Many of these properties can be evaluated using dry, powdered nanomaterials, yet one question that remains is whether nanomaterials retain the same properties once in solution. This is a critical question that must be addressed because upon exposure, nanomaterials will come in contact with and potentially become dispersed in a variety of bodily fluids. Furthermore, in some cases, *in vitro* testing is used to determine the predictive toxicity of nanomaterials before proceeding to *in vivo* studies, and the nanomaterials must be dispersed in order to dose the cells. Characterization methods commonly used in recent studies to measure properties of both dry NPs and NPs dispersed in solution are listed in Table 1.

Table 1. Methods for Characterizing Nanoparticles

Material Property	Sample Type	Method	Instrument / Location
Size	NPs in solution	Dynamic Light Scattering (DLS)	Malvern Zetasizer Nano ZS / In-House
Surface charge	NPs in solution	Laser Doppler Velocimetry (LDV)	Malvern Zetasizer Nano ZS / In-House
Size, structure, morphology	Wet or dry NPs	Atomic Force Microscopy (AFM)	Veeco Bioscope II AFM / In-House
Size and morphology	Dry NPs	Transmission Electron Microscopy (TEM)	H-7600 Hitachi TEM / UD NEST
Size and morphology	Dry NPs	Scanning Electron Microscopy (SEM)	S-4800 Hitachi HRSEM / UD NEST
Absorption / Emission Spectra	Dry NPs	UV-Vis Spectroscopy	BioTek Synergie HT/ In-House
Composition	Dry NPs	Energy Dispersive Analysis using X-ray (EDAX)	Philips XL-30 eSEM / RX Zeiss EVO-50XVP eSEM / UD NEST

For DLS measurements using the the Malvern Zetasizer Nano ZS, the mean particle diameter is calculated by the software from the particle distributions measured, and the polydispersity index (PdI) given is a measure of the size ranges present in the solution [143]. The PdI scale ranges from 0 to 1, with 0 being monodisperse and 1 being polydisperse. The

software calculates the PdI value from the G1 correlation function and from parameters defined in the ISO standard document 13321:1996 E.

Characterization of biological interactions with nanomaterials

Once NPs are exposed to an *in vitro* model, it is necessary to assess the resulting biological interactions, including the effect of NP exposure on cellular function, uptake of NPs into cells, and interaction of the NPs with cell structures. Various biochemical assays and imaging methods are used to evaluate these responses. Methods most commonly used in recent studies are summarized in Table 2.

Table 2. Methods for Characterizing Biological Interactions with Nanomaterials

Material Property	Sample Type	Method	Instrument / Location
Size, structure, morphology, and uptake	Live or fixed cells	Atomic Force Microscopy (AFM)	Veeco Bioscope II AFM / In-House
Cell morphology and fluorescently tagged cellular structures / NPs	Live or fixed cells	Confocal (Spinning Disk) Microscopy	BD Biosciences Pathway 435 / In-House
Cell morphology and cellular structures / NPs (stained or unstained)	Live or fixed cells	Darkfield and Fluorescence Microscopy	CytoViva System with Dual Mode Fluorescence / In-House
Size, morphology, and uptake	Fixed cell sections	Transmission Electron Microscopy (TEM)	H-7600 Hitachi TEM / UD NEST
Size and morphology	Fixed cells	Scanning Electron Microscopy (SEM)	S-4800 Hitachi HRSEM / UD NEST
Absorbance and fluorescence	Biochemical assays on cells	Spectroscopy	SpectraMAX microplate readers and BioTek Synergy plate reader / In-House

Commonly tested biochemical endpoints include cell viability, cell membrane integrity, and oxidative stress. A common method of measuring cell viability is the MTS assay. MTS is a biochemical assay that measures the cell viability (based on mitochondrial function of the cell) using the reagent [3-(4,5-dimethylthiazol-2-yl)- 5-(3-carboxymethonyphenol)-2-(4-sulfophenyl)-2H-tetrazolium, inner salt], abbreviated as MTS. This assay is a colorimetric assay that measures the ability for cellular mitochondria to reduce a tetrazolium based chemical to a formazan salt.

The lactate dehydrogenase (LDH) assay is commonly used to evaluate cell membrane integrity. LDH is an enzyme that leaks out of the cell when the plasma membrane integrity is altered or disrupted. At the end of 24-h exposure, LDH levels in the media versus the cells are quantified and compared to control values using a multi-well plate format and a microplate reader (Molecular Devices, Sunnyvale, CA) at 340 nm according to the manufacturer's procedure.

Oxidative stress is commonly assessed by measuring the formation of ROS. In the ROS assay, cells are treated with fluorescent probe 2',7'-dichlorodihydrofluorescein diacetate (DCFH-DA) for 30 min under dark conditions before dosing the cells with NPs. After removing media, cells are exposed to the NPs and free radical production is tested by measuring the fluorescence of the cells in a multi-well fluorescence plate reader at excitation 485 nm and emission at 530 nm. Acellular ROS is measured using a modified assay to test for ROS using the previous

method without the presence of cells and using horseradish peroxidase (HRP) to mimic cellular enzymes.

For fluorescent imaging techniques, various fluorescent tags can be applied to live or fixed cells. Fluorescent tags will be described in the specific studies for which they were used. Materials and methods employed in each individual study are described in the following sections.

Materials and Methods by Study

Immune suppression in MRSA- infected human alveolar co-cultures treated with Al, Al₂O₃, and Al-OA nanoparticles

The first objective in this study was to develop a standard protocol for characterizing nanomaterials for biological studies. Aluminum-based NPs were extensively characterized prior to and during exposure using TEM to yield information on primary particle size and morphology, DLS to provide the size, and LDV for the charge of NPs in solution. Dispersion agents were varied to study the effect that a solvent has on NP size and toxicity. In particular, NP size was measured in an artificial lung surfactant to mimic exposure conditions. Aluminum NPs were synthesized by Dr. Chris Bunker's group with oleic acid (Al-OA). Previous aluminum studies had been performed by members in our group using aluminum oxide (Al₂O₃) and aluminum NPs from NovaCentrix so these NPs were also studied.

The second objective was to develop an *in vitro* model for toxicity testing in order to evaluate the effects of aluminum NPs on biological systems. Based on their uses in jet fuels and munitions, the most likely scenario for exposure is inhalation. Therefore, the human alveolar epithelial cell line, A549, and the human alveolar macrophage cell line, U937, were chosen as an *in vitro* model for inhalation. For *in vitro* studies, the A549 and U937 cells were first cultured separately, and cell viability was assessed after a 24, 48, and 72 hour exposures at concentrations ranging from 0-500 µg/mL. Since these cells are found together in the alveoli, the cells were then cultured together in a 3:1 (A549:U937) ratio, and NPs were dispersed in an artificial lung surfactant prior to exposure [8,9]. Cell viability after exposure was determined using a Live Cell/Dead Cell staining kit from Biovision.

To assess the ability of the immune cells in the lung to protect the epithelial cells, the co-cultures were exposed to aluminum NPs and then infected with bacteria. Changes in the phagocytic function of macrophages, as well as gene expression and cytokine secretion were assessed.

Crystal structure mediates mode of cell death in TiO₂ nanotoxicity

The goal of this study was to evaluate the role of size in TiO₂ nanotoxicity with NPs composed of the same crystal structure and to evaluate crystal structure in TiO₂ nanotoxicity with NPs of a similar diameter. We chose to use the HEL-30 mouse keratinocyte cell line as a model for dermal exposure since nano-TiO₂ is used in cosmetics and sunscreens. In the size dependent studies, all the NPs are 100 percent anatase and aggregate sizes were determined in order to take into account the effect of agglomeration on size dependent toxicity. In addition, varying crystal structures were assessed while the size of the particles was controlled. NP size and morphology were examined in dry form using TEM. DLS was used to assess the size of

NPs dispersed in water and cell media, and LDV was used to assess particle charge of NPs dispersed in water.

Cell viability after NP exposure was evaluated using the MTS assay, oxidative stress was assessed by measuring the formation of ROS, and membrane integrity was evaluated using the LDH assay.

The role of nanoparticle charge in gold nanotoxicity

This study was designed to determine the biocompatibility of gold NPs using the HaCaT cell-line as a model. We evaluated the cytotoxicity of Au NPs with different ligands (MEEE which makes the particles neutral, MES which makes the particles anionic, and TMAT which makes the particles cationic) with 0.8 nm, 1.5 nm and 10nm diameters. CytoViva and TEM microscopy were used to visualize the uptake of 10 $\mu\text{g/mL}$ of NPs into the keratinocytes. MTS, LDH, and ROS assays were performed to assess the toxicity of the NPs at different concentrations (0, 10, 25, 50, and 100 $\mu\text{g/mL}$), and real-time polymerase chain reaction (PCR) was used to determine if gene expression of DNA damage genes was up or down-regulated.

Shape matters: Differential cytotoxicity observed in gold nanospheres and nanorods

The majority of nanotoxicity studies have focused on size and very few have assessed the role that shape plays in determining NP toxicity. This study evaluated the cytotoxicity of gold NPs with different shapes. Gold nanorods 51 nm in length with varying diameters were compared to gold nanospheres 12 nm in size. Particle size and morphology was determined using TEM. For cellular uptake studies, cells were plated on chambered slides and exposed to 25 $\mu\text{g/mL}$ of each particle for 24 hours. After exposure, the cells were fixed with methanol and mounted using Permount. CytoViva imaging was used to determine whether the particles had been taken into the cell.

Toxicity was assessed in the HaCaT cell-line. The cells were treated with varying concentrations (0-100 $\mu\text{g/mL}$) of the gold nanomaterials for 24 hours, and biocompatibility was tested using cell viability, membrane integrity, and ROS as endpoints. For cytotoxicity assays, a 96 well plate was seeded with 50,000 HaCaT cells per well and allowed to grow overnight at 37°C. The next day, the cells were treated with 5, 10, 25, 50, and 100 $\mu\text{g/mL}$ concentrations of each of the gold particles. Cell proliferation and viability were assessed using both the MTS assay and CellTiter 96 Aqueous One Solution Cell Proliferation Kit from Promega.

Toxicity of amorphous silica nanoparticles in mouse keratinocytes

The objective of this study was to illustrate the acute effects of well dispersed and different sizes of silica NPs in mouse keratinocytes cells. The DLS method was used to characterize silica NP sizes. To verify the uptake of NPs, cells were incubated with 100 $\mu\text{g/mL}$ of silica NPs for 24 hours, followed by imaging with TEM. These particles were studied for determining cellular uptake, changes in mitochondria-based viability, membrane leakage, reduced glutathione (GSH), and oxidative stress.

GSH possessing significant density of a free reductive thiol group for the cell is an important antioxidant for cells. During the process to remove hydrogen peroxide or lipid peroxides, GSH (reduced form) becomes oxidized to GSSG which is then recycled to GSH by the enzymes in the cells. GSH was measured after 24 hour exposure of silica NPs, using a glutathione assay kit by Cayman Chemical Company (Ann Arbor, MI). GSH levels were compared with the control values.

Unique cellular interaction of silver nanoparticles: Size dependent generation of reactive oxygen species

Deposition of inhaled particulate matter has been found to be dependent on size; consequently silver NPs are likely to have an effect on the deep regions of the lung; in specific, the alveolar region [50]. In the present study, rat alveolar macrophages (MAC) were selected as a model cell-line to assess the degree of toxicity and explore possible bio-mechanisms of toxicity after possible inhalation.

Cell viability was assessed via the MTT assay. Additionally, several cellular mechanisms stemming from NP-induced toxicity were assessed, including oxidative stress, and inflammatory and immunological responses. Oxidative stress was measured using the ROS assay. The mitochondrial membrane potential (MMP) was evaluated after 24 hour of exposure to different concentrations of silver NPs. For this assay, cells were incubated with Mit-E-Ψ reagent then examined for fluorescent intensity relative to control cells (100 percent) with microplate reading. Fluorescent intensity data expressed as percent of control as means \pm SD of three independent experiments. For qualitative determination of MMP, NP exposed cells were incubated with Mit-E-Ψ reagent and Hoescht 33342 stain then imaged using the BD pathway 435 confocal microscope.

Silver nanoparticles disrupt GDNF signaling in spermatogonial stem cells independent of nanoparticle size and coating

Hydrocarbon-coated silver (Ag-HC) NPs of 15 nm, 25 nm, and 80 nm diameters were synthesized and generously received in powder form from Dr. Karl Martin of NovaCentrix, Austin, TX (formerly Nanotechnologies, Inc.). For these NPs, the surface HCs are not a continuous coating, but rather an artifact of the manufacturing process that uses HC to prevent sintering of the Ag NPs during plasma synthesis. Polysaccharide-coated silver (Ag-PS) NPs of 10 nm, 25-30 nm, and 80 nm diameters were received dispersed in solution from Dr. Dan Goia's Laboratory at Clarkson University, Potsdam, NY. For these NPs, there was a continuous coating around the NPs.

The C18-4 cell line was established by stably transfecting type A spermatogonia with the Large T antigen gene driven by the ecdysone promoter. The cells were grown in a 1:1 mixture of Dulbecco's Modified Eagle's Medium/Nutrient F-12 Ham (DMEM/Ham's F-12, Hyclone) supplemented with 10 percent fetal bovine serum (FBS), 2 mM glutamine and 1 percent penicillin/streptomycin (pen/strep). For cultures that required serum starved conditions, FBS was replaced with 10 percent synthetic Nu serum (BD Biosciences, San Jose, CA). Cells were plated in 6-well or 96-well tissue culture plates (Falcon, Fisher Scientific, Pittsburgh, PA) and incubated at 34 degrees C and 5 percent CO₂ in a humidified incubator. Once the cells were 80 percent confluent they were treated with a range of concentrations of different silver NPs.

The various silver particles were characterized using TEM to obtain NP size and morphology at an accelerating voltage of 100kV. NPs were examined after suspension in water (1 mg/mL) and subsequent deposition onto formvar/carbon-coated TEM grids (~10 μ L). Information on mean size and standard deviation was calculated from measuring over 300 NPs in random fields of view in addition to images that show general morphology of the NPs. Particle size in solution was determined using DLS. Samples were prepared as described for TEM and vortexed to provide a homogeneous solution. A 1.5 mL aliquot of solution prepared at a concentration of 50 μ g/mL was transferred to a square cuvette for DLS measurements.

X-ray photoelectron spectroscopy (XPS) was used to determine NP composition and surface coating composition. XPS characterization was performed on a Surface Science Labs SSX-100 system. This instrument has a monochromatic aluminum x-ray source with a nominal x-ray beam diameter of 600 μm . The Al K(alpha) x-ray energy used was 1486.6 eV. To generate these x-rays, an aluminum anode is bombarded by an electron gun operating at 10 kV with a 10 mA emission current (100 Watts). Sample preparation consisted of placing a drop of the Ag NP sample in water on a piece of clean Al foil, then allowing the water to evaporate at room temperature before measurements. The measurements were repeated in duplicate.

For immunoprecipitation and Western blotting, the cells were cultured in 100 mm Petri dishes until 50 percent confluency in DMEM/F-12, 2 mM glutamine and 1 percent pen/strep as described above. To provide a controlled environment, we replaced 10 percent FBS with 10 percent Nu synthetic serum (Fisher Scientific, Pittsburgh). The cells were exposed to 10 $\mu\text{g/mL}$ HC- and PS-coated NPs before a 4 hour stimulation with GDNF (100 ng/mL, recombinant rat GDNF, R&D Systems, Minneapolis, MN). As controls, we used cells that were not exposed to NPs, with or without 100 ng/mL GDNF for 4 hours. The cells were lysed with a lysis buffer (Cell Signaling, Danvers, MA) containing a 1:100 protease inhibitors cocktail and a 1:100 phosphatases inhibitor cocktail (100x solutions, both from Pierce, Rockford, IL). Protein concentrations were assessed with the Lowry method (DC Protein Assay, Bio-Rad, Hercules, CA). The samples (500 μg proteins) were immunoprecipitated with an anti-Fyn antibody using standard methods (Upstate Technologies/Millipore, Billerica, MA). Then 30 μg of the immunoprecipitates were loaded onto 10 percent Tris-HCl gels for electrophoresis (Bio-Rad, Hercules, CA). The proteins were transferred onto nitrocellulose membranes and probed using the primary antibodies anti-Fyn and antiphospho-Src family kinase (SFK) (Upstate Technologies/Millipore, Billerica, MA). After incubation with the appropriate biotin-conjugated secondary antibodies, the membranes were incubated with streptavidin-HRP, and HRP revealed with an enhanced DAB substrate (Pierce, Rockford, IL). For quantitative analysis, the membranes were scanned with a gel/membrane imaging system (Typhoon Blue Laser Module, Amersham Biosciences, Piscataway, NJ), and the band intensities evaluated with the KODAK 1D Image Analysis software (Kodak Molecular Imaging Systems Carestream, Rochester, NY). The background was evaluated as the median intensity of the total number of pixels within the perimeter outside the bands and subtracted from the measurement of the protein band intensity. The protein bands intensities were standardized over the intensity of phosphorylated Fyn in the control samples without NPs or GDNF. The data were generated from triplicates, and 2 different experiments. The data are represented as the mean + the standard deviation. A Student t test was run, and $p < 0.05$ indicated significance.

SEM was used to demonstrate binding of the Ag NPs to the cell surface at 5kV. Prior to imaging, the cells were fixed with 4 percent paraformaldehyde, dehydrated through analytical grade 30-100 percent ethanol, mounted to aluminum stubs with double-sided carbon adhesive tape, and sputter coated with gold. TEM was used to demonstrate uptake of Ag NPs in the cells at 75-80 degrees K. The C18-4 cells were seeded in a 100 mm tissue culture dishes and once 85 percent confluent they were treated with 10 $\mu\text{g/mL}$ of the different Ag NPs. Twenty-four hours later, the cells were fixed in 2 percent paraformaldehyde/2.5 percent glutaraldehyde for 2 hours. After fixing, the cells were stained with 1 percent osmium tetroxide for 1 hour and then the cells were scraped from the plate to be processed for TEM. The cells were dehydrated using increasing concentrations of ethanol with three changes of 100 percent ethanol. The samples were then placed in 100 percent resin and cured overnight at 60 degrees C in BEEM capsules.

The samples were then sectioned on a Leica ultramicrotome at a thickness of 50-100 nm and collected on a TEM grid.

To measure cell viability, the C18-4 cells were seeded in 96-well plates at a density of 30,000 cells/well. The following day, the cells were treated with 10 $\mu\text{g/mL}$ of Ag NPs or polysaccharide and 100 ng/mL of GDNF. Fresh GDNF was added daily for six days and cell proliferation was assessed each day using the MTS solution from Promega.

Kinase activity was determined using the tyrosine kinase activity kit (Chemicon International, Inc., Temecula, CA), and 15 ng of purified active Fyn purchased from Chemicon/Millipore (Billerica, MA). The active Fyn was incubated with 10 $\mu\text{g/mL}$ of Ag NPs or polysaccharide, and 10 μM of the Src family inhibitor SU6656 was used as a control. Each experiment was performed in triplicate and the data are represented as the mean \pm the standard deviation. A Student t test was run and $p < 0.05$ indicated significance.

For *in vivo* Fyn and Akt kinase assays, the C18-4 cell line was grown in complete cell culture media and 10 percent FBS until the cells were 75 percent confluent. The cells were then treated with 10 $\mu\text{g/mL}$ of Ag NPs, polysaccharide, or 10 μM of SU6656 for 24 hours and then serum starved overnight. The following morning the cells were stimulated with 100 ng/mL of GDNF for four hours and proteins were isolated in a non-denaturing lysis buffer using osmotic lysis.

The Fyn kinase was immunoprecipitated using a Fyn antibody (Santa Cruz Biotechnology, Santa Cruz, CA) and Fyn activity was assessed using a tyrosine kinase activity kit (Chemicon International, Inc., Temecula, CA). Each experiment was performed in triplicate and the data are represented as the mean \pm the standard deviation. A Student t test was run and $p < 0.05$ indicated significance.

The Akt kinase was immunoprecipitated using an Akt antibody from BioVision and then the KinaseSTARTM Akt Activity Assay Kit was used to determine Akt activity. The immunoprecipitated Akt kinase was incubated with a GSK-3 α /ATP mixture to facilitate the kinase reaction, and then the level of phosphorylated GSK-3 α protein was detected using a rabbit anti-Phospho-GSK-3 α (Ser 21) specific antibody at 1:1000 dilution and a Cy3 labeled goat anti-rabbit secondary antibody. The Cy3 levels were detected using a Gemini Spectra Max plate reader with an excitation wavelength of 544 nm and an emission wavelength of 590 nm. Each experiment was performed in triplicate and the data are represented as the mean \pm the standard deviation based on a percent control. A Student t test was run and $p < 0.05$ indicated significance.

For *n-myc* expression analysis, the C18-4 cells were seeded in 6-well plates and once they were 80 percent confluent they were treated with 10 $\mu\text{g/mL}$ of Ag NPs or polysaccharide for 24 hours. After the 24 hour treatment, the cells were treated with 100 ng/mL of GDNF overnight. The following day, RNA was isolated from the cells using the Qiagen RNeasy Mini kit. Using 1 μg of RNA, *N-myc* and β -*actin* expression were then assessed using the SuperScriptTM One-Step RT-PCR with Platinum[®] Taq kit from Invitrogen. The primers used to detect mouse *N-myc* were 5'-ACTTCTACT TCG GCG G-3', $T_m = 47$ degrees C (forward), and 5'-TCT CCG TAG CCCAAT-3', $T_m = 44$ degrees C (reverse complement). The primers used to detect β -*actin* were 5'-GGA CTC CTATGT GGG TGA CGA-3', $T_m = 59$ degrees C (forward) and 5'-GCC TCG GTG AGC AGC-3', $T_m = 52$ degrees C (reverse complement). The primers were designed and evaluated using the NetPrimer program and ordered from Integrated DNA Technologies (IDT, Coralville, IA). The PCR products were visualized on a 0.8 percent agarose gel stained with ethidium bromide using the Sygene Gel Documentation system and the band intensities were measured using the software analysis package for the system. The *N-myc*

expression levels were normalized based on the β -actin expression levels. Each experiment was performed in triplicate and the data are represented as the mean \pm the standard deviation based on a percent control. A Student t test was run and $p < 0.05$ indicated significance.

For statistical analysis, the data were first read with a critical screening to eliminate biologically inconsistent data, then the test of Dixon was used to confirm the elimination (critical level 5 percent). The data were analyzed with the statistical analysis software GraphPad Prism (Microsoft). For each NP growth inhibition curve, the normality of the data dispersion was not assumed and the non-parametric test of Kruskal and Wallis was used. For the NPs where the non-parametric test shows a significant difference, a one-way analysis of variance (ANOVA) and post hoc test of Dunnett against the control were done (the normality and homogeneity of the variances hypothesis were assumed). Then, a Student unpaired t test (one tailed) was applied between the last non-significant toxic dose and the first toxic dose. Wherever this difference was significant, the t-test was repeated with the next toxic dose (the non parametric test was done to confirm the validity of results). In order to compare the different type of NPs, the post-hoc tests of Bonferini were added to the ANOVA. The critical level of significance was chosen at 5 percent for each test.

Characterization and biocompatibility of “green” synthesized silver nanoparticles

Silver NPs were prepared using a “green” method involving the use of tea extract. For the tea extract preparation, 1 gram of tea powder (Red label from Tata, India Ltd. 99 percent) was boiled in 50 mL of water and filtered through a 25 μ L Teflon filter. Then 2 mL of 0.1 N AgNO_3 (AgNO_3 , Aldrich, 99 percent) was mixed with 10 mL of tea extract and shaken to ensure thorough mixing. The reaction mixture was allowed to settle at room temperature. The color of the reaction mixture changed from light brown to green color indicating the formation of Ag NPs. The formed Ag NPs are stable in nature. A similar procedure was repeated with 5, 3, 1, and 0.5 mL of tea extract. We extended this strategy using pure tea component, 0.01 N (-) epicatechin (Aldrich, 99 percent), and the procedure was repeated exactly as described earlier for tea extract with 0.1 N AgNO_3 .

The primary particle size of all NPs used in this study was determined using TEM. Ten μ L of each sample was spotted on a carbon-coated copper grid, which was purchased from Electron Microscopy Supply (product number 080612), and then viewed at 100 KV. The diameter of one hundred particles were measured using the Advanced Microscopy Techniques imaging software point to point measurement function, which calculates the average and standard deviation in the measurements.

The agglomerate diameter measurements were performed by DLS using the method previously described by Murdock et al. [63]. Samples were dispersed in water, HaCaT Exposure Media (HEM), and Macrophage Exposure Media (MEM) at a concentration of 50 μ g/mL.

The rat alveolar macrophage cell-line (MAC) was purchased from ATCC (#CRL – 2192) and cultured with F-12K media (Kaighn’s modification of Ham’s F-12) with 20 percent FBS and 1 percent pen/strep. The MAC line was incubated at 37 degrees C, 100 percent humidity, and 5 percent CO_2 . During exposure, the MAC line was cultured with F-12K media with 10 percent FBS and 1 percent pen/strep (MEM).

The human keratinocyte cell-line, HaCaT, was received from Dr. James Duiman at USAURICD (Boukamp et al 1988). The HaCaT cells were cultured with RPMI-1640 media with 10 percent FBS and 1 percent pen/strep and incubated at 37 degrees C, 100 percent humidity, and 5 percent CO_2 . During exposure, the HaCaT line was cultured with RPMI-1640

media with 1 percent pen/strep and no FBS serum (HEM). Cells were seeded to provide 60-80 percent confluency in 96 well plates or chamber slides within a growth period of 48-72 hours. Upon reaching 80 percent confluency, typically 48 hours, cells were treated with either 50 $\mu\text{g/mL}$ or 100 $\mu\text{g/mL}$ concentrations of NPs suspended in the respective cells exposure media. After a 24 hour exposure, the NP biocompatibility was assessed using cytotoxicity assays and cellular uptake evaluation.

The MAC and HaCaT cells were exposed to the Ag NPs at 50 and 100 $\mu\text{g/mL}$ in their respective exposure media. After a 24 hour incubation with the NPs, cell proliferation was measured using the CellTiter 96[®] Aqueous One Solution Cell Proliferation Assay (Promega), and membrane leakage was evaluated using the CytoTox 96[®] Non-Radioactive Cytotoxicity Assay (Promega). The amount of mitochondrial function and membrane leakage was then assessed spectrophotometrically with a SpectraMAX Plus 190 microplate reader. The data are represented as an average of three independent trials \pm the standard deviation.

MAC and HaCaT cells were exposed for 24 hours to a 15 $\mu\text{g/mL}$ concentration of silver NPs. This low concentration was used to increase imaging quality by decreasing the number of Ag NPs refracting light and allowing a clear image of the cell for determining cellular uptake. After exposure, cells were washed with PBS to remove any excess Ag NPs that were not interacting with the cells. Slides were observed with the CytoVivaTM150 System using the method previously described by Skebo et al. [144].

The data are represented as an average of three independent trials \pm the standard deviation. The cytotoxicity assays were run and any group with a p value less than 0.05 was considered significant.

In-vitro biocompatibility of silver nanoparticles anchored on multi-walled carbon nanotubes

Characterization of the MWCNT-Ag composites was carried out using SEM, XRD, and TEM. SEM was carried out using a Philips FEI XL30 FEG SEM operated at 15 kV. XRD was performed using a XRD D8 ADVANCE – BRUKER AXS, with a Cu K_{α} radiation ($\lambda = 1.54060$ Å) and operating current and voltage maintained at 35 kV and 25 mA. High resolution TEM images were acquired using a HRTEM -field emission JEOL-JEM-3000F.

HaCaT cells were maintained in RPMI-1640 with 1 percent pen/strep and 10 percent FBS at 37 degrees C and 5 percent CO_2 . The cells were passaged using trypsin-EDTA and PBS when they reached 70-80 percent confluency.

For cell viability, the MTS assay was employed. HaCaT cells were plated at cell densities of 50,000 cells / 200 μL in 96 well plates. After 24 hours of cell growth the cells were dosed with carbon nanotubes. Carbon nanotubes functionalized with silver (MWCNT-Ag), Carbon nanotubes functionalized with silver and doped with nitrogen (CNx-Ag), and carbon nanotubes functionalized with silver and carbonyl groups (COx-Ag) were used. Each nanotube composite was plated in triplicate at concentrations of 5, 10, 25, 50 and 100 $\mu\text{g/mL}$ in RPMI-1640 exposure media for each of three trials. The plates were then allowed to sit for 24 hours and the media was replaced with RPMI-1640 exposure media after washing 3 times with PBS. The plates were then read on the BioTek Synergy Plate reader at 490 nm at time points of 24, 48, 72 and 168 hours.

For cell imaging, HaCaT cells were plated in 2 chambered slides at cell densities of 300,000 cells/mL and incubated for 24 hours. After 24 hours the cells were dosed with 25 $\mu\text{g/mL}$ concentrations of MWCNT-Ag, CNx-Ag and COx-Ag in exposure media for 24 hours. The HaCaTs were then rinsed once with PBS and stained using the AlexaFluor 555 Dye. The

cells were fixed in 2 percent paraformaldehyde. They were then stained with 25 μ L of stain per mL of media and incubated at 37 degrees C. One to two drops of antifade with DAPI were added to each chambered and the cells were imaged using CytoViva.

ROS production in the HaCaT cells was measured using the Image-IT Live Green ROS Detection Kit (I36007 Molecular Probes). The HaCaT cells were grown in 96 well plates at densities of 100,000 cells / 200 μ L. Induction of ROS was performed using tert-butylhydroperoxide according to the directions and allowed to incubate for 60 minutes. The carboxy-H₂DCFDA and Hoechst 33342 stains were also used according to the instructions from the kit. The Hank's balanced salt solution with calcium and magnesium (HBSS/Ca/Mg) was used for the induction of ROS and the staining.

Biocompatibility of carbon foam substrates for osteoblast growth

Two types of microcellular carbon foam were researched versus flat graphite to study the effect of surface topography on osteoblast growth. Carbon foam was purchased from Koppers Inc. and differed in pore size. For surface modification studies, carbon foam was coated with silicon dioxide, and collagen. The silicon dioxide coating on the carbon foam was done through a plasma coating process. The collagen coating on the foam was conducted through a process of making a collagen/PBS solution and soaking the carbon foam for 2 hours and letting it air dry to let the collagen form on the foam. Before any experiments were conducted, each foam sample was rinsed with PBS and sterilized under ultraviolet light for at least 20 minutes.

A cell density of 1×10^6 cells/mL of human fetal osteoblasts (hFOB) were seeded on uncoated, silicon dioxide, and collagen coated samples. They were incubated for 72 hours before the preparation for microscopy. After the carbon foam is coated and cells are seeded on them, they were viewed in an SEM. This was done by growing the cells on the foam, and then fixing them in a paraformaldehyde solution. Next the samples were dried with increasing amounts of ethanol to prepare the substrates. The samples were then brought to Wright State University and placed in the SEM where the morphology was then viewed for each sample.

In order to view cell morphology, cell staining was performed for each of the surface coating samples. The osteoblasts were stained with actin stain, Alexa Fluor 555 phalloidin, and nuclear stain, Prolong Gold Reagent with DAPI.

Mitochondrial function of human fetal osteoblasts was assessed as a measure of cell viability. Once the cells had grown for 72 hours, cell viability was assessed by evaluating mitochondrial function using the CellTiter 96[®] AQueous One Solution assay of Promega. The solution reagent contains the tetrazolium compound MTS and an electron coupling reagent (phenazine ethosulfate; PES). The quantity of formazan product as measured by the amount of 490 nm absorbance is directly proportional to the number of living cells in culture.

RESULTS AND DISCUSSION

Results by Study

Immune suppression in MRSA-infected human alveolar co-cultures treated with Al, Al₂O₃, and Al-OA nanoparticles

The three types of NPs used in this study (Al, Al₂O₃, and Al-OA) were characterized in their dry powdered form using TEM analysis to assess the primary NP size and the morphology. All three types of aluminum were spherical in morphology and had similar size distributions (Fig. 1). In addition, the average NP size in solution was determined once the NPs had been dispersed in an artificial lung surfactant. The two NovaCentrix NPs (Al and Al₂O₃) exhibited a similar size in solution ~800 nm, while the Al-OA NPs were three times larger with the average agglomerate size ~2400 nm.

A Sample	Average Nanoparticle Size after Dispersion in Lung Surfactant	
	TEM(nm)	DLS Z-Ave (d.nm) ± Pdl
Al ₂ O ₃ 40nm	48.08 ± 21.01	878 ± 0.495
Al 50nm	32.71 ± 28.28	805 ± 0.497
Al-OA 50nm	51.09 ± 22.48	2430 ± 1.00

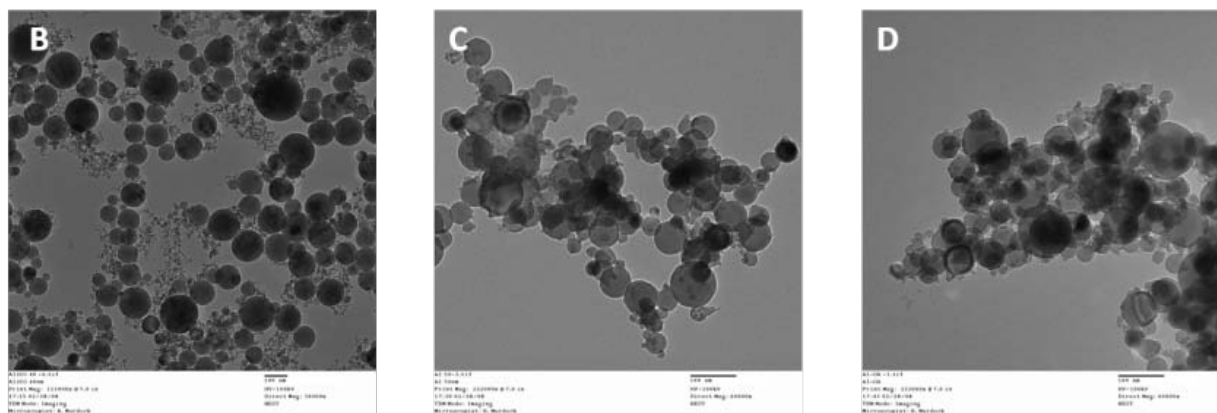


Figure 1. Aluminum nanoparticle characterization. **A.** Aluminum NP size distributions prior to and after dispersion in an artificial lung surfactant. The TEM analysis measurements determined that the three types of aluminum NPs had relatively similar sizes. After the NPs had been dispersed in an artificial lung surfactant, DLS was performed to determine the average NP size in solution. The Al₂O₃ and Al NPs had relatively similar average sizes, while the Al-OA NPs had an average size that was approximately three times greater than the other aluminum NPs once dispersed in the lung surfactant; **B.** TEM micrograph of the NovaCentrix aluminum oxide NPs; **C.** TEM micrograph of the NovaCentrix aluminum NPs; **D.** TEM micrograph of the aluminum oleic acid NPs synthesized by Dr. Chris Bunker's group (AFRL/RZPF).

For *in vitro* studies, the A549 and U937 cells were first cultured separately and cell viability was assessed after a 24, 48, and 72 hour exposure at concentrations ranging from 0-500 $\mu\text{g/mL}$ (Fig. 2 reports the data at 24 hours). The epithelial cells were more sensitive to the aluminum NPs than the macrophages and had a more dramatic loss of viability.

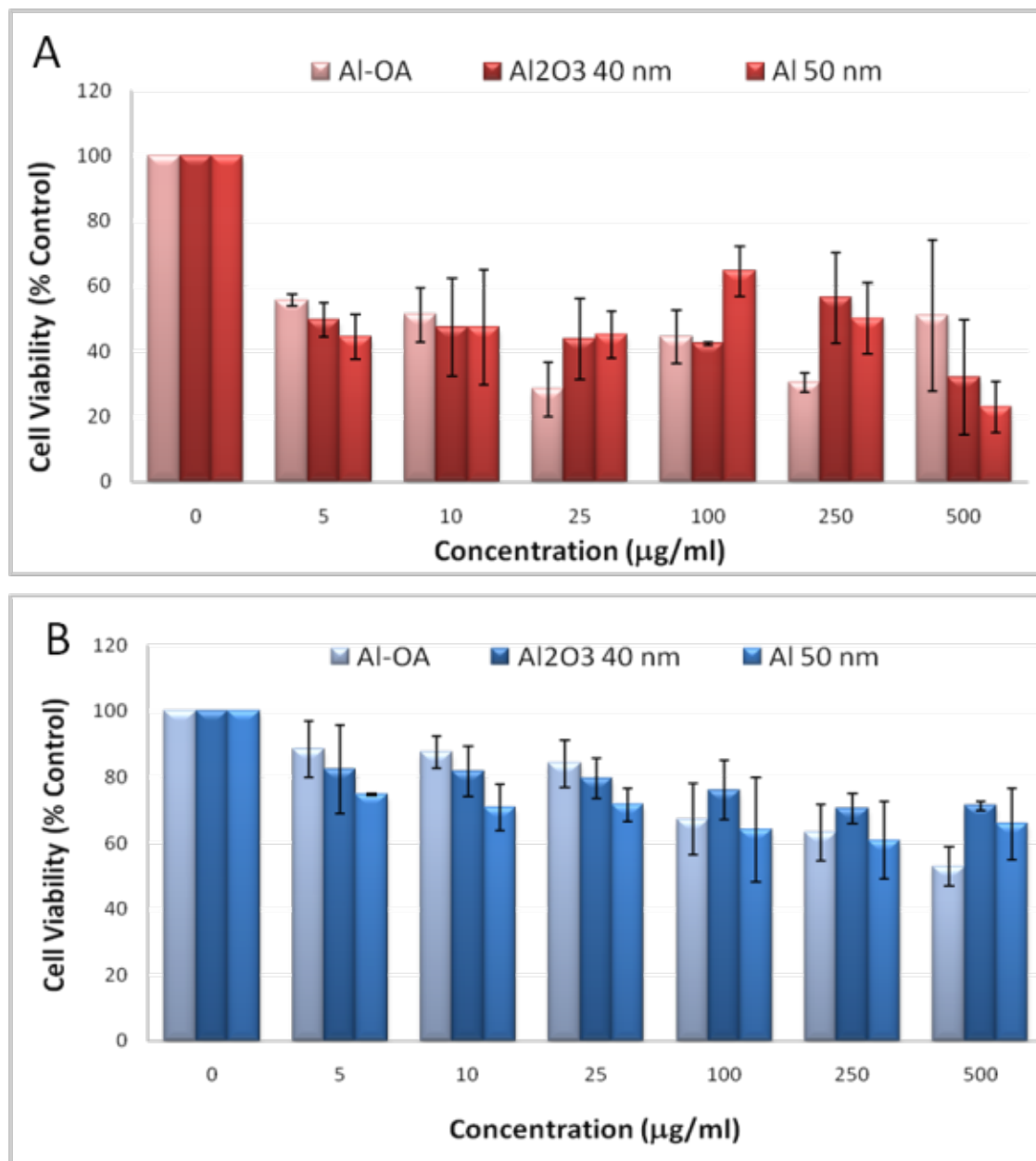


Figure 2. Cell viability in the alveolar cells when cultured separately. A. Alveolar epithelial cell viability. The A549 cells were cultured with varying concentrations of aluminum NPs and all three types of NPs reduced cell viability. Furthermore, this was not a concentration dependent effect; **B.** Alveolar macrophage cell viability. The U937 cells showed a slight reduction in cell viability when cultured with the various aluminum NPs, and this was independent of concentration. Overall the epithelial cells were more sensitive to the aluminum NPs than the macrophages and there did not appear to be a dose-dependent or surface chemistry-dependent effect on cell viability.

Since the function of the immune cells is to interact with and destroy foreign material we expected them to be less sensitive. In addition, since these cells are found together in the alveoli, the cells were cultured together to see if the presence of the immune cells protected the epithelial cells (Fig. 3), and in fact the epithelial cells which were originally very sensitive to a low (25 $\mu\text{g/mL}$) dose of aluminum NPs, were not affected at this dose when cultured with the macrophages. Furthermore, the aluminum NPs were mainly localizing in the macrophages.

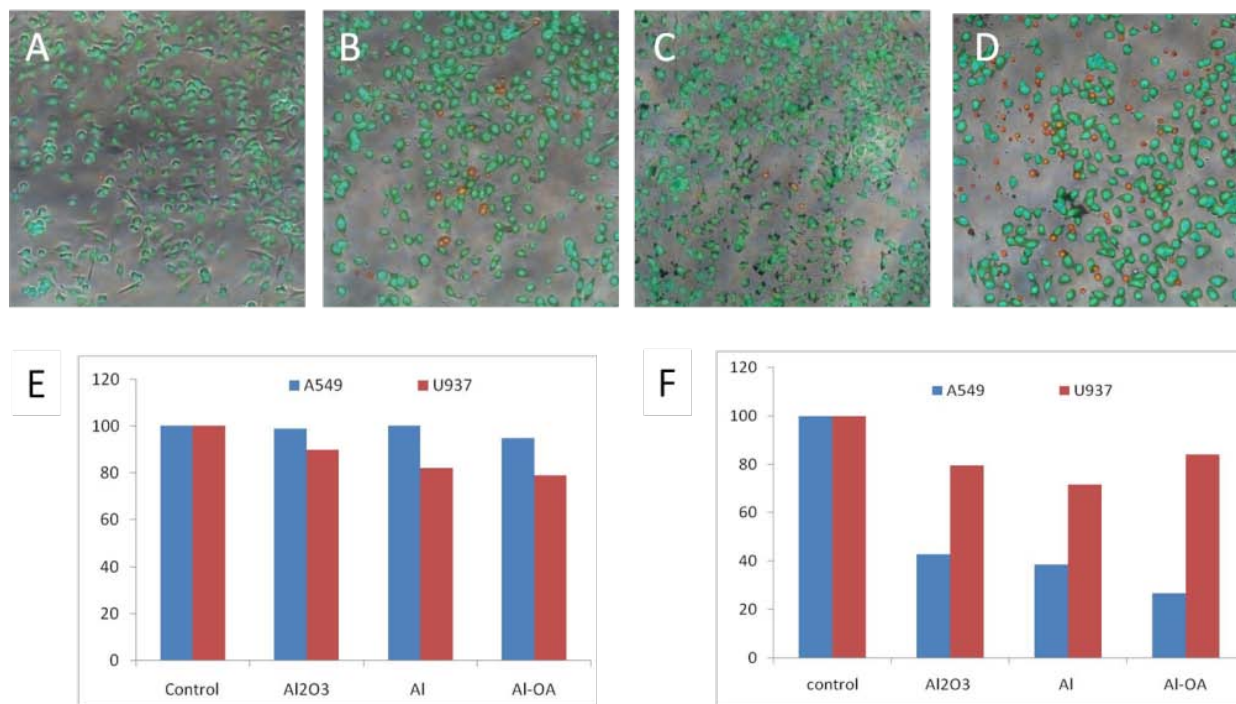


Figure 3. Cell viability in the lung co-cultures following exposure to the aluminum nanoparticles. A-D. are co-cultures treated with 25 $\mu\text{g/mL}$ of aluminum NPs for 24 h assessed using the Live Cell/Dead Cell staining kit from Biovision. The live cells are stained green by a cell permeable dye and the dead cells are stained red by a cell impermeable dye, propidium iodide. **A.** Control; **B.** Al_2O_3 ; **C.** Al; **D.** Al-OA; **E.** Cell viability based on the two cell types in the co-cultures. The A549 epithelial cells show no changes in viability while the U937 macrophages show a slight reduction in viability; **F.** The cell viability of each cell type when cultured individually with the same concentration of aluminum NPs. The A549 epithelial cells are very sensitive to the aluminum NPs while the macrophages show a slight reduction in viability. This data illustrated that the macrophages protect the epithelial cells in the co-cultures.

Additionally, since the main function of the macrophages is to destroy foreign material, we assessed if after treatment with the aluminum NPs the macrophages could still phagocytose bacteria. We found that the Al_2O_3 NPs did not impair phagocytosis, but phagocytosis was impaired by the Al and Al-OA NPs (Fig. 4). This data confirms previous studies where Al but not Al_2O_3 NPs reduced phagocytic function in rat alveolar macrophages [145].

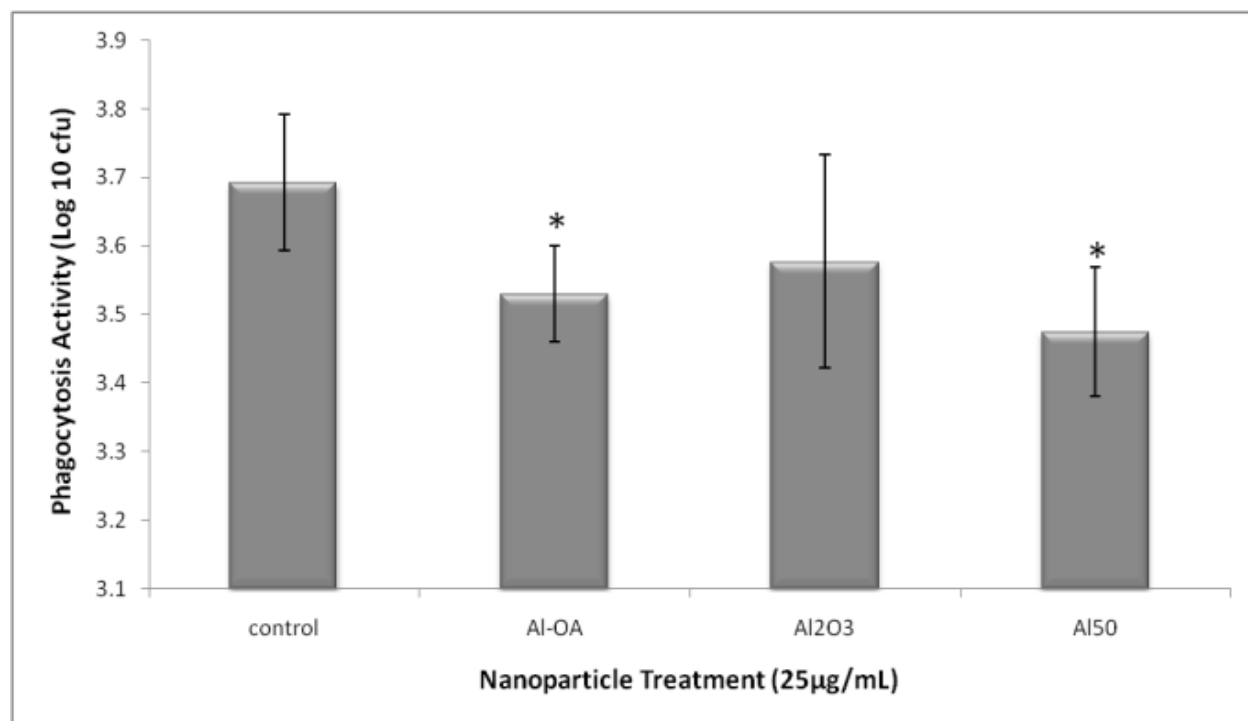


Figure 4. Phagocytic activity of human macrophages following exposure to aluminum nanoparticles and the bacteria MRSA. The Al₂O₃ NPs did not demonstrate a decrease in the cells ability to phagocytose bacteria. However, the cells treated with Al and Al-OA NPs demonstrated a significant decrease in phagocytosis activity.

Within the lungs, the macrophages are responsible for responding to and destroying foreign material. Since our phagocytosis data demonstrated that there was a change in the cells ability to phagocytose bacteria, we wanted to evaluate if the presence of aluminum further impaired this normal cellular response. The MRSA bacteria activate the NFκB pathway which is responsible for regulating genes involved in stress and inflammation. Therefore, following treatment with aluminum NPs and infection with MRSA, changes in gene expression were evaluated on genes involved in the NFκB pathway as well as targets of the NFκB pathway, which are inflammatory response and apoptotic genes. Figure 5A illustrates that there was minor induction of the NFκB pathway by the NPs alone. Furthermore, the MRSA stimulated a strong activation of the NFκB pathway as anticipated and the Al-OA NPs with MRSA generated activation of this pathway (Fig. 5B). However, the genes that were activated differed between the two groups. When the Al and Al₂O₃ NPs were present the cells were unable to generate activation of the NFκB pathway in the presence of MRSA. This data illustrated that the aluminum NPs alter or abolish the cells ability to respond to a pathogen via the NFκB pathway.

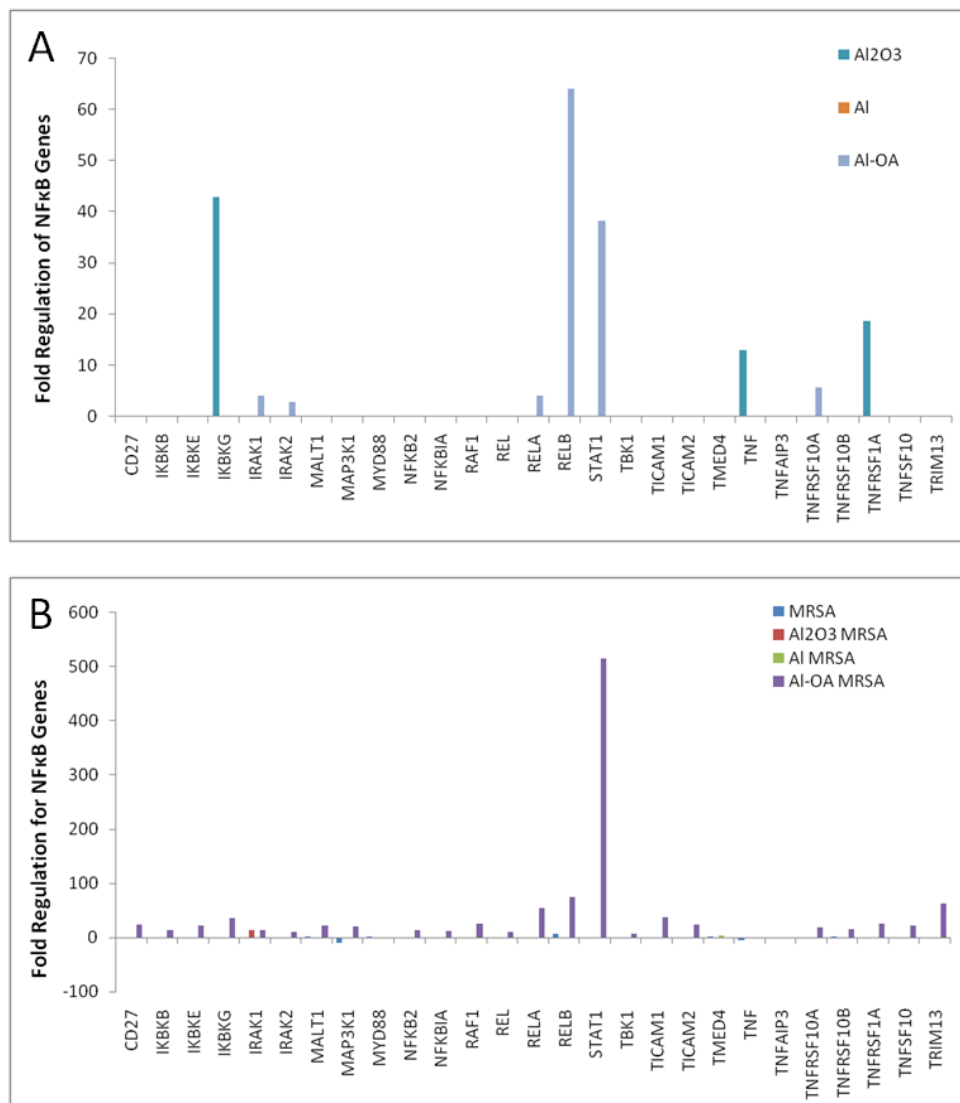


Figure 5. NFκB gene expression after treatment with aluminum nanoparticles and exposure to MRSA. **A.** Changes in NFκB activation following exposure to aluminum NPs. The Al₂O₃ and Al-OA NPs showed a mild increase in the activation of NFκB genes following a 24 h treatment; **B.** Changes in NFκB activation following exposure to aluminum NPs and MRSA. The MRSA stimulated a strong activation of the NFκB pathway as anticipated and the Al-OA NPs + MRSA also generated activation of this pathway. However, the genes that were activated differed between the two groups. When the Al and Al₂O₃ NPs were present the cells were unable to generate activation of the NFκB pathway in the presence of MRSA. This data illustrated that the aluminum NPs alter the manner in which cells are capable of responding to a pathogen via the NFκB pathway. (Represents three independent trials and only gene changes with a p<0.05 were reported).

One of the main targets of the NFκB pathway is inflammatory response genes and cytokines are key mediators of this response. In the NP alone treatments, the Al₂O₃ and Al-OA generated inflammatory responses while the Al NPs did not generate an inflammatory response (Fig. 6A). The MRSA induced inflammatory responses and when the Al and Al₂O₃ NPs were

present this induction was not seen. In contrast, the Al-OA MRSA treatments had the highest levels of inflammatory induction, which could be potentially harmful since the hallmark of toxic shock syndrome is high levels of cytokine production otherwise known as “cytokine storms.”

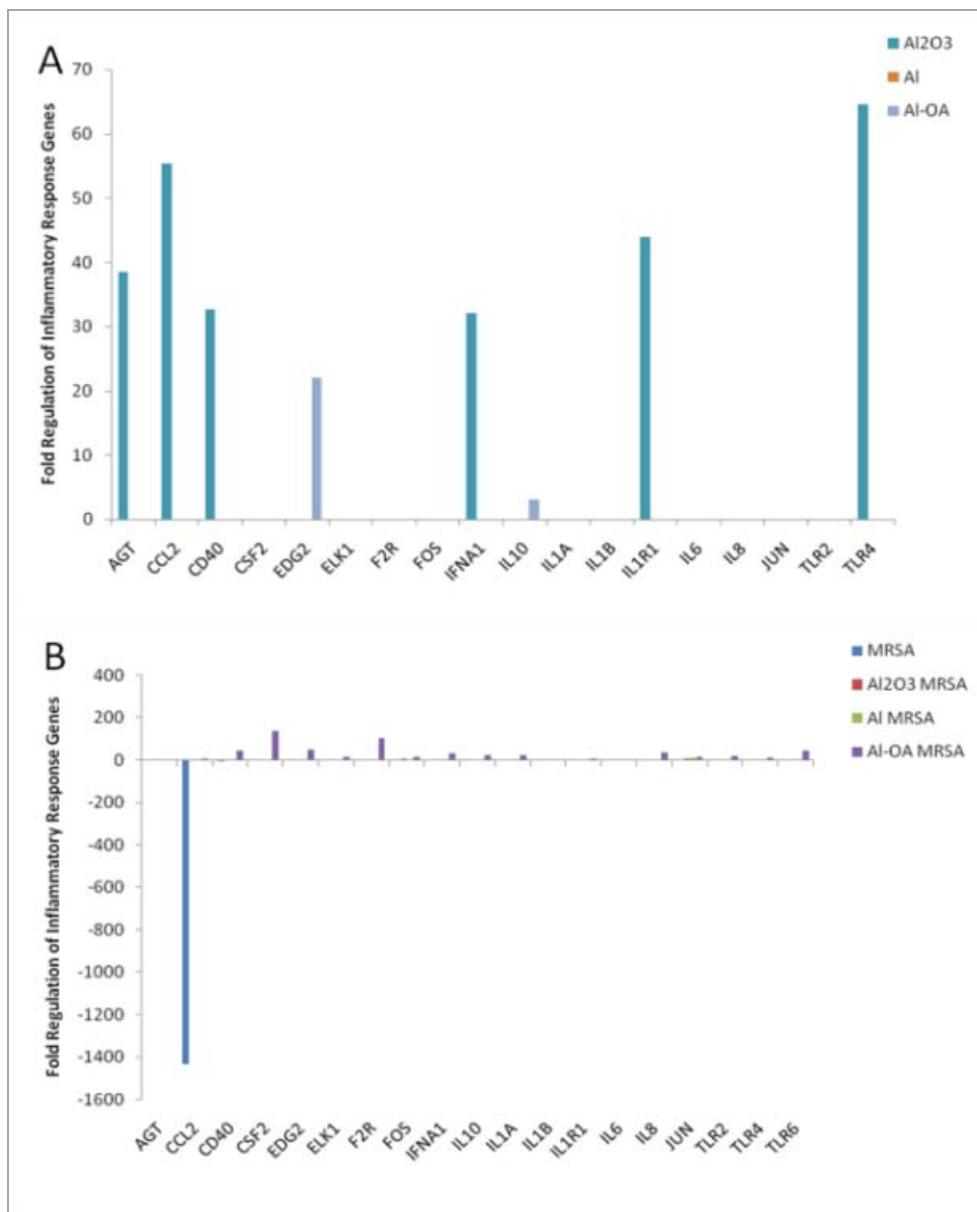


Figure 6. Activation of inflammatory response genes following exposure to aluminum nanoparticles and MRSA. **A.** Activation of inflammatory response genes by aluminum NPs. The Al₂O₃ generated a significant inflammatory response and the Al-OA NPs generated a minor response. The Al NPs did not generate any type of inflammatory response; **B.** Activation of inflammatory response genes following treatment with aluminum NPs and exposure to MRSA. The MRSA alone generates an inflammatory response and this response is greater in the Al-OA MRSA treatments. The Al₂O₃ and Al were unable to generate a significant response to the MRSA. (Represents three independent trials and only gene changes with a $p < 0.05$ were reported).

Another target of the NF κ B pathway is activation of apoptosis or programmed cell death. In the treatments with the NPs alone, there was a minor induction of apoptosis by the Al₂O₃ and Al-OA NPs, and the Al NPs did not induce apoptosis at all (Fig. 7A). In the MRSA treated co-cultures, the control cultures showed a significant down-regulation of the NOD1 gene which is responsible for activating apoptosis. In comparison, the Al-OA plus bacteria demonstrated an up-regulation of a wide range of apoptotic genes indicating that the presence of the Al-OA negatively impacted the cells' response to the MRSA (Fig. 7B). The Al₂O₃ and Al NPs did not generate a significant response.

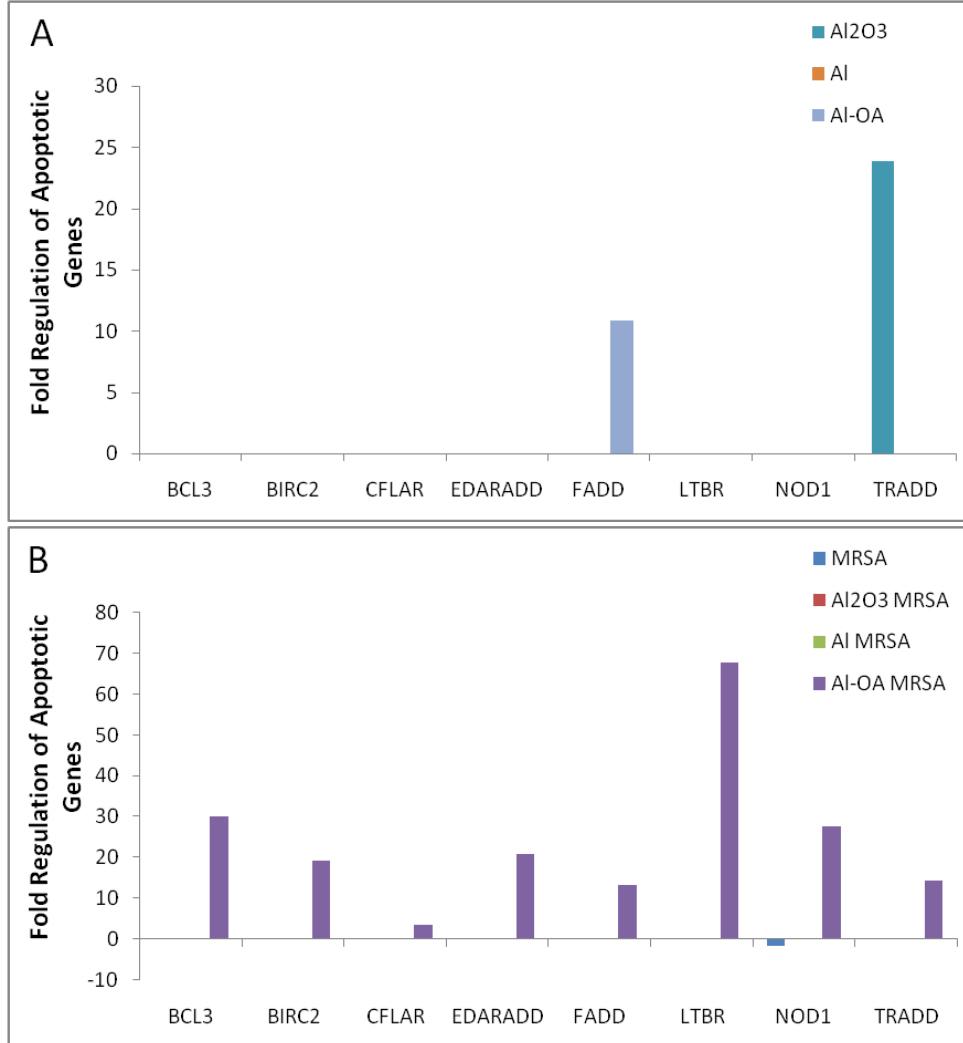


Figure 7. Activation of apoptotic genes after exposure to aluminum nanoparticles and MRSA. **A.** Activation of apoptotic genes after exposure to aluminum NPs. The Al₂O₃ and Al-OA NPs demonstrated minor activation of the cell death pathway. The Al did not initiate apoptosis at all; **B.** Activation of apoptotic genes after exposure to aluminum NPs and MRSA. The MRSA alone causes a slight down-regulation of NOD1. In comparison the Al-OA + MRSA treatment initiated up-regulation of a wide range of apoptotic genes, indicating the combination of the NPs and MRSA was harmful to the cells. The Al₂O₃ and Al did not generate a significant response apoptotic response to MRSA. (Represents three independent trials and only gene changes with a $p < 0.05$ were reported).

The lung co-cultures were treated with a low dose of aluminum NPs and then infected with the respiratory pathogen MRSA to determine 1) if the NPs initiated an inflammatory response and 2) if the presence of the aluminum NPs altered the normal inflammatory response. MRSA typically activates the proinflammatory cytokines IL-6, IL-1 β , and TNF α , which are responsible for altering the flow of blood to the infected site so that immune cells can be recruited to destroy the pathogen. When the aluminum NPs were present, the cells were unable to generate the typical response to MRSA, which makes the cells less able to fight infection (Fig. 8). Furthermore, the anti-inflammatory cytokine IL-8 is responsible for recruiting white blood cells to the site of infection to aid in killing pathogens. When MRSA is present secretion of IL-8 is up-regulated. However, when the aluminum NPs are present IL-8 is not up-regulated leaving the cells more vulnerable to the pathogen (Fig. 9). In addition, the aluminum NPs were shown to increase the down-regulation of IL-10 in the presence of MRSA (Fig. 10). This cytokine is responsible for inhibiting the synthesis of pro-inflammatory cytokines and blocks NF κ B activation, which initiates apoptosis. Therefore, the cells treated with aluminum NPs are unable to prevent apoptosis.

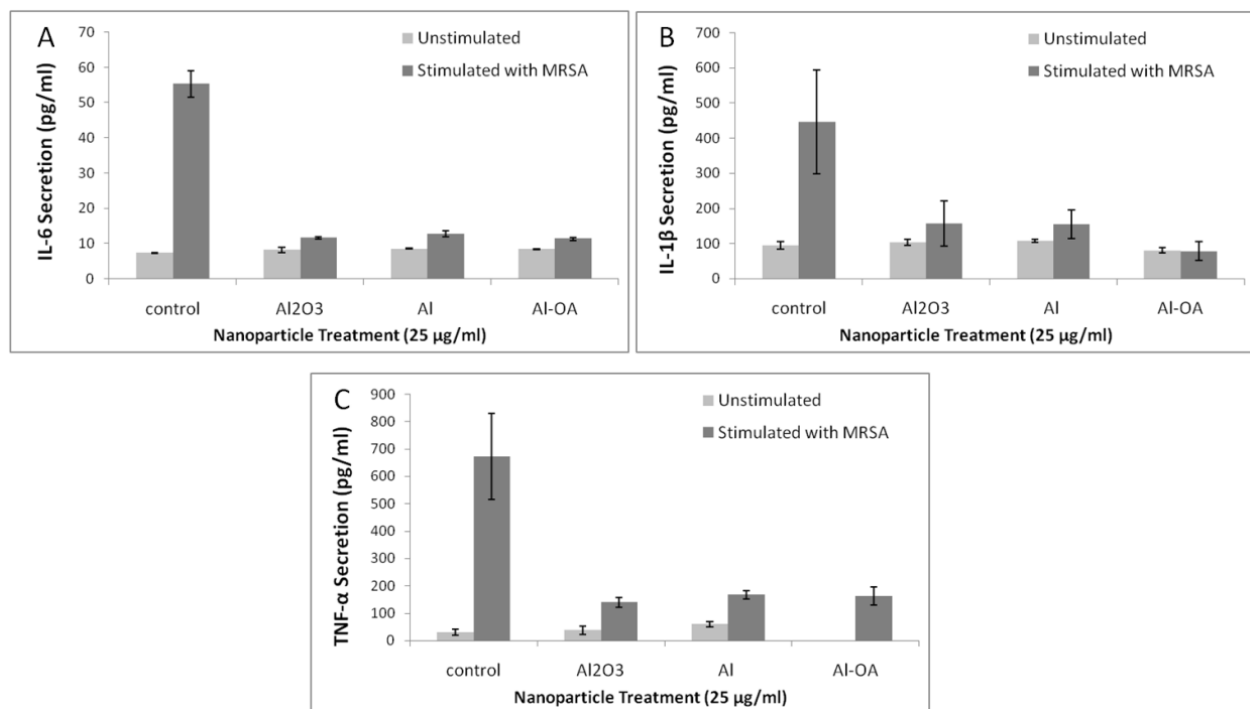


Figure 8. Secretion of pro-inflammatory cytokines from the lung co-cultures exposed to MRSA in the presence of aluminum nanoparticles. **A.** IL-6 Secretion. The bacteria MRSA initiated a 7.5 fold increase in the secretion of IL-6 in the lung co-cultures when compared to control cells; **B.** IL-1 β Secretion. MRSA stimulated a 5 fold increase in the secretion of IL-1 β when compared to the control cells in the lung co-cultures; **C.** TNF- α Secretion. The lung co-cultures treated with MRSA demonstrated a 22 fold increase in TNF- α secretion when compared to the control cultures. For all three cytokines, the increase in secretion that was observed after exposure to MRSA was not seen when the aluminum NPs were present. Furthermore, the reduced secretion of cytokines occurred independent of NP surface composition.

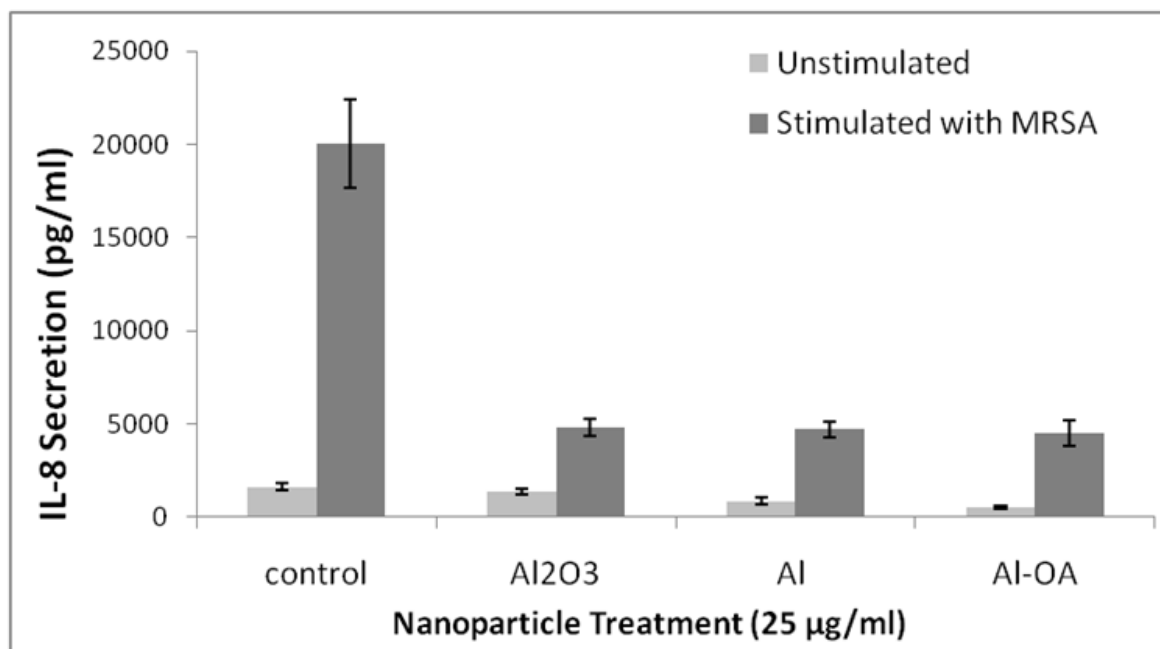


Figure 9. Secretion of anti-inflammatory cytokine IL-8 from the lung co-cultures exposed to MRSA in the presence of aluminum nanoparticles. IL-8 is an anti-inflammatory cytokine and following exposure to MRSA, IL-8 secretion was up-regulated 12 fold. However, this increase was not demonstrated in the lung co-cultures that contained aluminum NPs, and this inhibition was not dependent on NP surface coating.

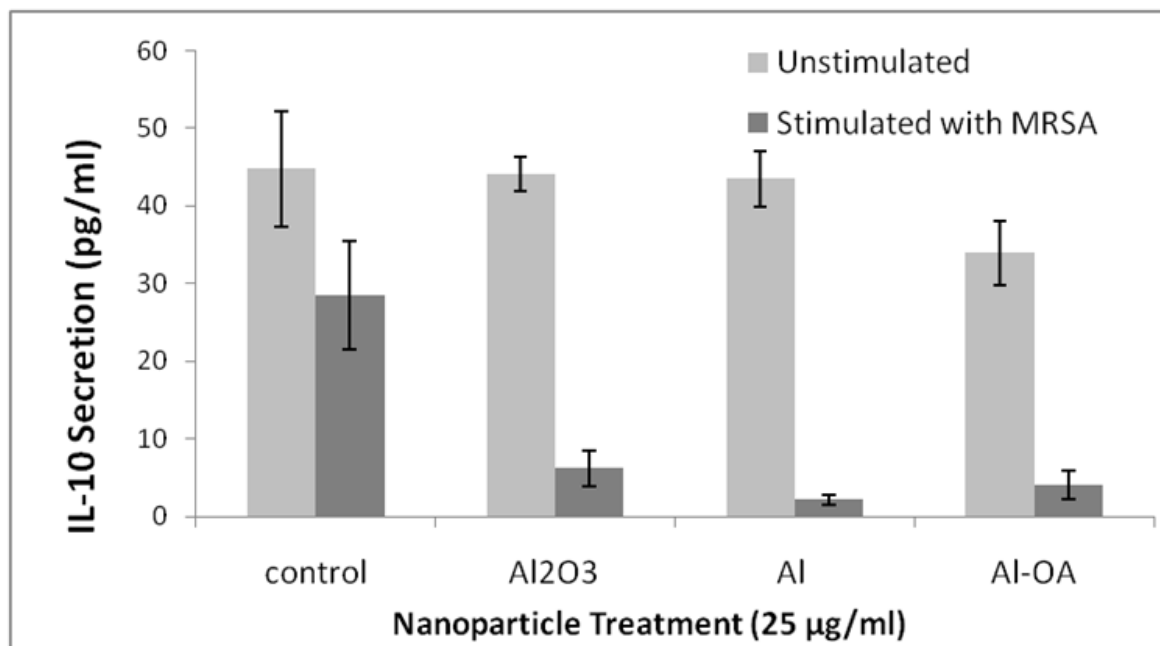


Figure 10. Secretion of chemokine IL-10 from the lung co-cultures exposed to MRSA in the presence of aluminum nanoparticles. IL-10 is a chemokine and the secretion was down-regulated 1.5 fold after exposure to MRSA. This decrease was even greater in the presence of aluminum NPs with a 7 fold decrease seen by the Al₂O₃, a 20 fold decrease by the Al, and an 11 fold decrease by the Al-OA NPs.

This research was published and highlighted in Toxicological Sciences in February 2008.

Crystal structure mediates mode of cell death in TiO₂ nanotoxicity

Table 3 provides a summary of the TiO₂ NPs with the average primary particle diameter, crystalline structure, and source, and Figure 11 provides TEM images of the different NPs.

Table 3. Titanium Dioxide Nanoparticle Diameter, Composition, and Source. **Previously reported by Liu et al. [62]

Particle Diameter	Particle Composition	Source
6.3 nm \pm 1	100% Anatase	Dr. Pratim Biswas, Washington University in St. Louis
10 nm \pm 2	100% Anatase	Dr. Pratim Biswas, Washington University in St. Louis
50 nm \pm 13	100% Anatase	Dr. Pratim Biswas, Washington University in St. Louis
100 nm \pm 23	100% Anatase	Dr. Pratim Biswas, Washington University in St. Louis
39 nm \pm 10	40% Anatase 60% Rutile	Dr. Pratim Biswas, Washington University in St. Louis
39 nm \pm 10	61% Anatase 39% Rutile	Dr. Pratim Biswas, Washington University in St. Louis
40 nm \pm 16	Amorphous	Dr. Pratim Biswas, Washington University in St. Louis
51 nm \pm 13	100% Rutile	Dr. Xiu Bohkimi , National University of Mexico
Degussa P25 (26 nm \pm 8)	75% Anatase 25% Rutile**	Degussa Corporation
40 nm \pm 14	100% Anatase	Dr. Nina Joshi, UES Inc.

The varying crystalline structures did not show a definable trend in relation to crystal structure and agglomeration size in water or media illustrated in Table 4. The 60 percent rutile TiO₂ showed the smallest agglomeration in de-ionized water with an average hydrodynamic diameter of 519 nm while the amorphous TiO₂ had the highest agglomeration in de-ionized water at 1300 nm (Table 4). As for agglomeration in media, the 100 percent rutile TiO₂ had the smallest agglomeration at an average hydrodynamic diameter of 1110 nm and the largest agglomeration was seen with the 61 percent anatase TiO₂ at 2510 nm (Table 4). Zeta potential values were all at -20 mV or slightly higher, except for the TiO₂ 50 nm 100 percent anatase which had a zeta potential of -13.7 mV (Table 4).

The DLS data for the different sizes of TiO₂ did not show a discernable trend either. The least agglomeration seen in de-ionized water was with the 10 nm TiO₂ particles at 216 nm while the most agglomeration was observed with the 100 nm TiO₂ at 1000 nm (Table 4). In media, the smallest agglomerate sizes were seen with the 50 nm TiO₂ at 1550 nm and the largest was 6.3 nm TiO₂ at 2930 nm. As with the different crystal structure particles, all zeta potential values were negative, when measured using LDV (Table 4). The lowest (most negative) zeta potential was observed with the 6.3 nm TiO₂ at -29.0 mV, followed closely by the 100 nm TiO₂ and the 50 nm TiO₂ at -21.3 mV and -13.7 mV, respectively. The least negative zeta potential value recorded was the 10 nm TiO₂ at only -2.79 mV (Table 4).

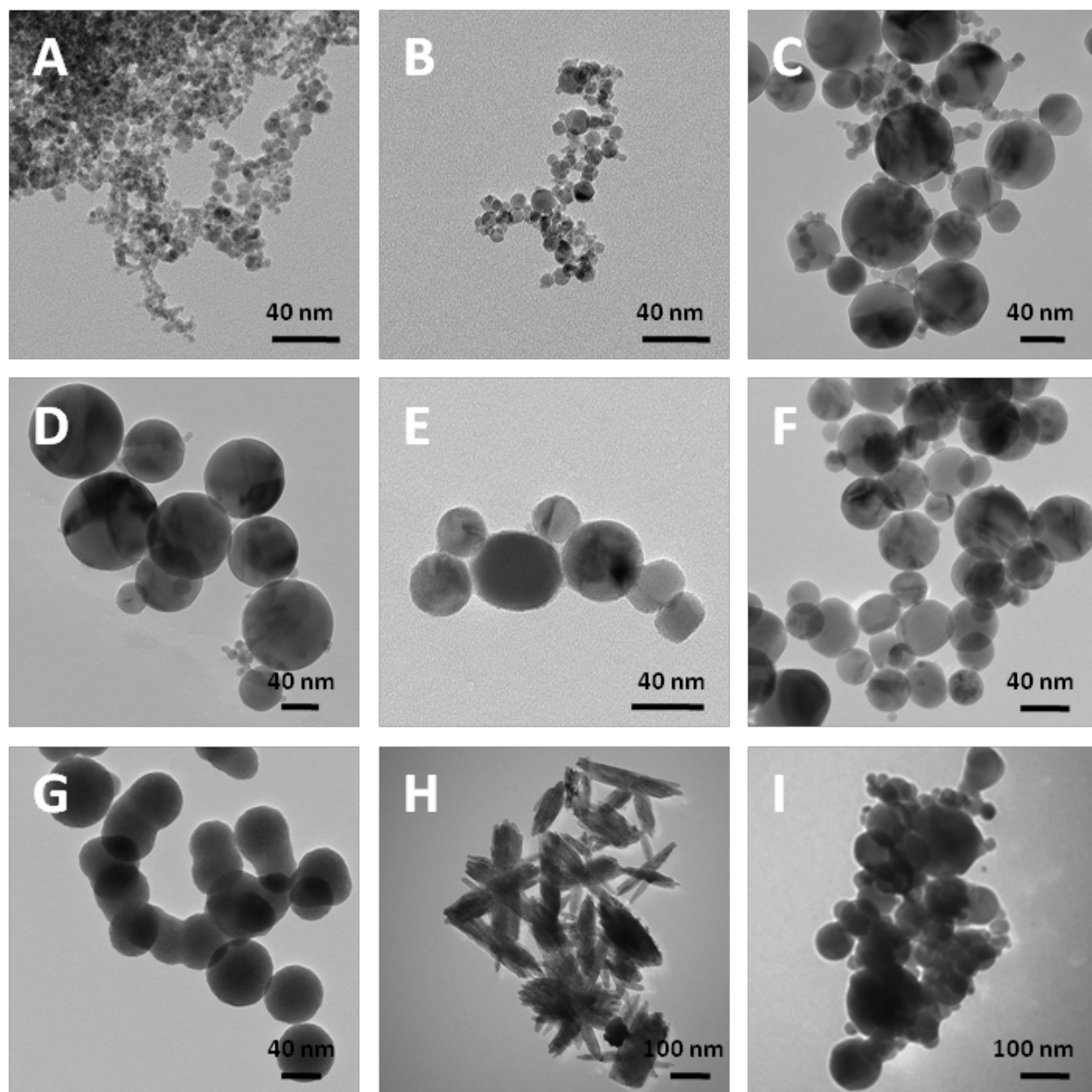


Figure 11. TEM images of the titanium dioxide nanoparticles. A. TiO_2 6.3 nm **B.** TiO_2 10 nm **C.** TiO_2 50 nm **D.** TiO_2 100 nm **E.** TiO_2 39 nm, 40 percent anatase **F.** TiO_2 39 nm, 61 percent anatase **G.** TiO_2 40 nm, amorphous **H.** TiO_2 51 nm, 100 percent rutile **I.** TiO_2 40 nm, ruthenium.

Table 4. Titanium Dioxide Nanoparticle Characterization in Solution. Size measurements performed by DLS and surface charge, or zeta potential, measurements were performed by LDV. **Previously reported values by Murdock et al. [63].

Particle		DLS		LDV	
		Average Diameter (nm)	PDI	Zeta Potential ζ (mV)	Electrophoretic Mobility U (μmcm/(Vs))
Crystallinity	*TiO₂ 40 nm Amorphous				
	DI H ₂ O	1300	0.282	-21.2	-1.66
	DMEM/F-12 Media	2040	0.349	***	***
	*TiO₂ 39 nm, 39% R, 61% A				
	DI H ₂ O	796	0.654	-23.3	-1.83
	DMEM/F-12 Media	2510	0.408	***	***
	*TiO₂ 39 nm, 60% R, 40% A				
	DI H ₂ O	519	0.661	-20.1	-1.58
	DMEM/F-12 Media	2030	0.743	***	***
	*TiO₂ 50 nm 100% A				
	DI H ₂ O	749	0.435	-13.7	-1.07
	DMEM/F-12 Media	1550	0.861	***	***
Size	TiO₂ 51 nm, 100% R				
	DI H ₂ O	582	0.604	-21.8	-1.71
	DMEM/F-12 Media	1110	0.647	***	***
	TiO₂ 6.3 nm				
	DI H ₂ O	476	0.552	-29.0	-2.27
	DMEM/F-12 Media	2930	1	***	***
	TiO₂ 10 nm				
	DI H ₂ O	216	0.439	-2.79	1.63
	DMEM/F-12 Media	1800	0.402	***	***
	TiO₂ 50 nm				
	DI H ₂ O	749	0.435	-13.7	-1.07
	DMEM/F-12 Media	1550	0.861	***	***
Control	TiO₂ 100 nm				
	DI H ₂ O	1000	0.301	-21.3	-1.67
	DMEM/F-12 Media	1800	0.402	***	***
	TiO₂ Degussa				
	DI H ₂ O	542	0.499	19.4	1.52
	DMEM/F-12 Media	3500	0.303	***	***
	TiO₂ Ruthenium				
	DI H ₂ O	663	0.689	-17.9	-1.41
	DMEM/F-12 Media	5870	1	***	***

Uptake and localization of the TiO₂ NPs were evaluated in addition to studying cytotoxicity and mechanisms of toxicity. After a 24 hour of incubation with 10 or 100 $\mu\text{g}/\text{mL}$ of the 60 percent rutile TiO₂ (chosen as a representative particle), thin sections of the cells showed that the TiO₂ NPs are taken up and localized in membrane-bound vacuoles that appear to be endosomes by their size and shape (Fig. 12A,B). In addition after a 24 hour exposure, a cell appeared to be wrapping itself around the NPs suggesting endocytosis as the mechanism of uptake (Fig. 12B). Lastly, Confocal imaging supported endocytosis as the mechanism of uptake since the majority of NPs were localizing in the lysosomes (Fig. 12C). However, there were NPs that were not in the lysosomes. Further imaging studies showed that there were instances of NPs localized in the

mitochondria (Fig. 12D), indicating that mitochondrial function can be altered by the presence of NPs in a cell, which was confirmed by the cell viability data in Figure 13 and summarized in Table 5. The mechanism of cytotoxicity was evaluated by looking at membrane leakage (Fig. 14) and oxidative stress (Fig. 15 and 16).

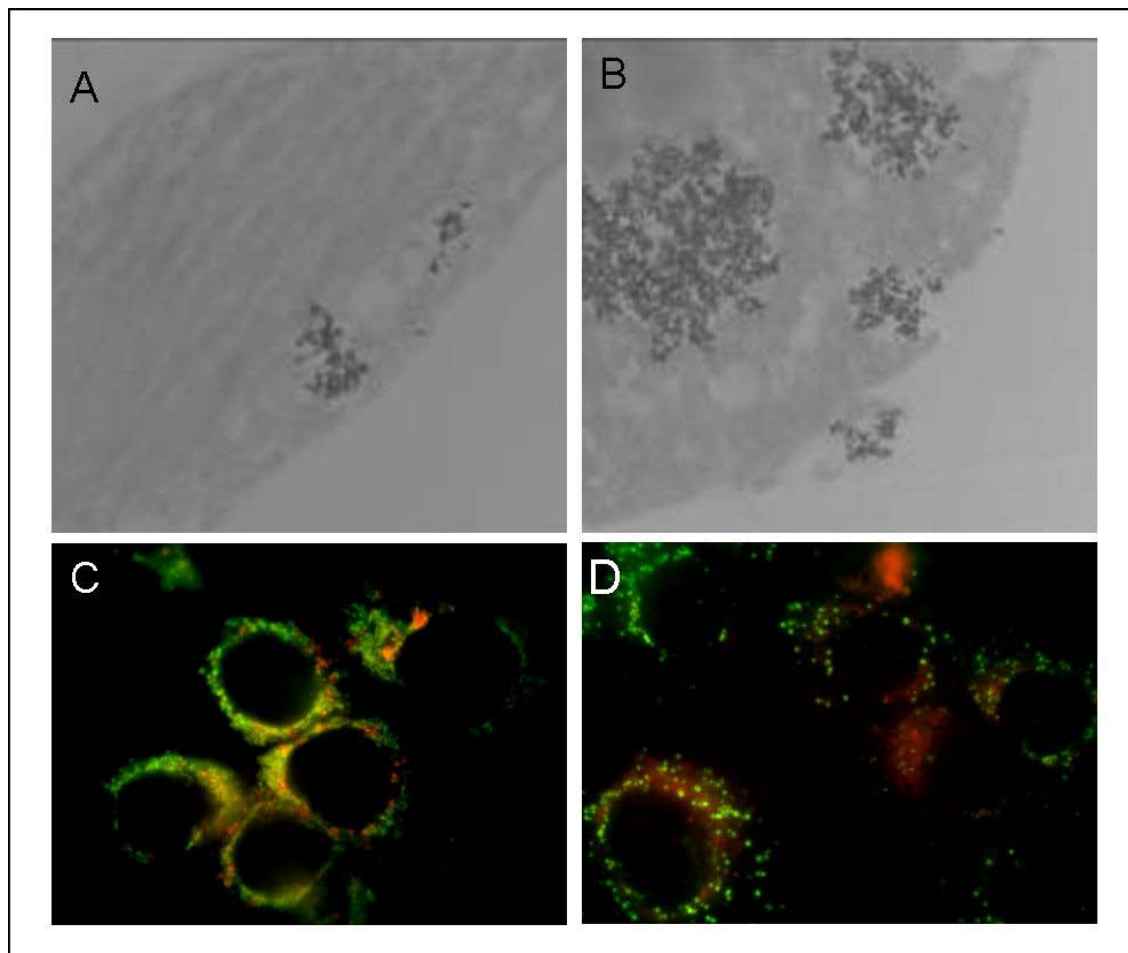


Figure 12. Uptake and localization of titanium dioxide nanoparticles in mouse keratinocytes. **A.** HEL-30 cells treated with 10 µg/mL of 60 percent rutile TiO₂, exposed for 24 h, and evaluated using TEM. The cell has taken up the TiO₂ NPs and they are localizing in membrane-bound vacuoles; **B.** HEL-30 cells treated with 100 µg/mL of 60 percent rutile TiO₂, exposed for 24 h, and evaluated using TEM. The cell appeared to be wrapping itself around the NPs (as shown by the black arrow) suggesting endocytosis as the mechanism of uptake. Furthermore, the NPs were localizing in membrane-bound vacuoles; **C.** Confocal image of mouse keratinocytes treated with TiO₂-Ru labeled NPs and exposed for 24 h. The lysosomes were stained green and the NPs fluoresced red, yellow indicated co-localization. The majority of NPs were localizing in the lysosomes, further suggesting endocytosis as the mechanism of uptake; **D.** Confocal image of mouse keratinocytes treated with TiO₂-Ru labeled NPs and exposed for 24 h. The mitochondria were stained green and the NPs fluoresce red, yellow indicated co-localization. The majority of the mitochondria were free of NPs, however, there were instances of NPs localizing in the mitochondria (as shown by the white arrow) indicating that mitochondrial function can be altered by the presence of NPs in a cell.

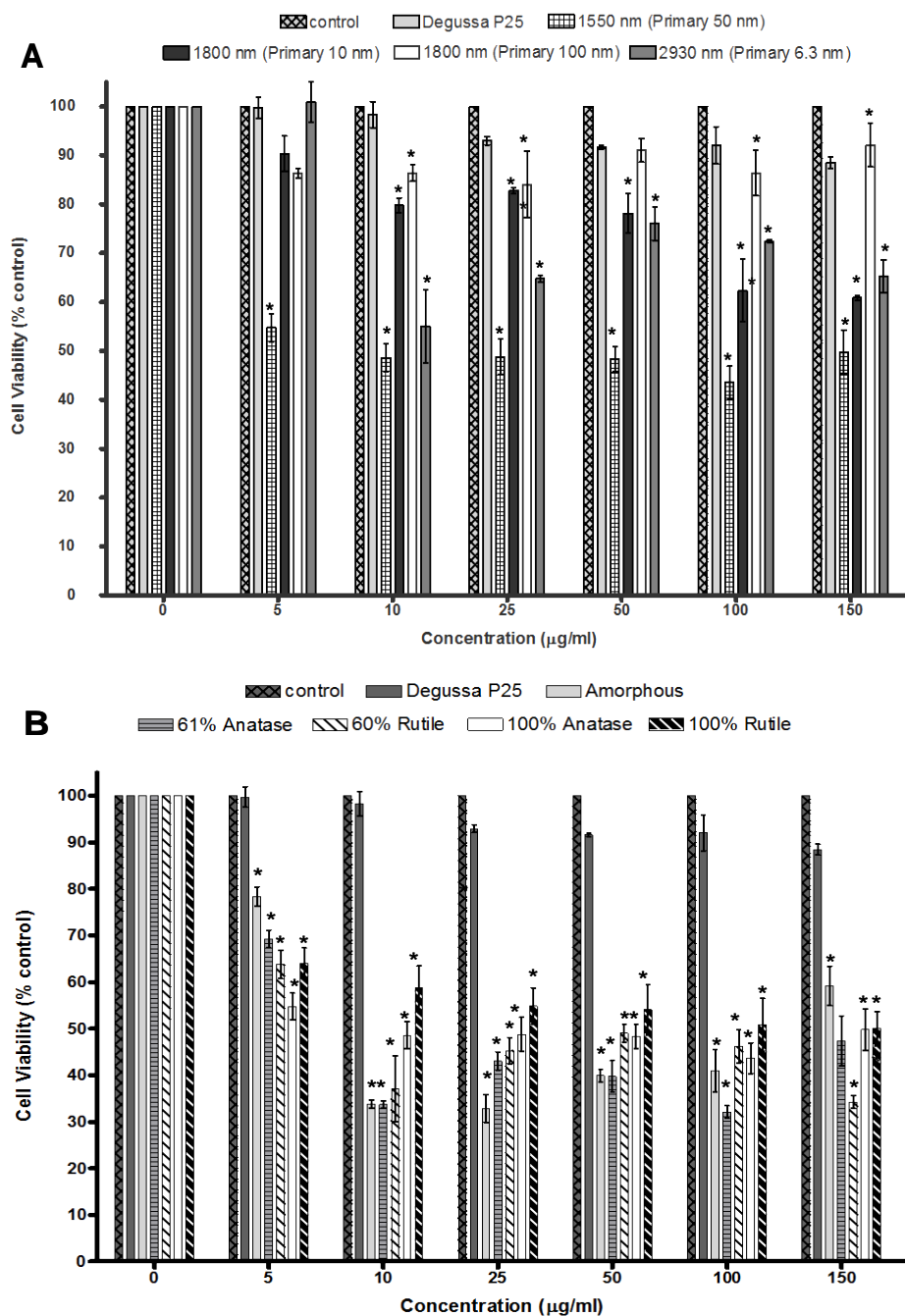


Figure 13. Cell proliferation in mouse keratinocytes treated with titanium dioxide nanoparticles. **A.** Cell proliferation after treatment with 100 percent anatase TiO_2 NPs varying in size. The data demonstrated that at concentrations greater than 10 $\mu\text{g/mL}$, significant cytotoxicity was induced by the different sized TiO_2 NPs in comparison to controls. Furthermore, the 1550 nm (Primary 50 nm) TiO_2 NPs induced cytotoxicity at all concentrations and were significantly more toxic than the other TiO_2 NPs; **B.** Cell proliferation after treatment with TiO_2 NPs with varying crystal structures. The data demonstrated that at all concentrations there was significant cytotoxicity when compared to controls regardless of the crystal structure. Based on this data, regardless of size or crystal structure, TiO_2 is able to induce a toxic response in the HEL-30 cells. *Denotes significance in comparison to control values ($p < 0.01$).

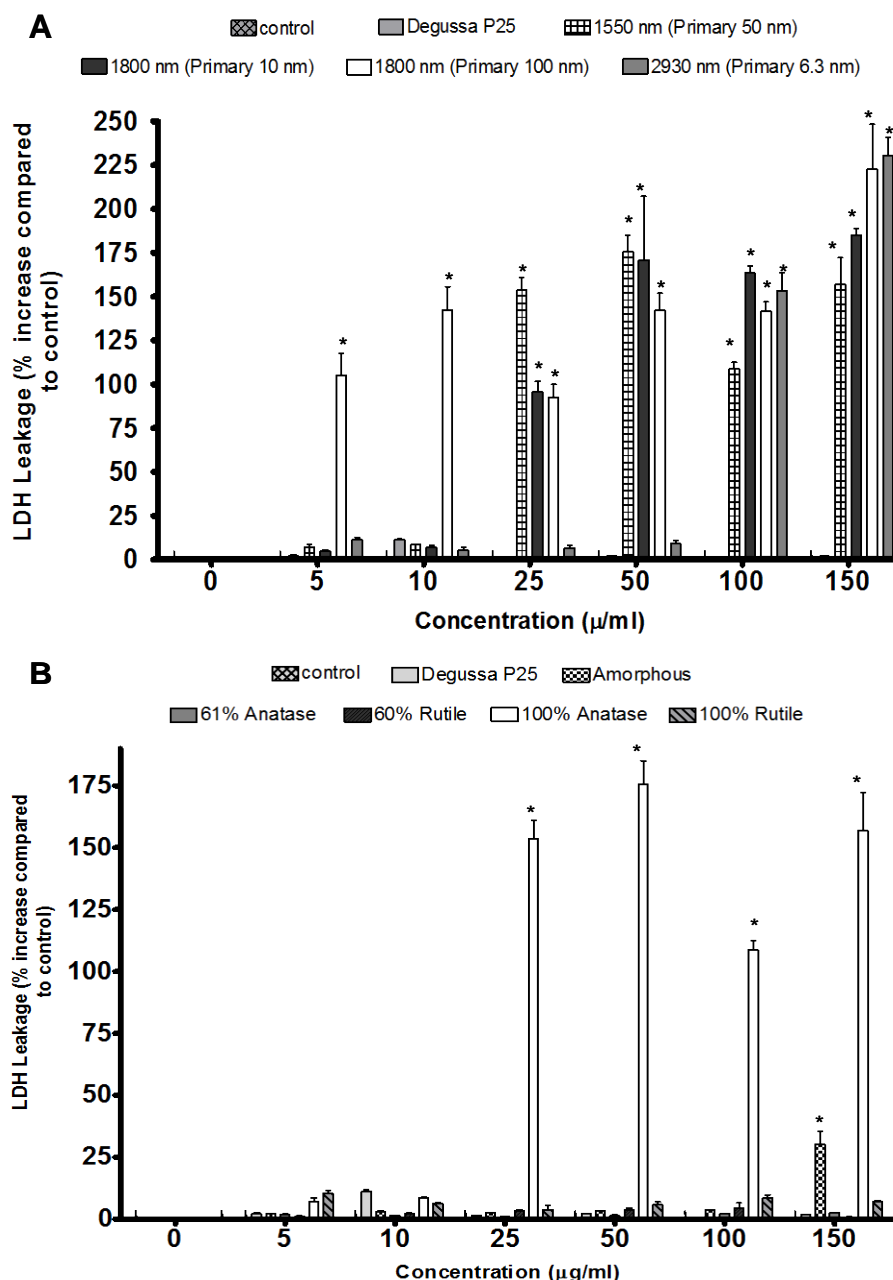


Figure 14. Membrane leakage in mouse keratinocytes treated with titanium dioxide nanoparticles. **A.** Membrane leakage after treatment with 100 percent anatase TiO_2 NPs varying in size. The data here shows that at concentrations $\geq 25 \mu\text{g/mL}$ the 1550 nm (Primary 50nm), 1800 nm (Primary 10 nm) and the 1800 nm (Primary 100 nm) TiO_2 demonstrated significant membrane leakage. Furthermore at very high concentrations ($\geq 100 \mu\text{g/mL}$) so do the 2930 nm (Primary 6.3 nm) TiO_2 ; **B.** Membrane leakage after treatment with TiO_2 NPs with varying crystal structures. The crystal structure membrane leakage data illustrates that LDH leakage is dependent upon crystal structure since at concentrations $\geq 25 \mu\text{g/mL}$ the 100 percent anatase TiO_2 there is highly significant amounts of LDH leakage. In comparison, there is no significant leakage from any form of rutile TiO_2 and the amorphous only demonstrate significant leakage at very high concentrations (150 $\mu\text{g/mL}$). Based on this data, membrane leakage seems to be dependent on crystal structure. *Denotes significance in comparison to control values ($p < 0.01$).

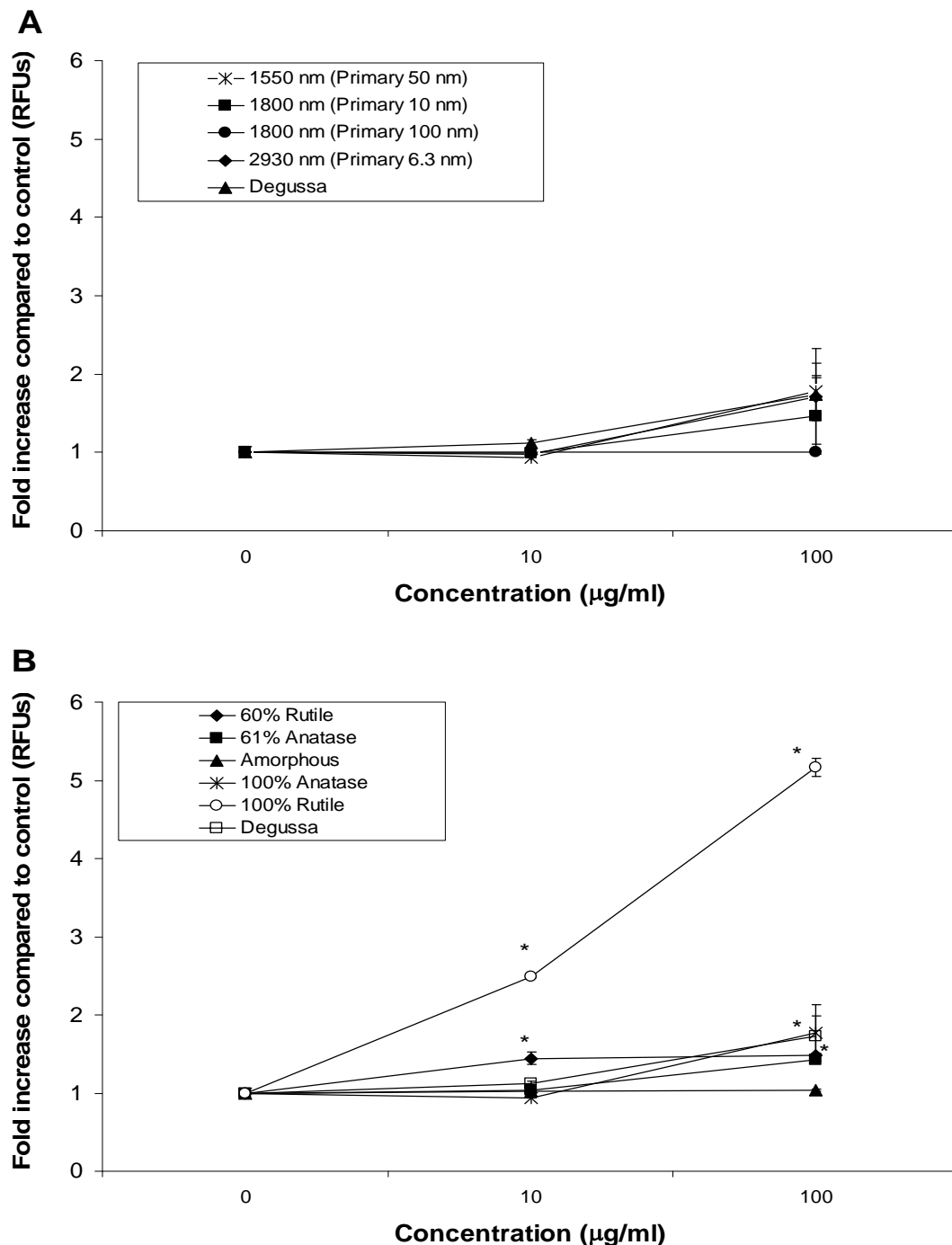


Figure 15. Acellular reactive oxygen species formation in titanium dioxide particles.

A. Production of ROS in different sized 100% anatase TiO_2 NPs. There is no significant ROS production in the different sized 100% anatase NPs at either concentration; **B.** Production of ROS in different crystal structure TiO_2 NPs. There is a significant amount of acellular ROS production seen in the rutile forms of the TiO_2 NPs, with the 100% rutile showing the greatest amount of production. The amorphous and the 100% anatase TiO_2 NPs do not generate any significant production of ROS acellularly. *Denotes significance in comparison to control values ($p < 0.01$).

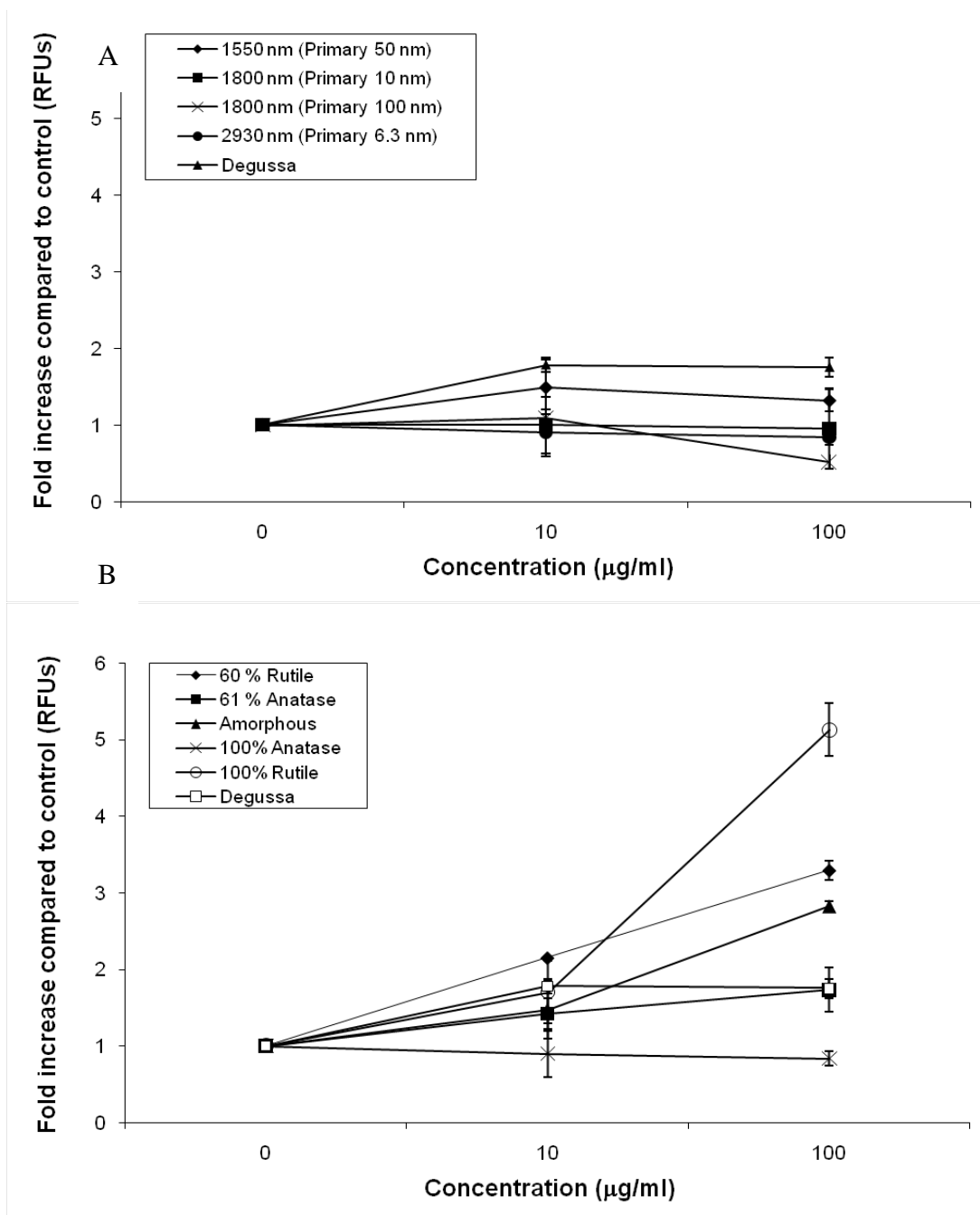


Figure 16. Reactive oxygen species production in mouse keratinocytes treated with titanium dioxide particles. **A.** Formation of ROS in HEL-30 cells treated with different sized 100 percent anatase TiO₂ particles. Only the Degussa P25 TiO₂ NPs generated a significant amount of ROS production when compared to the controls at high concentrations (100 μg/mL); **B.** Formation of ROS in HEL-30 cells treated with different crystal structure TiO₂ particles. There is a significant amount of ROS production seen in the rutile forms of the TiO₂ NPs, with the 100 percent rutile showing the greatest amount of production (p<0.01). At the high concentration (100 μg/mL) the amorphous TiO₂ show significant production of ROS. Based on this data, crystal structure influences the production of ROS generation in the HEL-30 cells. *Denotes significance in comparison to control values (p<0.01).

Because cells produced ROS after exposure to TiO₂ NPs, the ability for addition of an antioxidant (N-Acetyl-L-Cysteine) to improve cell viability was evaluated (Fig. 17).

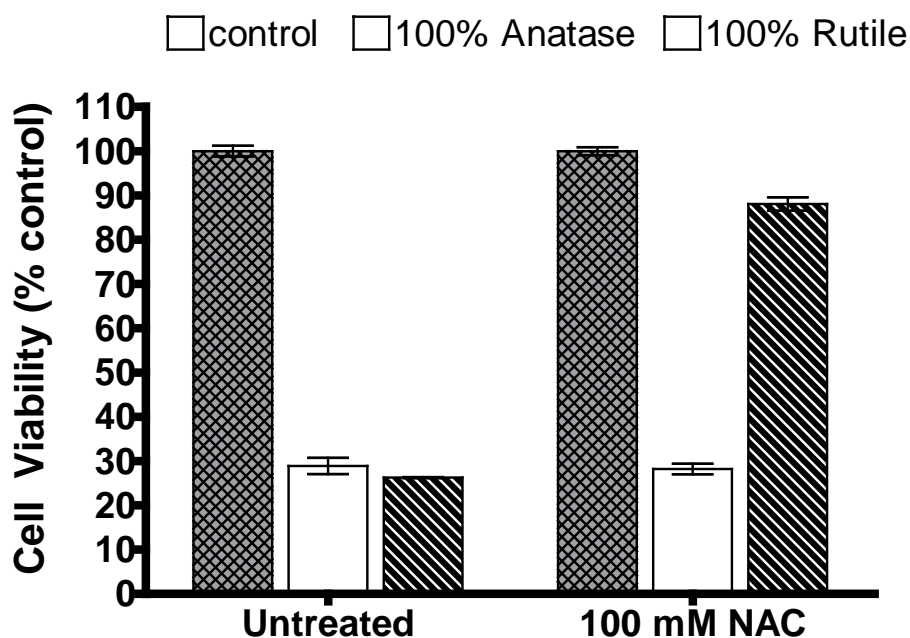


Figure 17. Cell proliferation in mouse keratinocytes treated with titanium dioxide nanoparticles and the antioxidant N-Acetyl-L-Cysteine. There was not a significant toxic response from the cells treated with 100 mM NAC and 100 µg/mL of the 100 percent rutile NPs. However, in the 100 percent anatase TiO₂ NP treatments (100 µg/mL), the NAC was unable to alter the toxicity.

Table 5. Compilation of Nanomaterial Characterization and Cellular Assay Data. Data points for the MTS, LDH, and ROS assays were from the studies with HEL-30 cells dosed at 100 µg/mL. Also, the data for the acellular ROS was performed at the 100 µg/mL concentration.

Particle		Nanoparticle Characterization				Cellular Response to Nanoparticles			Mode of Cell Death
		TEM Average Diameter (nm)	DLS Hydrodynamic Diameter (nm)	LDV Zeta Potential (mV)	Acellular ROS Fold Increase over Control at 100µg/mL	MTS % to Control at 100µg/mL	LDH % to Control at 100µg/mL	ROS Fold Increase over Control at 100µg/mL	
Crystallinity	TiO ₂ 40nm Amorphous	40 ± 16	2040	-21.2	1.04	40.98 ± 7.97	3.71 ± 0.34	2.83	Apoptosis
	TiO ₂ 39nm, 39%R, 61%A	39 ± 10	2510	-23.3	1.42	32.12 ± 2.36	2.12 ± 0.12	1.74	Apoptosis
	TiO ₂ 39nm, 60%R, 40%A	39 ± 10	2030	-20.1	1.49	46.22 ± 6.22	4.39 ± 3.79	3.29	Apoptosis
	TiO ₂ 50nm, 100% A	50 ± 13	1550	-13.7	1.77	43.63 ± 5.72	136.40 ± 48.08	1.32	Necrosis
	TiO ₂ 51nm, 100% R	51 ± 13	1110	-21.8	5.16	50.83 ± 9.79	9.36 ± 2.40	5.13	Apoptosis
Size	TiO ₂ 6.3nm	6.3 ± 1	2930	-29.0	1.71	72.42 ± 0.37	153.28 ± 17.66	0.84	Necrosis
	TiO ₂ 10nm	10 ± 2	1800	-2.79	1.47	62.3 ± 9.07	163.54 ± 6.79	0.95	Necrosis
	TiO ₂ 50nm	50 ± 13	1550	-13.7	1.77	43.63 ± 5.72	136.40 ± 48.08	1.32	Necrosis
	TiO ₂ 100nm	100 ± 23	1800	-21.3	1.00	75.48 ± 0.13	124.50 ± 30.16	0.52	Necrosis
Control	TiO ₂ Degussa P25	30	3500	19.4	1.73	91.92 ± 5.43	0.39 ± 0.22	1.75	Not toxic
	TiO ₂ Ruthenium	40 ± 14	5870	-17.9	***	***	***	***	***

Cellular Impact Level: ■ Low ■ Moderate ■ High

Based on these studies, we know that regardless of size or crystal structure TiO₂ NPs were able to be taken up by the cell and disrupt cell viability, and upon further analysis we saw a size and crystal structure dependent effect on LDH leakage and ROS formation (summarized in Table 5). By assigning a cellular impact level, relative to the data collected, trends and patterns relating the characteristics of the NPs to the matching cellular response assays can more easily be seen and interpreted. This allowed easier determination of the mode of cell death and linking to the characteristics of the NP which may have induced the particular cell responses.

In addition, when describing size dependent toxicity, agglomerate size and primary particle size must be taken into account. When these factors are considered there is a moderate correlation between TiO₂ nano-size and toxicity. While there is no definitive answer between crystal structure and size in terms of cytotoxicity because LDH leakage is most commonly associated with cell death through necrosis [146], and ROS production causes oxidative stress which leads to apoptosis, crystal structure appears to be mediating the mechanism of cell death [61,147]. Since the anatase NPs generate high levels of membrane leakage and do not generate ROS, necrosis is most likely the mechanism of cell death for these NPs. In contrast, the rutile NPs display insignificant levels of membrane leakage and high levels of ROS formation, indicating that apoptosis is the likely mechanism of cell death. Furthermore, when the ROS formation is neutralized by the presence of an antioxidant, cells treated with 100 percent rutile TiO₂ do not show significant levels of toxicity.

The role of nanoparticle charge in gold nanotoxicity

Images acquired via CytoViva showed that NPs were taken up into the cells. They also show changes in morphology in many cases (Fig. 18). The toxicity tests show the 0.8 nm and 1.5 nm gold particles were toxic in a concentration dependent manner, regardless of charge, with the 1.5 nm particles being the most toxic (Fig. 19). Both 0.8 and 1.5 nm showed a significant decrease in cell proliferation and substantial membrane leakage (Fig. 20). However, the 10 nm TMAT gold particles were non-toxic while the 10 nm MES gold particles were toxic in a concentration dependent manner. All gold NPs produced significant ROS, with the exception of 1.5 nm MES and 10 nm TMAT NPs (Fig. 21). Gene expression studies suggest that charge does play a role in the toxicity. The gold NPs are causing DNA damage to the cells, but the cells aren't able to repair themselves, regardless of charge. However, the genes that are affected differ based on charge. The MES (-) particles cause a massive down-regulation of DNA repair genes, and there is no up-regulation on any repair genes. There is some slight up-regulation with the MEEE and TMAT particles (Fig. 22 and Table 6).

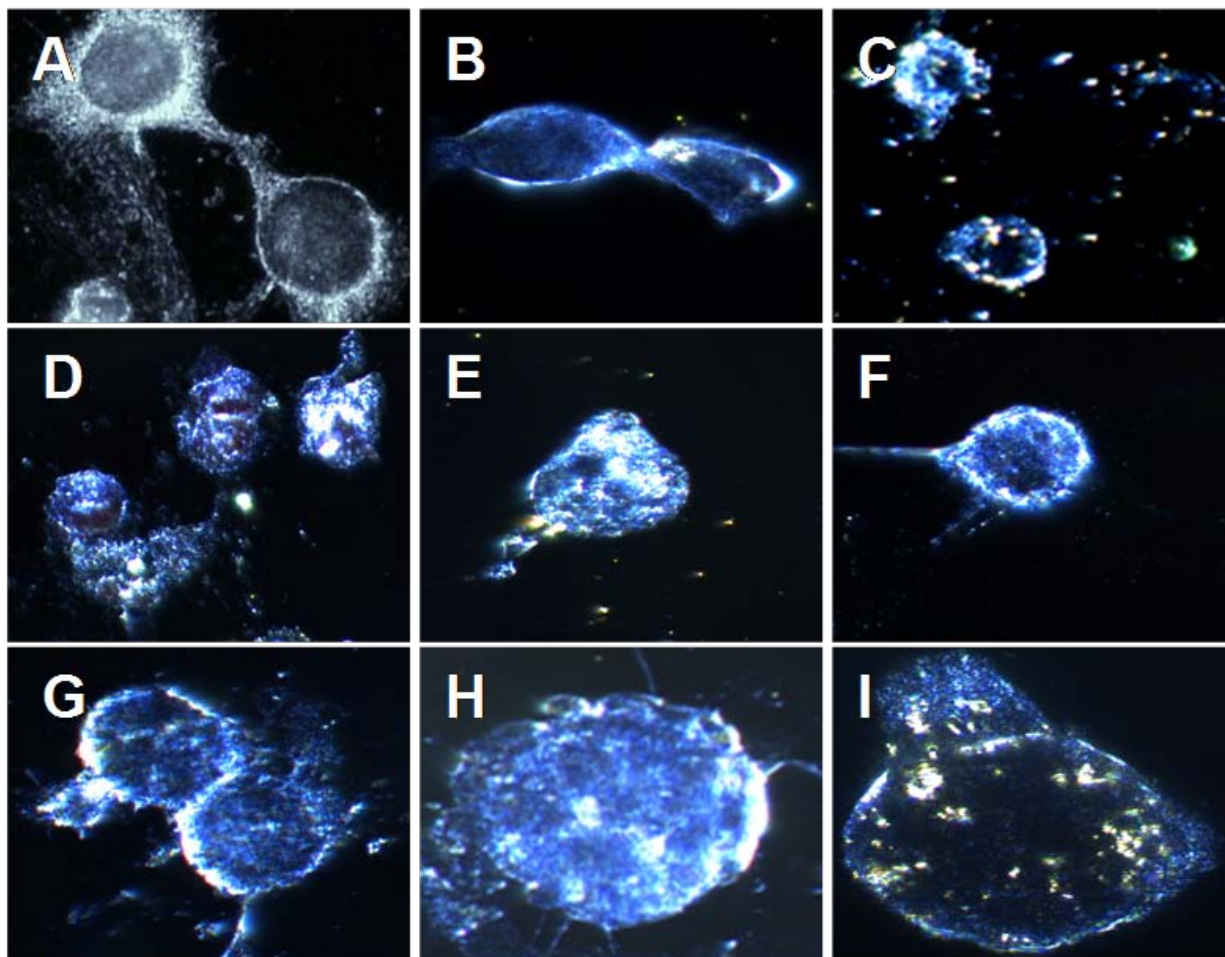


Figure 18. CytoViva images of gold nanoparticles in HaCaT cells. **A.** Untreated HaCaT cells 96X; **B.** HaCaT cells treated with 0.8 nm MEEE Au particles; **C.** HaCaT cells treated with 0.8 nm TMAT Au particles; **D.** HaCaT cells treated with .8nm MES Au particles; **E.** HaCaT cells treated with 1.5 nm MEEE Au particles; **F.** HaCaT cells treated with 1.5 nm TMAT Au particles; **G.** HaCaT cells treated with 1.5 nm MES Au particles; **H.** HaCaT cells treated with 10 nm MEEE Au particles; **I.** HaCaT cells treated with 10 nm TMAT Au particles.

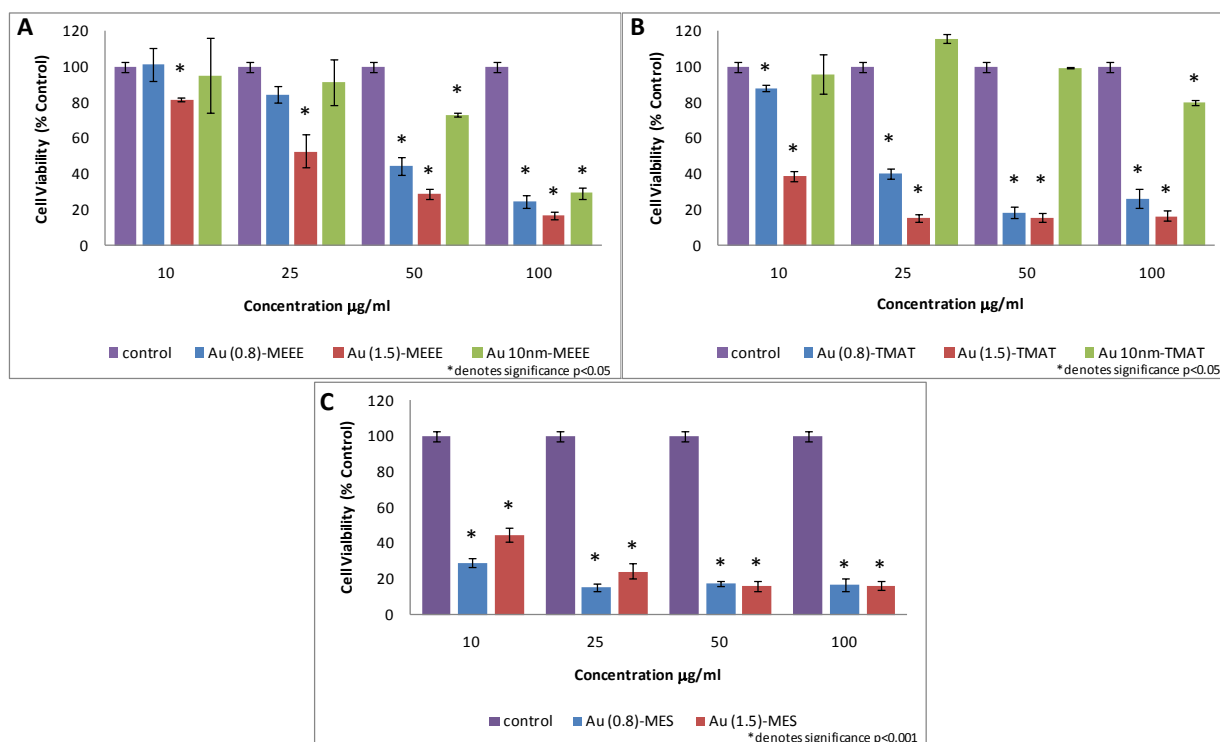


Figure 19. Cell proliferation in HaCaT cells treated with various gold nanoparticles for 24 hours. **A.** Cell proliferation of HaCaT cells dosed with varying concentrations of the Au MEEE NPs. The Au MEEE NPs are toxic to the HaCaT cells in a dose-dependent manner, with toxicity beginning at 25 µg/mL for the 1.5nm particles and at 50 µg/mL for the 0.8 and 10 nm particles; **B.** Cell proliferation of HaCaT cells dosed with varying concentrations of the Au TMAT NPs. The TMAT particles are toxic to the HaCaT cells also in a dose-dependent manner for the 0.8 and 1.5 nm particles, with toxicity beginning at the 10 µg/mL dose for the 1.5 nm particles and at 25 µg/mL for the 0.8 nm particles. The 10 nm TMAT particles do not appear to be toxic to the cells; **C.** Cell proliferation of HaCaT cells dosed with varying concentrations of the gold MES NPs. The MES NPs are toxic to the cells, but not in a dose-dependent manner. This data suggests that both size and charge a role in the toxicity. * denotes significance in comparison to control values where $p < .001$.

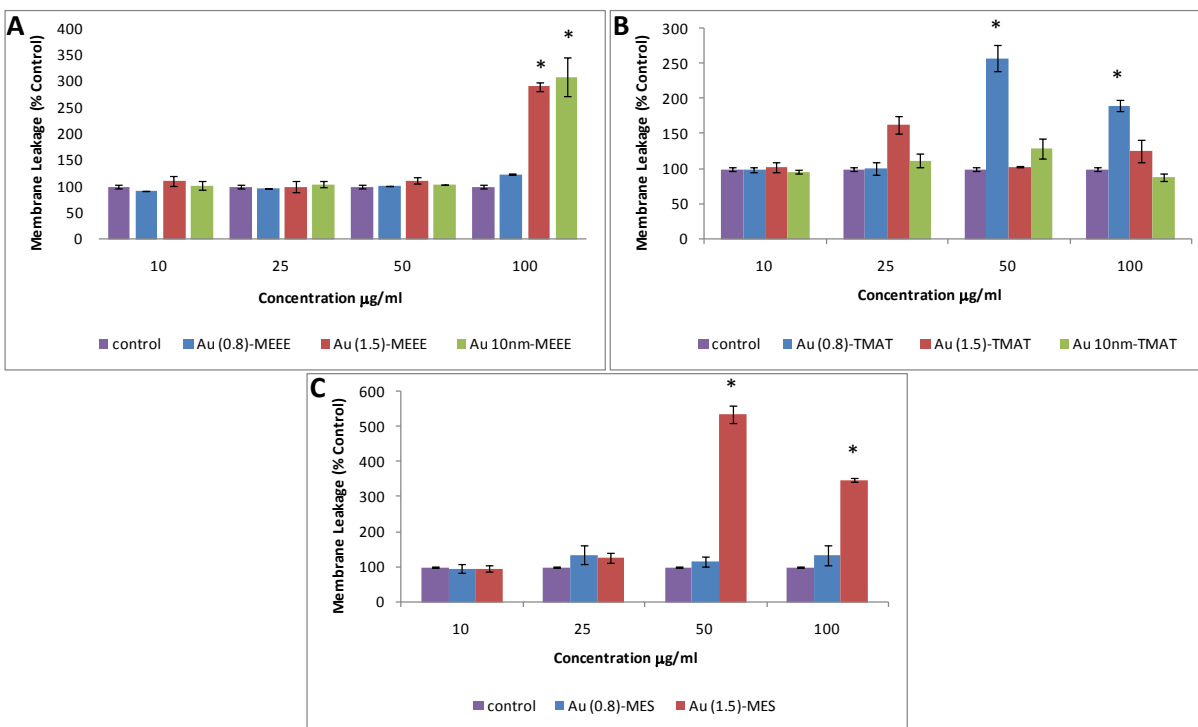


Figure 20. Membrane leakage in HaCaT cells treated with various gold nanoparticles for 24 hours. A. Membrane Leakage in cells treated with varying concentrations of Au MEEE NPs for 24 h. The 1.5 nm and 10 nm MEEE particles show significant amount of membrane leakage at the highest dose of 100 µg/mL, while the 0.8 nm particles do not; B. Membrane leakage in cells treated with varying concentrations of the Au TMAT NPs. Only the 0.8 nm TMAT particles show membrane leakage at the highest dose of 100 µg/mL, while the 1.5 nm and 10 nm TMAT particles do not seem to cause any membrane leakage at any dose. This could mean that death occurs via another mechanism such as apoptosis; C. Membrane leakage in cells treated with varying concentrations of the Au MES NPs. The 1.5nm MES particles begin to show a significant amount of membrane leakage at the 50 µg/mL dose, while 0.8 nm particles do not show any membrane leakage. This indicates that the mechanism of toxicity may not be through necrosis, but rather apoptosis of the cell. *Denotes significance in comparison to control values ($p < 0.05$).

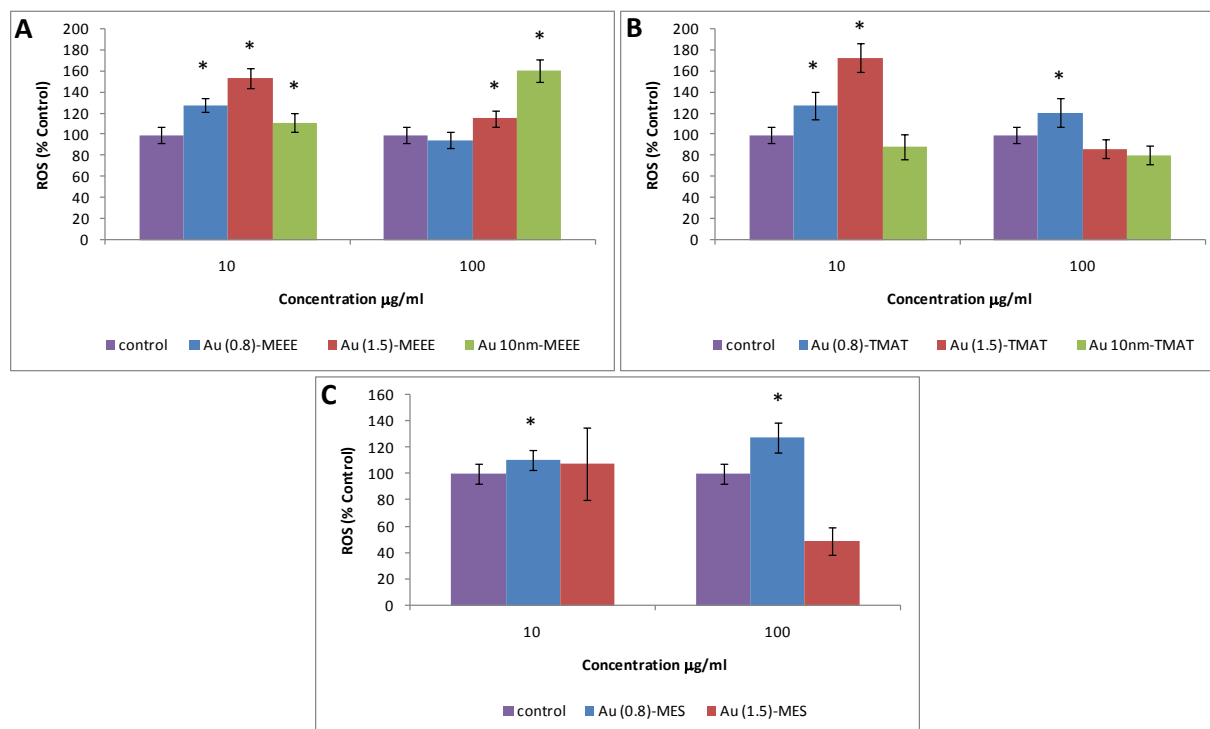


Figure 21. ROS generated in HaCaT cells treated with various gold nanoparticles for 24 hours. **A.** ROS generated by HaCaT cells dosed with MEEE Au NPs at 10 and 100 µg/mL; **B.** ROS generated by HaCaT cells dosed with TMAT Au NPs at 10 and 100 µg/mL ; **C.** ROS generated by HaCaT cells dosed with MES Au NPs at 10 and 100 µg/mL. All Au particles generate significant amounts of ROS at one or both concentrations except for the 1.5 nm MES and 10 nm TMAT particles. This is expected for the 10 nm TMAT because these particles are non-toxic to the cell. The results for the 1.5 nm MES particles are unexpected because these particles are extremely toxic. One explanation for this is that these particles are so toxic that they are fewer live cells to generate ROS. *Denotes significance in comparison to control values ($p < 0.05$).

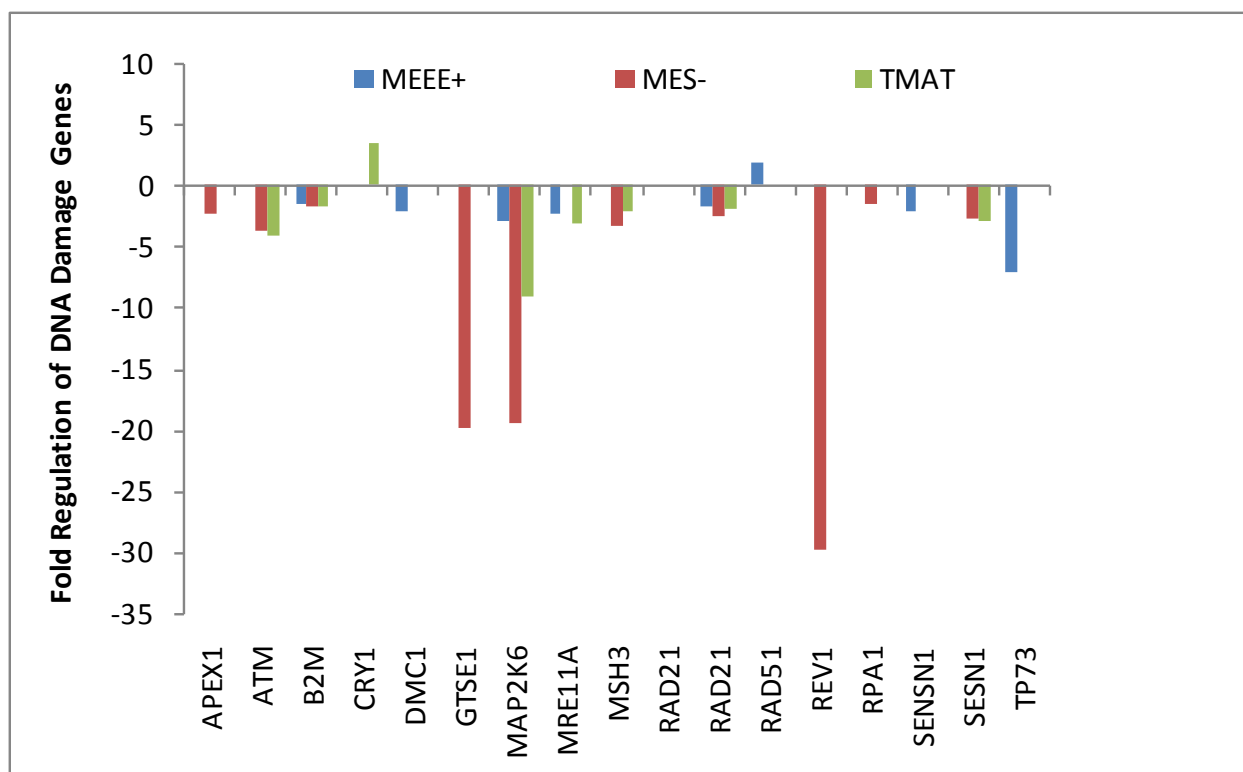


Figure 22. Changes in gene expression of DNA damage genes after 24 hour exposure to 1.5 nm Au nanoparticles. A total of 14 genes were up/down-regulated. The gold NPs are causing DNA damage to the cells, but the cells aren't able to repair themselves, regardless of charge. However, the genes that are affected differ based on charge. The MES (-) particles cause a massive down-regulation of DNA repair genes, and there is no up-regulation on any repair genes. There is some slight up-regulation with the MEEE and TMAT particles.

Table 6. List of DNA Damage Genes Up and Down-Regulated and Their Functions.

Gene Function	Gene Name
Apoptosis	ATM, MAP 2 K6, SESN 1, TP 73
DNA Repair	CRY 1, RAD 21, APEX 1, REV 1, RPA 1
Double Strand Break Repair	MRE 11A
Mismatch Repair	MSH 3
Cell Cycle Checkpoint	RAD 21, SESN 1, GTSE 1, TP 73
Damaged DNA Binding	RAD 51

Shape matters: Differential cytotoxicity observed in gold nanospheres and nanorods

Gold NPs of varying shapes (nanospheres and nanorods) and sizes were synthesized by Dr. Robert MacCuspie and Dr. Kyoungweon Park from AFRL/RXBN (Table 7 and 8). TEM images of each particle was provided by Dr. Robert MacCuspie to show the morphology (Fig. 23 and 24).

Table 7. Gold Nanospheres with Different Ligands and Their Concentrations

Particle Name	RM1	RM2	RM3	RM4
Ligand	Citrate	MPS	MPS+Tripentylamine (T5)	MPS+Trihexylamine (T6)
Concentration	0.411 mg/mL	0.336 mg/mL	0.227 mg/mL	0.469 mg/mL
Size	12 nm	12 nm	12 nm	12 nm

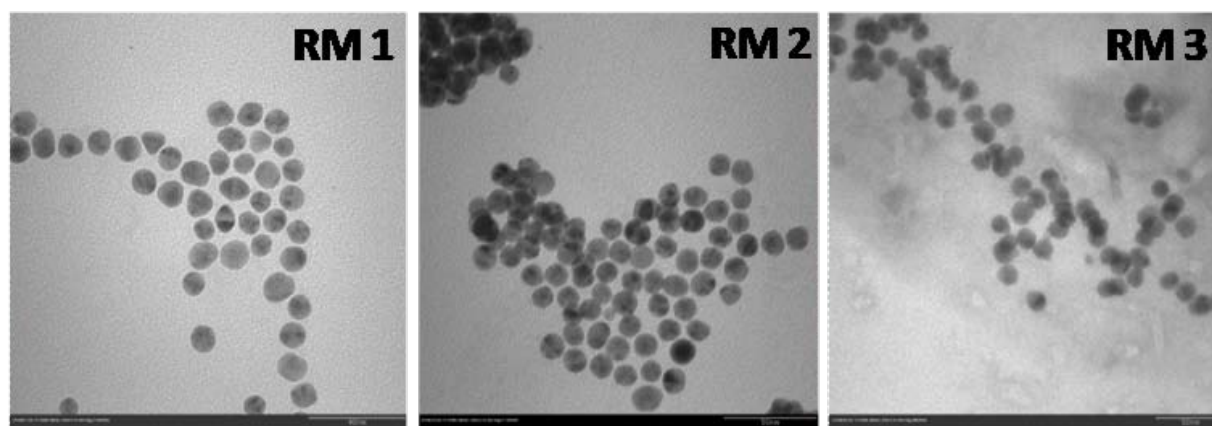


Figure 23. TEM images of the nanospheres. Images provided by Dr. Robert MacCuspie.

Table 8. Gold Nanorods with Different Ligands and Their Concentrations.

Particle Name		TT_S1	TT_S2	TT_S3	TT_S4, 5, 6
Size	Length	54.8 \pm 7.1	39.2 \pm 2.9	78.8 \pm 15.2	51.2 \pm 6.2
	Diameter	20.1 \pm 5.1	9.5 \pm 0.6	12.5 \pm 4.3	24.3 \pm 3.4
	L/D	2.9 \pm 0.66	4.2 \pm 0.45	6.5 \pm 1.8	2.1 \pm 0.3
Capping Molecules		CTAB	CTAB	CTAB/BDAC	CTAB
Particle Concentration		0.548 mg/mL	0.103 mg/mL	0.315 mg/mL	2.2 mg/mL

(CTAB: Hexadecyltrimethylammonium bromide, BDAC: Benzyldimethylhexadecylammonium chloride)

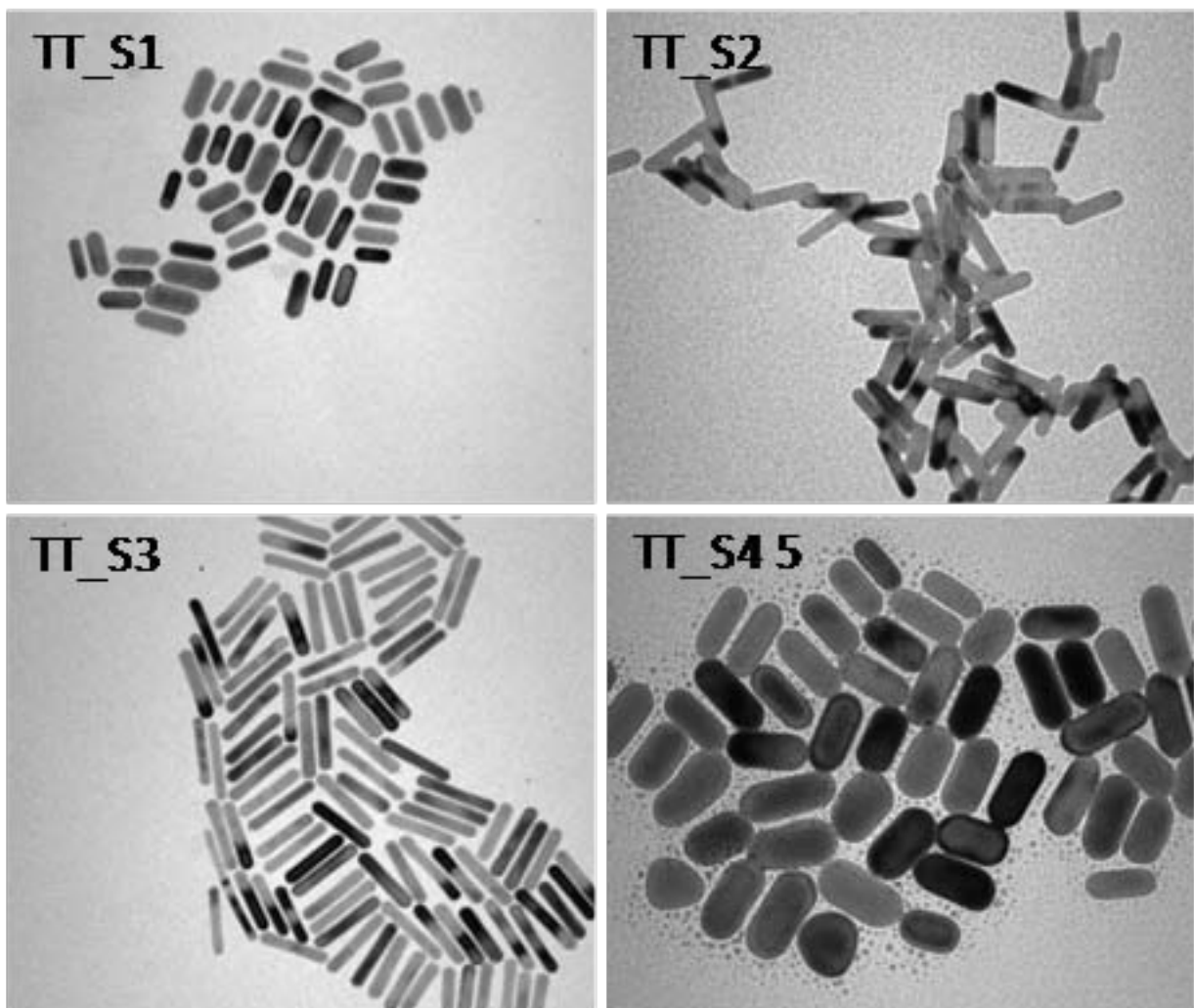


Figure 24. TEM images of the gold nanorods. Images provided by Dr. Kyoungweon Park.

Cytoviva was used to show the interaction of gold nanospheres and nanorods with cells (Fig. 25 and 26). Images show that the NPs agglomerate in cell media. There appears to be some interaction between the agglomerates and cells.

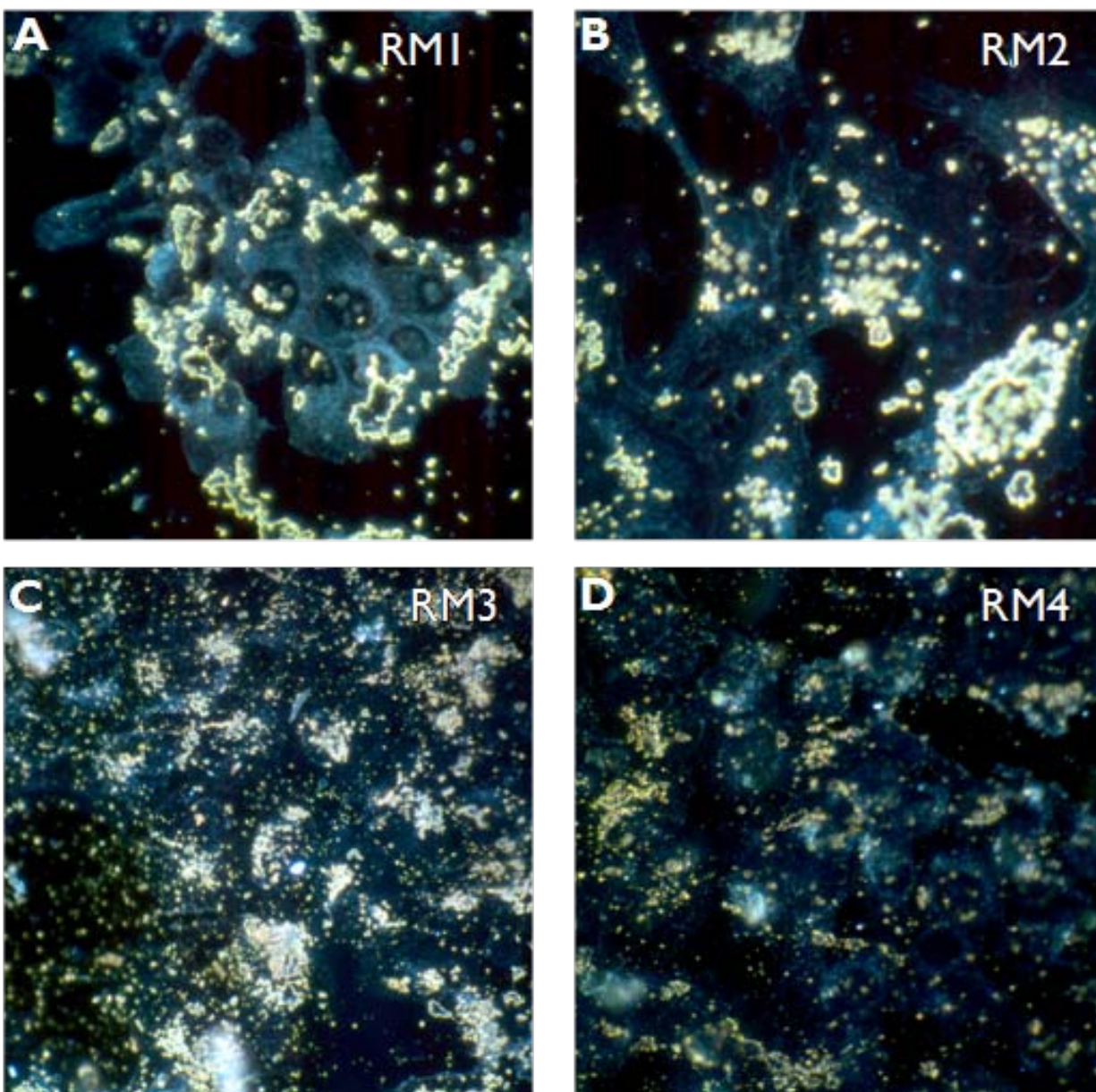


Figure 25. CytoViva images of gold nanospheres. **A.** HaCaT cells treated with RM1 Au nanospheres; **B.** HaCaT cells treated with RM2 Au nanospheres; **C.** HaCaT cells treated with RM3 Au nanospheres; **D.** HaCaT cells treated with RM4 Au nanospheres.

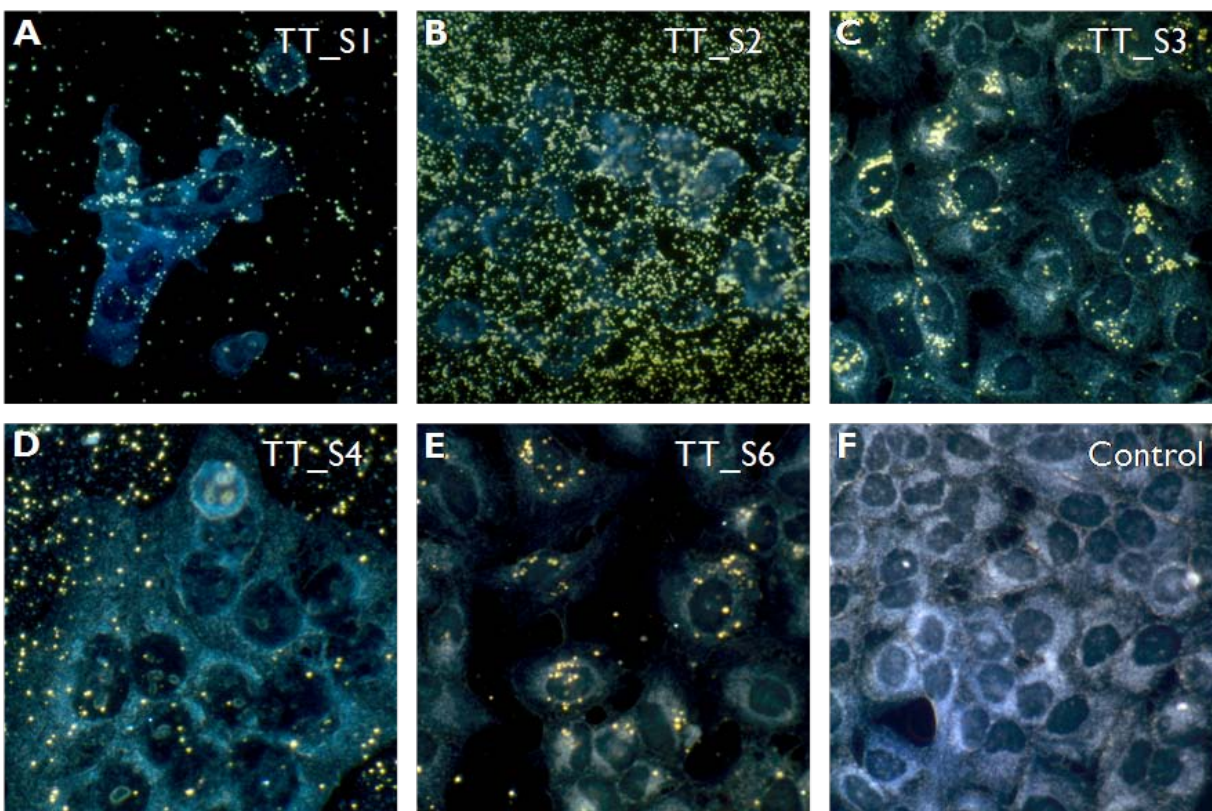


Figure 26. CytoViva images of gold nanorods. A. HaCaT cells treated with TT_S1 Au nanorods; B. HaCaT cells treated with TT_S2 Au nanorods; C. HaCaT cells treated with TT_S3 Au nanorods; D. HaCaT cells treated with TT_S4 Au nanorods; E. HaCaT cells treated with TT_S5 Au nanorods; F. Untreated HaCaT cells.

The MTS assay which measured mitochondrial function and directly relates to cell proliferation, demonstrated that the 12 nm nanospheres did not disrupt cell proliferation while the nanorods, regardless of size, reduced proliferation (Fig. 27 and 28). A similar trend was observed with the LDH membrane leakage assay which measures membrane integrity (Fig. 29 and 30). In addition, the nanorods were toxic at very low doses and did not display much of a dose-dependent effect. Four out of the six nanorods were toxic at the lowest dose of 5 $\mu\text{g/mL}$ with the other two displaying toxicity as early as 10 and 25 $\mu\text{g/mL}$ respectively. The ROS studies confirmed the results obtained from both the MTS and LDH assays. Based on the initial observations of this study, shape seems to play a role in contributing to nanomaterial toxicity.

The ROS assay was used to compare the amount of oxidative stress produced in cells exposed to the different gold NPs. It was found that the nanospheres did not generate ROS (Fig. 31), while three of the nanorods either increased or decreased the generation of ROS compared to control (Fig. 32).

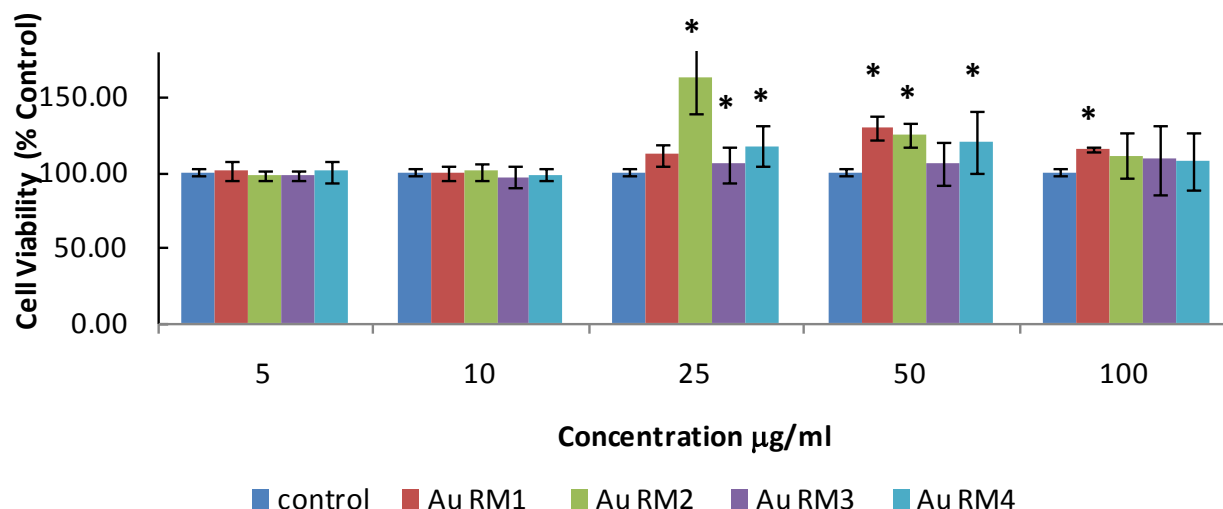


Figure 27. Cell viability after 24 hour exposure to Au nanospheres.

There is no significant decrease in cell proliferation after exposure to any of the nanospheres. In contrast, it appears that the nanospheres actually increase the rate of cell proliferation. *Denotes significance in comparison to control values ($p < 0.05$).

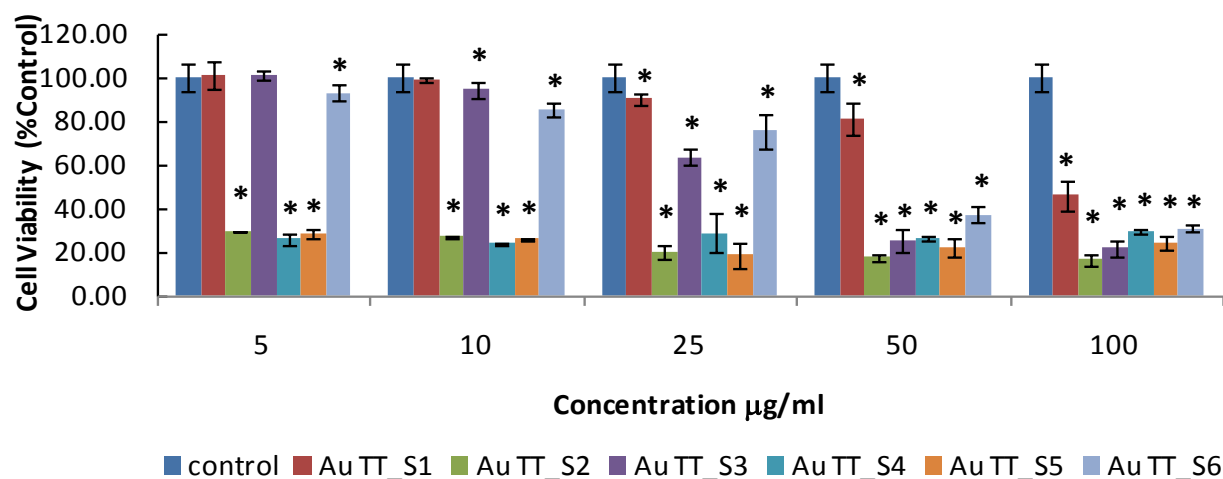


Figure 28. Cell proliferation in HaCaT cells after 24 hour exposure to Au nanorods.

All the nanorods significantly reduce cell viability. TT_S2, S4 and S5 are extremely toxic to the cells, causing a 70 percent decrease in cell viability at the lowest dose of 5 µg/mL, while TT_S1, S3, and S6 cause a dose-dependent decrease in cell viability. *Denotes significance in comparison to control values ($p < 0.05$).

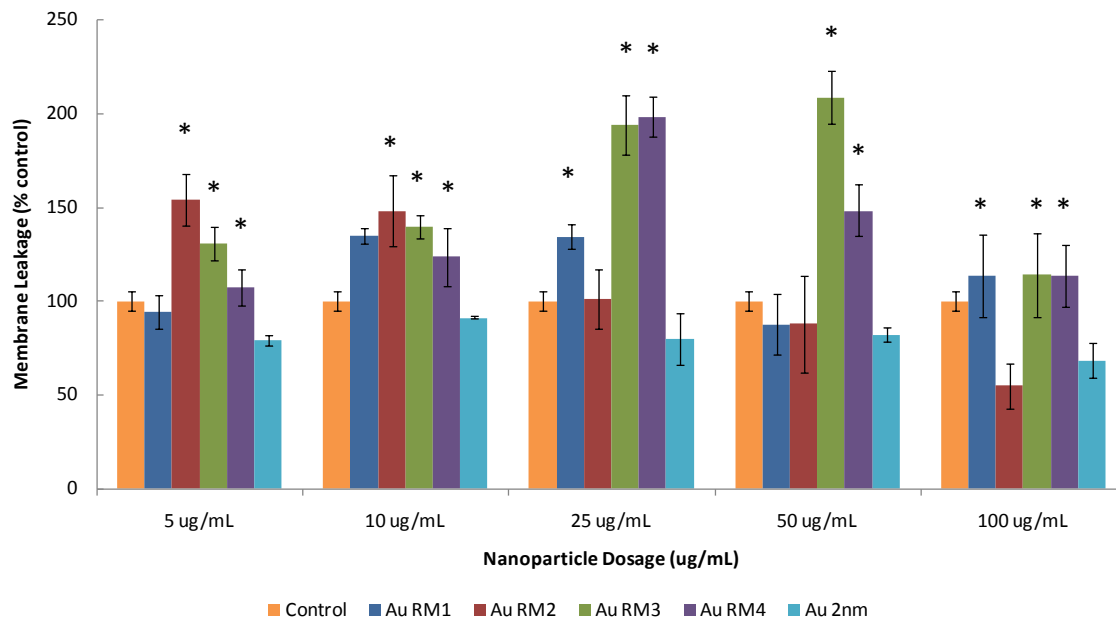


Figure 29. Membrane leakage in HaCaT cells after 24 hour exposure to Au nanospheres. The LDH results show an increase in membrane leakage after exposure to all particles except the 2 nm negative control particles, but there does not seem to be a discernible pattern for any of the nanospheres. *Denotes significance in comparison to control values ($p < 0.05$).

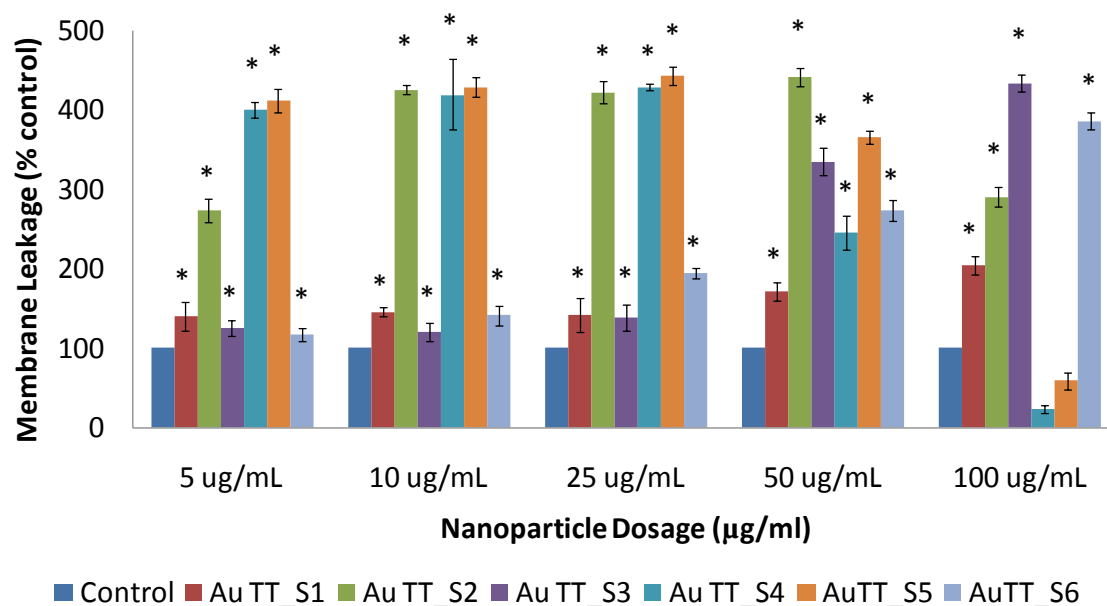


Figure 30. Membrane leakage in HaCaT cells after 24 hour exposure to Au nanorods. The LDH results show a significant amount of membrane leakage after exposure to all of the particles, starting at the lowest dose of 5 $\mu\text{g/mL}$. These results also correspond to the MTS results in that TT_S2, 4, and 5 show significantly more membrane leakage (300-500 percent as compared to the control) than S1, 3 and 6. The amount of leakage dramatically decreases to almost nothing at the highest dose for S4 and S5. This could be because all the cells are dead, therefore there are no cells left to leak. *Denotes significance in comparison to control values ($p < 0.05$).

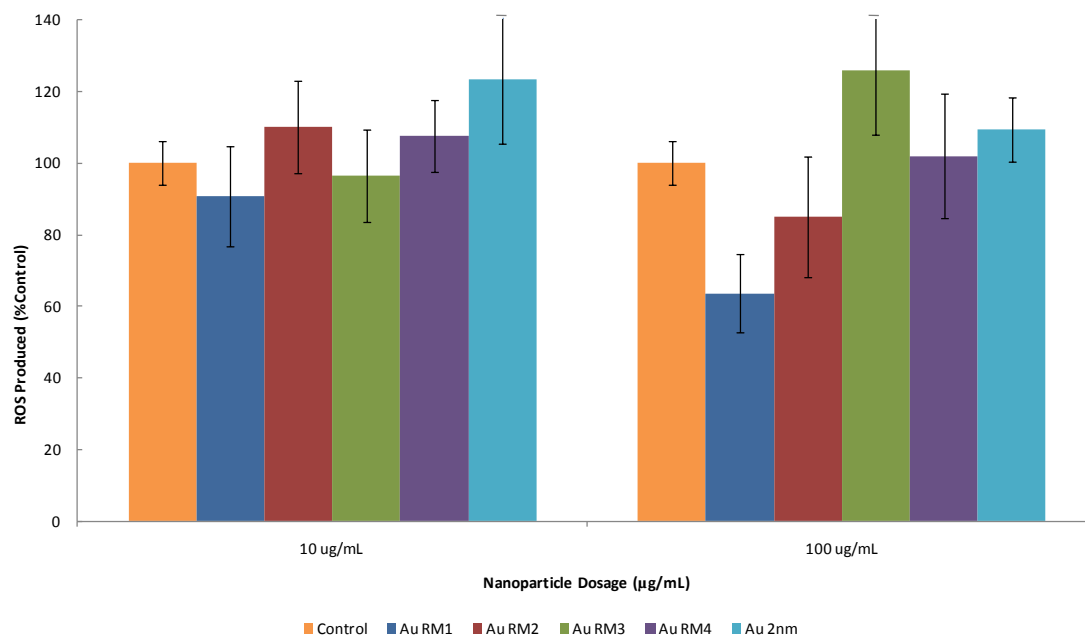


Figure 31. ROS generated in human keratinocytes after 24 hour exposure to Au nanospheres. The ROS assay shows there is no significant amount of reactive oxygen species generated after exposure to any of the nanospheres.

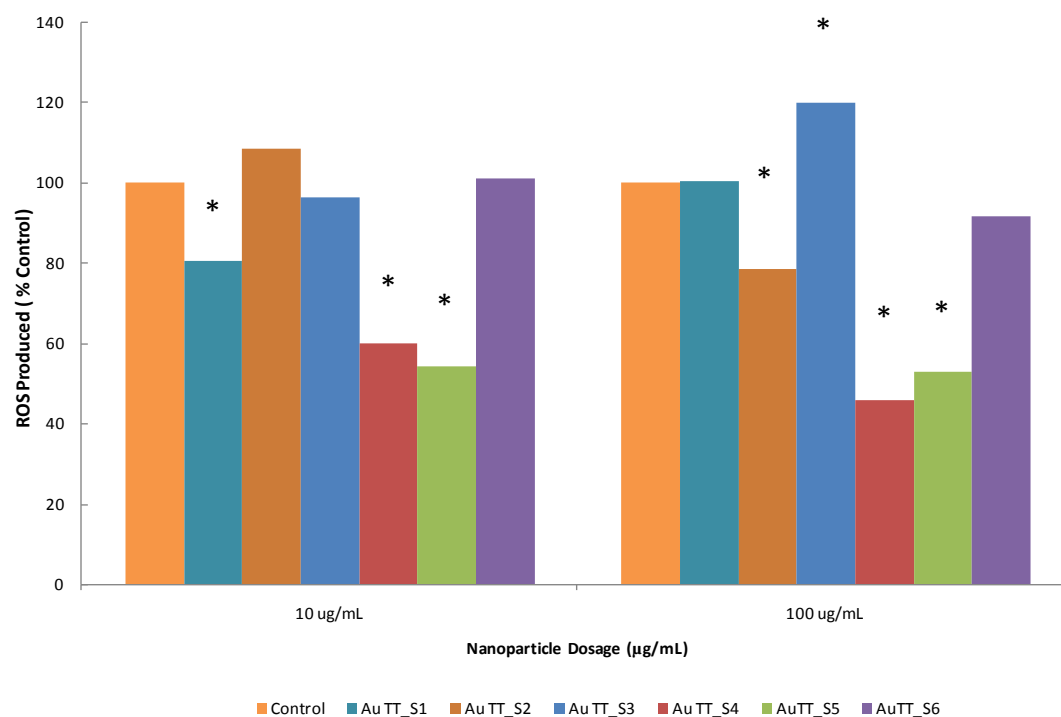


Figure 32. ROS generated in human keratinocytes after 24 hour exposure to Au nanorods. The ROS studies show that only the TT_S3 show a significant increase in the amount of ROS generated. However, TT_S2, S4 and S5 show a significant decrease in the amount of ROS generated as compared to the control. This coincides with the MTS and LDH results for these particles. The particles are so toxic to the cells that there are no cells present to generate ROS. *Denotes significance in comparison to control values ($p < 0.05$).

Toxicity of amorphous silica nanoparticles in mouse keratinocytes

DLS and TEM were used to characterize silica NP sizes shown in Table 9. No changes in particle sizes were observed in water versus dosing media with the exception of the 30 nm particle solutions, which were estimated to be 28.9 nm in water and 39 nm in the media by DLS. Average particle size was similar between the two methods, indicating silica does not agglomerate significantly in water. Figures 33 and 34 provide TEM images of monodispersed silica NPs in water, and the average particle size with standard deviation, respectively.

Table 9. Particle Sizes of Silicon Dioxide in Water and Dosing Media. Average particle size was measured using DLS and TEM.

Instrumentation		DLS		Microscope	(TEM)
Particle		Average Diameter (nm)	PDI	Average Diameter (nm)	SD
SiO ₂ A	Water	28.9	0.093	30.3	1.2
	Media	39.0	0.116	na	na
SiO ₂ B	Water	52.9	0.07	47.7	3.2
	Media	51.9	0.069	na	na
SiO ₂ C	Water	121	0.007	118	6.1
	Media	119	0.018	na	na
SiO ₂ D	Water	537	0.438	535	13.4

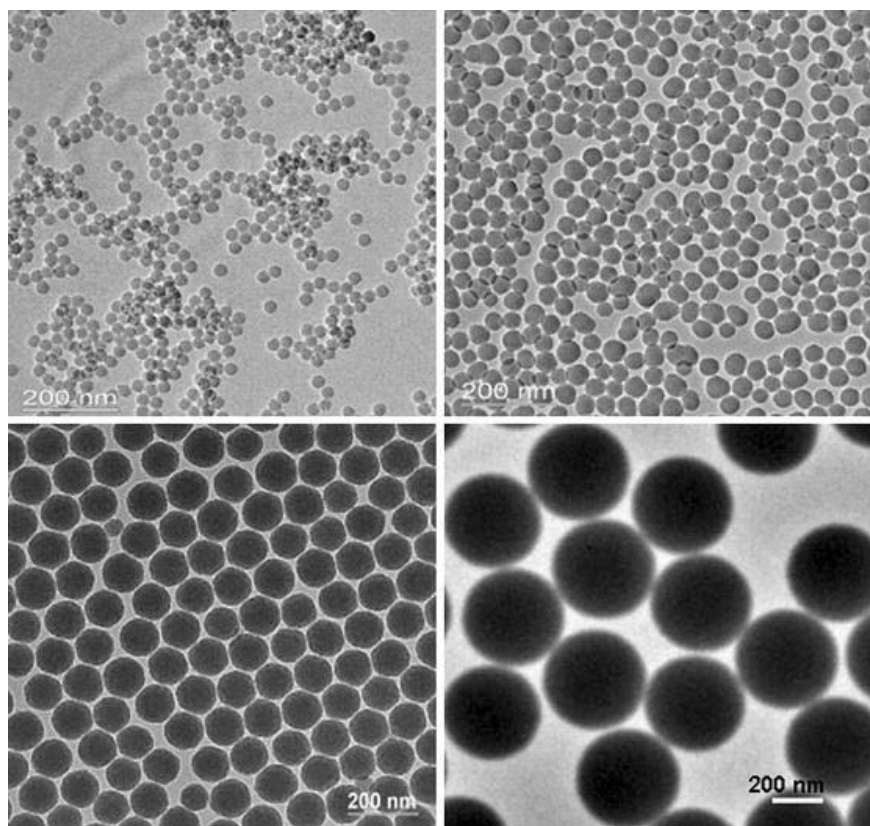


Figure 33. Transmission electron microscopy of SiO₂ spheres.

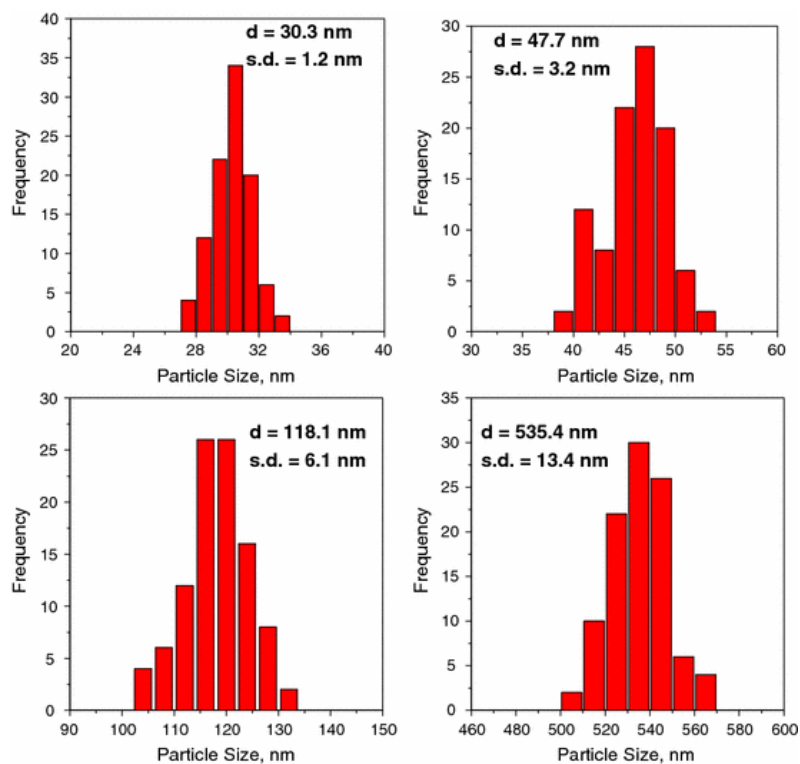


Figure 34. The average particle size (d) and the standard deviation determined using TEM by analyzing over 300 particles.

To verify the uptake of NPs, cells were incubated with 100 $\mu\text{g/mL}$ of silica NPs for 24 hours, followed by imaging with TEM (Fig. 35). Cells show internalization of all of the different sizes of silica NPs into intracytoplasmic vacuoles or endosomes. There was no evidence of silica NPs in the nucleus, but they could be found randomly in the cytoplasm. Higher magnification insets of the selected areas show individual 535 nm silica NPs (Fig. 35D) while all of the smaller-sized silica NPs (30, 48, and 118 nm) were found in loose aggregates containing multiple NPs, in some instances with retention of the characteristic NP sizes and shapes. (Fig. 35A-C).

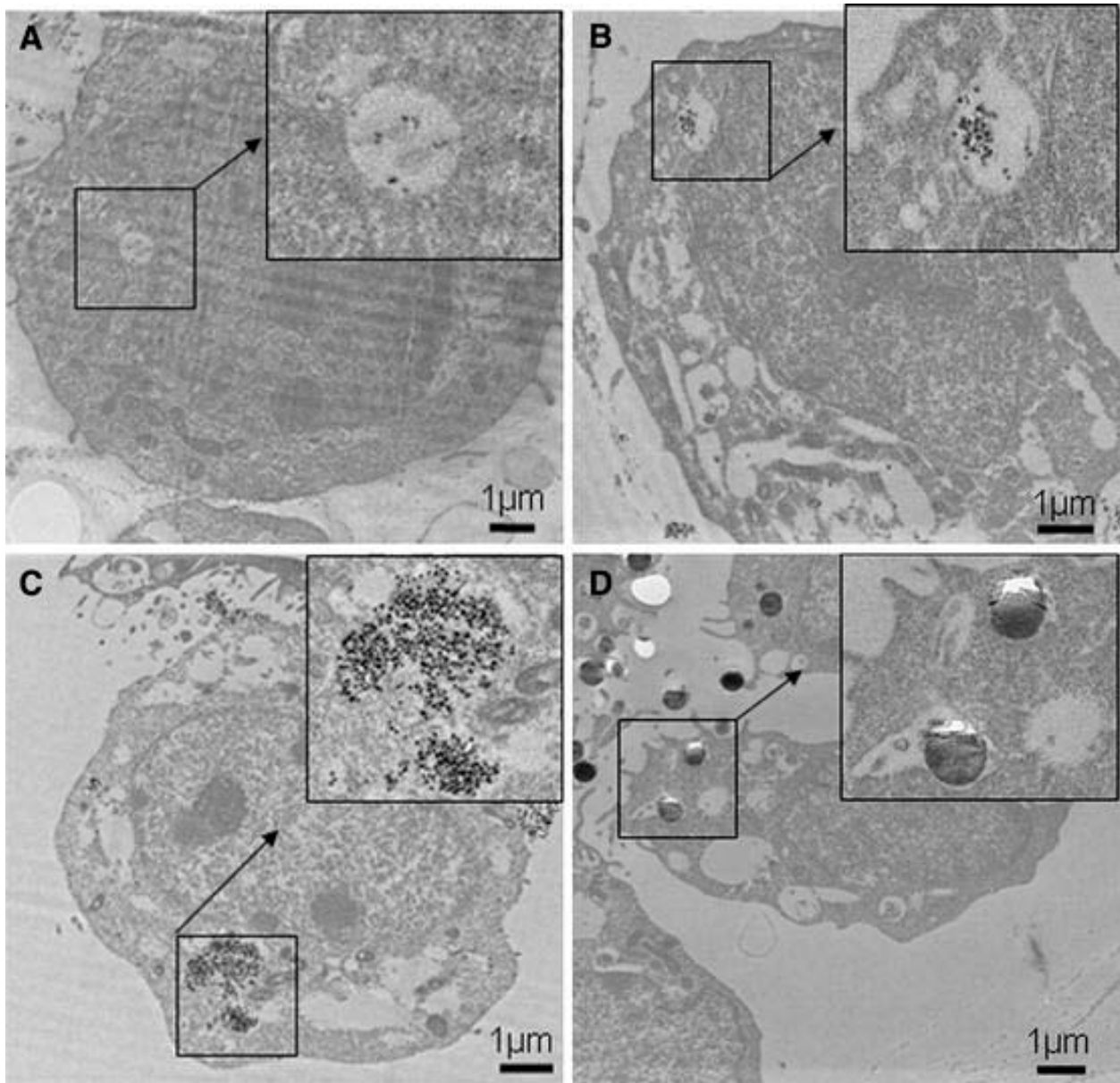


Figure 35. Transmission electron microscopy of HEL-30 cells incubated with 100 $\mu\text{g/mL}$ of silica nanoparticles for 24 hours showing internalization of all sizes used in this study. A. 30 nm SiO₂; B. 48 nm SiO₂; C. 118 nm SiO₂; and D. 535 nm SiO₂. Boxes provide higher magnification images correspond to the areas inside the box.

The effects of silica NPs on cell membrane integrity are shown in figure 36. At a concentration of 100 $\mu\text{g/mL}$, membrane leakage of LDH was 43, 30, 7 and 8 percent of the control, decreasing with increasing size of silica particles. The smallest size at the highest concentration (30 nm at 200 $\mu\text{g/mL}$) presented the most toxic effect as indicated by LDH measurements. There was a strong correlation between particle sizes and the reduction of MTT (Fig. 37). At 200 $\mu\text{g/mL}$, 30 and 48 nm particles induced significant MTT reductions of 30 and 50 percent, respectively, which was increased to 42 and 55 percent, respectively at 100 $\mu\text{g/mL}$. The two smallest dimensions tested showed significant toxicities while the two larger sizes (118 and 535 nm) did not demonstrate toxicity as indicated by MTT reduction. Figure 38 depicts correlation between LDH and MTT for cytotoxicity. There was a strong correlation ($R^2 = 0.9623$) at 200 $\mu\text{g/mL}$ in various sizes of silica NPs.

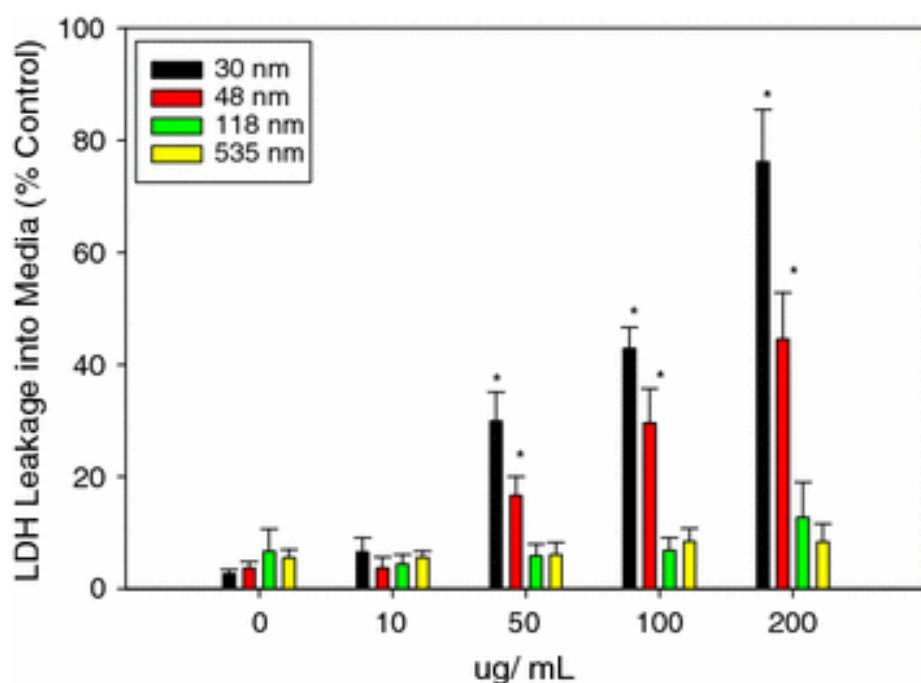


Figure 36. Effect of SiO_2 on LDH leakage into media (percent control). The HEL-30 cells were dosed with different sizes (30, 48, 118, and 535 nm) and various concentrations of silica (0, 10, 50, 100, and 200 $\mu\text{g/mL}$) for 24 hours. Size- and dose-dependent LDH leakage were observed in 30 and 48 nm silica NPs. Large size (118 and 535 nm) showed less toxicity compared with smaller NPs. Three independent experiments ($n = 3$) were carried out, and data are means \pm SD. *Significantly different from control at $p < 0.05$

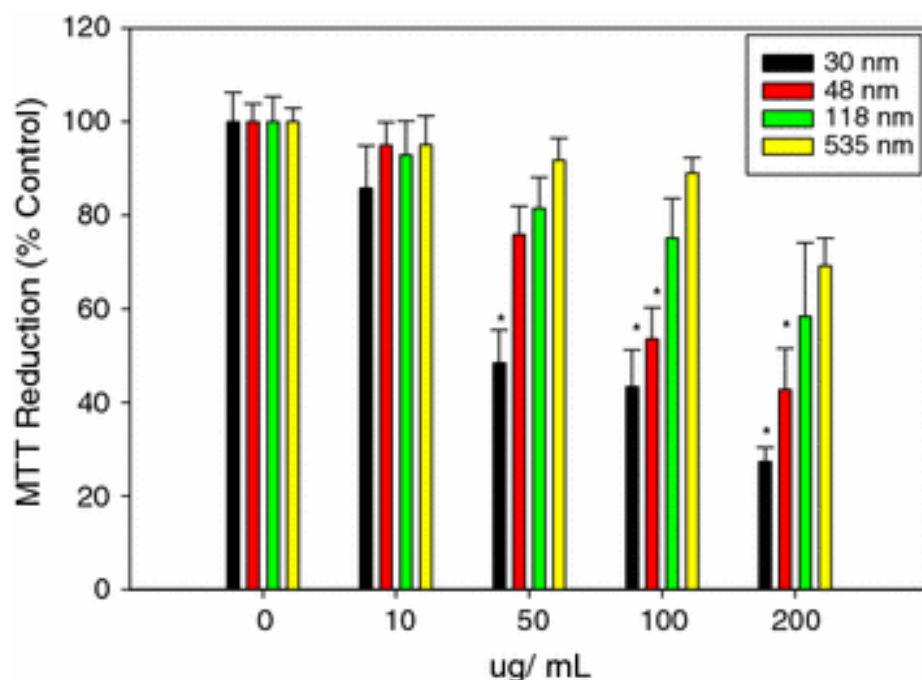


Figure 37. Effect of silica nanoparticles on MTT reduction (percent control). The HEL-30 cells were dosed with different sizes (30, 48, 118, and 535 nm) and various concentrations of silica (0, 10, 50, 100, and 200 µg/mL) for 24 h. Size- and dose-dependent MTT reduction in 30 and 48 nm at higher concentrations (200 µg/mL) produced significant toxicity when compared to large sizes (118 and 535 nm). Three independent experiments ($n = 4$) were carried out, and data are means \pm SD. * Significantly different from control at $p < 0.05$

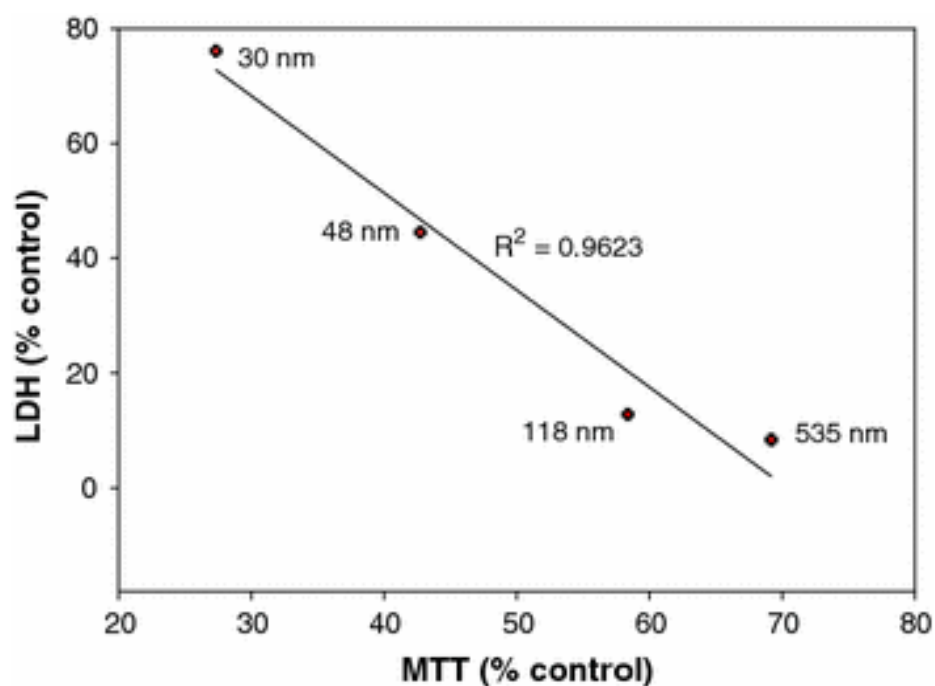


Figure 38. Correlation between LDH and MTT in various sizes of silica nanoparticles at 200 µg/mL. The graph was generated using two data points in the highest exposure condition (200 µg/mL) in Figs. 30 and 31.

Experiments were performed to study redox potential/ thiol status (Fig. 39). The smallest particles at high concentration of silica produced toxicity. Exposure to 30 nm particles showed GSH levels decreased 93, 89, and 78 percent of the control at 50, 100 and 200 $\mu\text{g/mL}$ respectively. Only at the highest concentrations (200 $\mu\text{g/mL}$) of 30 nm silica NPs the toxicity was statistically significant. With 48 nm particulate exposure, GSH levels were reduced to 100, 98 and 87 percent at 50, 100 and 200 $\mu\text{g/mL}$, respectively. No changes of GSH levels were detected at any concentration for the 118 and 535 nm NPs.

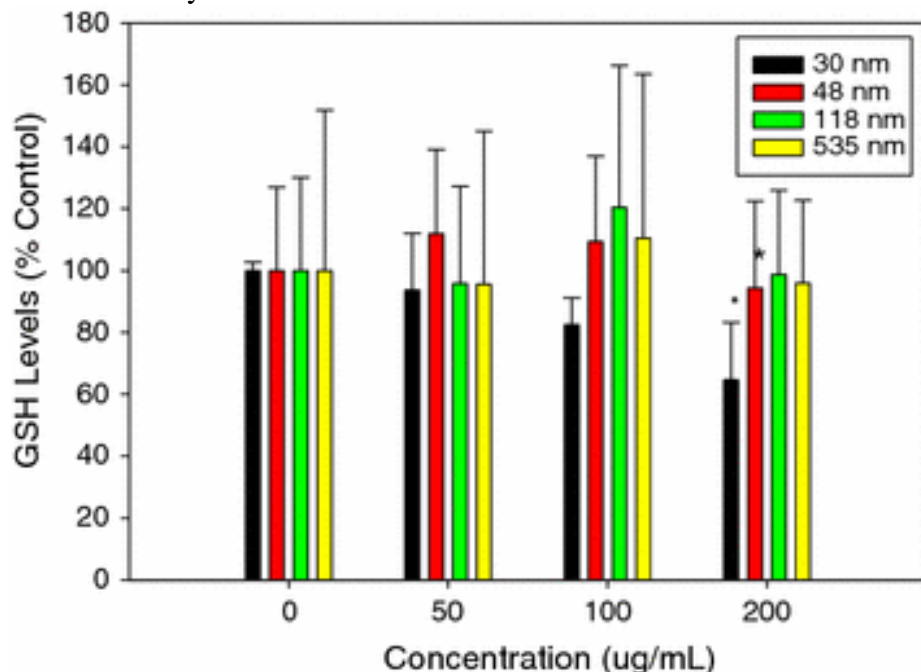


Figure 39. Effect of silica nanoparticles on GSH levels (percent control). The HEL-30 cells were dosed with different sizes (30, 48, 118, and 535 nm) and various concentrations of silica (0, 10, 50, 100, and 200 $\mu\text{g/mL}$) for 24 hours. Size- and dose-dependent toxicity was observed. Three independent experiments ($n = 4$) were carried out, and data are means \pm SD. *Significantly different from control at $p < 0.05$.

Increase in ROS levels causes damage to cell structures (oxidative stress), eventually leading to cell death or apoptosis [148]. Time course studies of silica particles (30, 48, 118 and 535 nm) at different concentrations (0, 10, 50, 100 and 200 $\mu\text{g/mL}$) were performed, and no significant increase of ROS levels was observed at any time points or at any concentrations when compared with the controls. Therefore, concentration of 10 $\mu\text{g/mL}$ of silica NPs at 6 h post dosing was chosen to represent all data (Fig. 40).

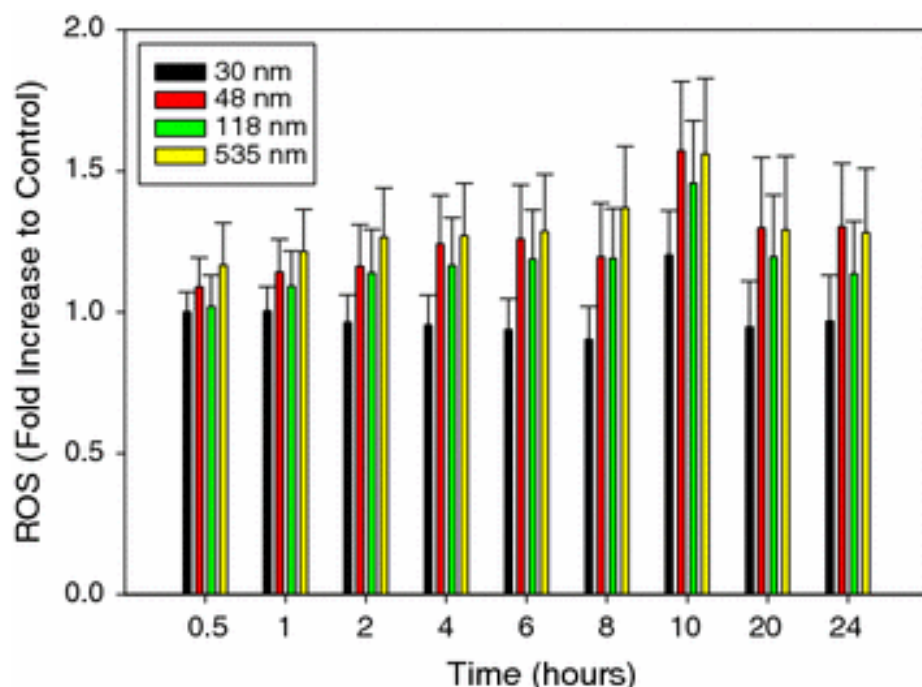


Figure 40. Time course study of effect of silica nanoparticles on ROS formation (fold of increase compared with the control). The HEL-30 cells were dosed with different sizes (30, 48, 118, and 535 nm) and various concentrations of silica (0, 10, 50, 100, and 200 $\mu\text{g/mL}$) for 0, 0.5, 1, 2, 4, 6, 8, 10, 20, and 24 h. There was no difference between the controls and dosed cells. Concentration of 10 $\mu\text{g/mL}$ was selected to represent this study. There was no difference statistically in all experiments

Unique cellular interaction of silver nanoparticles: Size dependent generation of reactive oxygen species

Silver NPs with diameters of 15, 30, and 55 nm were used to determine the size dependent effect on MACs. Mitochondrial function was assessed by the MTT reduction assay after 24 hours of NP treatment. Ag-15 nm significantly reduced mitochondrial function at concentrations starting from 5 $\mu\text{g/mL}$, Ag-30 nm at 10 $\mu\text{g/mL}$, and Ag-55 nm at 50 $\mu\text{g/mL}$ indicating a possible size-dependent cytotoxicity. The negative NP control TiO_2 did not show any statistically significant difference compared to controls for any of the sizes examined (Fig. 41). Based on LDH leakage, both Ag-15 nm and Ag-30 nm significantly decreased cell membrane integrity at concentrations from 10-75 $\mu\text{g/mL}$ whereas Ag-55 nm did not significantly reduced the integrity until 75 $\mu\text{g/mL}$ (Fig. 42). ROS production is shown to significantly increase with Ag-15 nm concentration, while Ag-30 and Ag-55 nm do not significantly induce oxidative stress (Fig. 43).

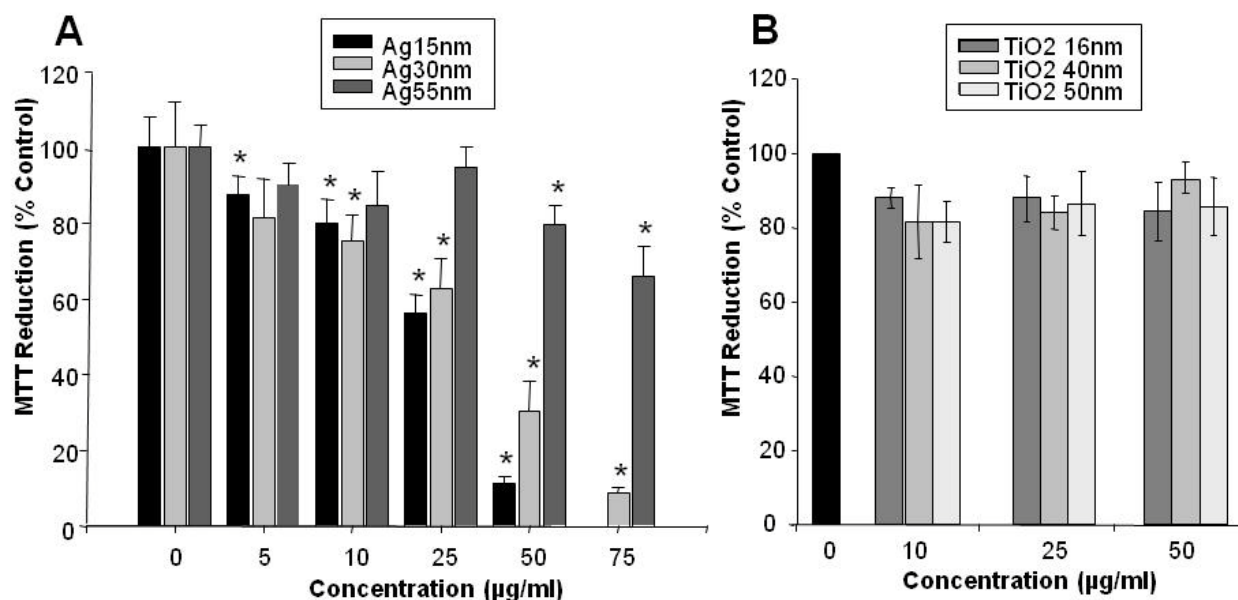


Figure 41. Effect of Ag and TiO₂ nanoparticles on mitochondrial function in macrophages. A. Ag-15 nm, Ag-30 nm, and Ag-55 nm; B. Negative NP control TiO₂.

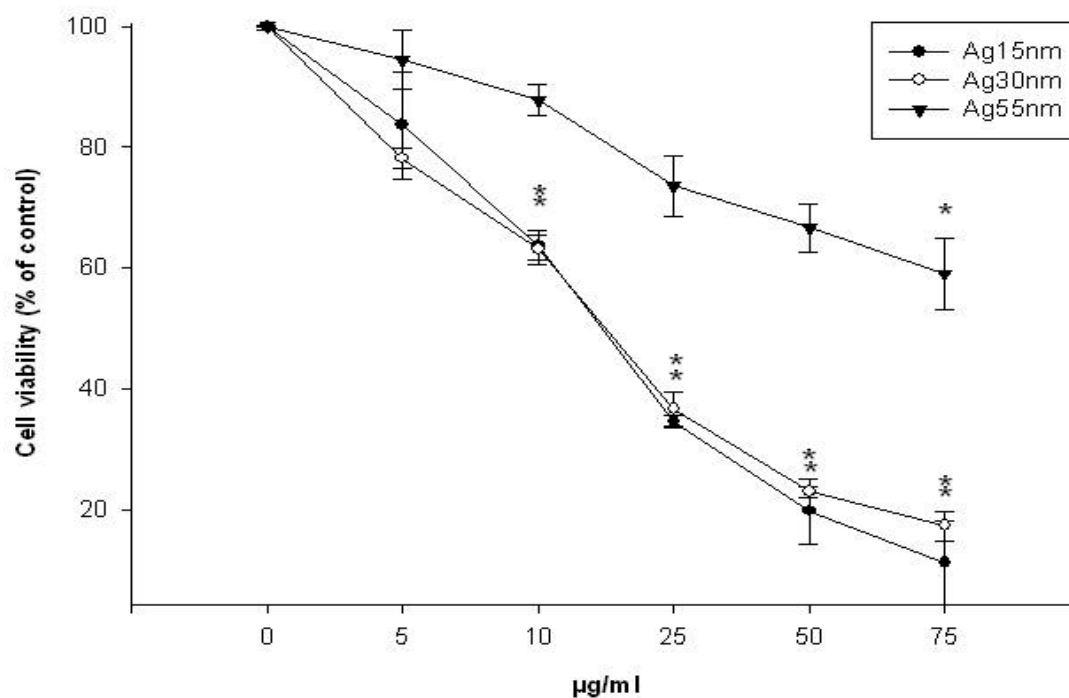


Figure 42. Effect of Ag nanoparticles on membrane integrity in macrophages. Cells were treated with various concentrations of silver NPs for 24 h. Following the treatment period, membrane integrity was assessed by measuring LDH leakage. Fluorescent values of the control cells (NPs-free exposure media) were set at 100 percent and the fluorescent values of the treated cells were measured as a percent of control. The data are expressed as a mean \pm SD of three independent experiments conducted in triplicate. (*) indicates a statistically significant difference compare to controls ($p < 0.05$).

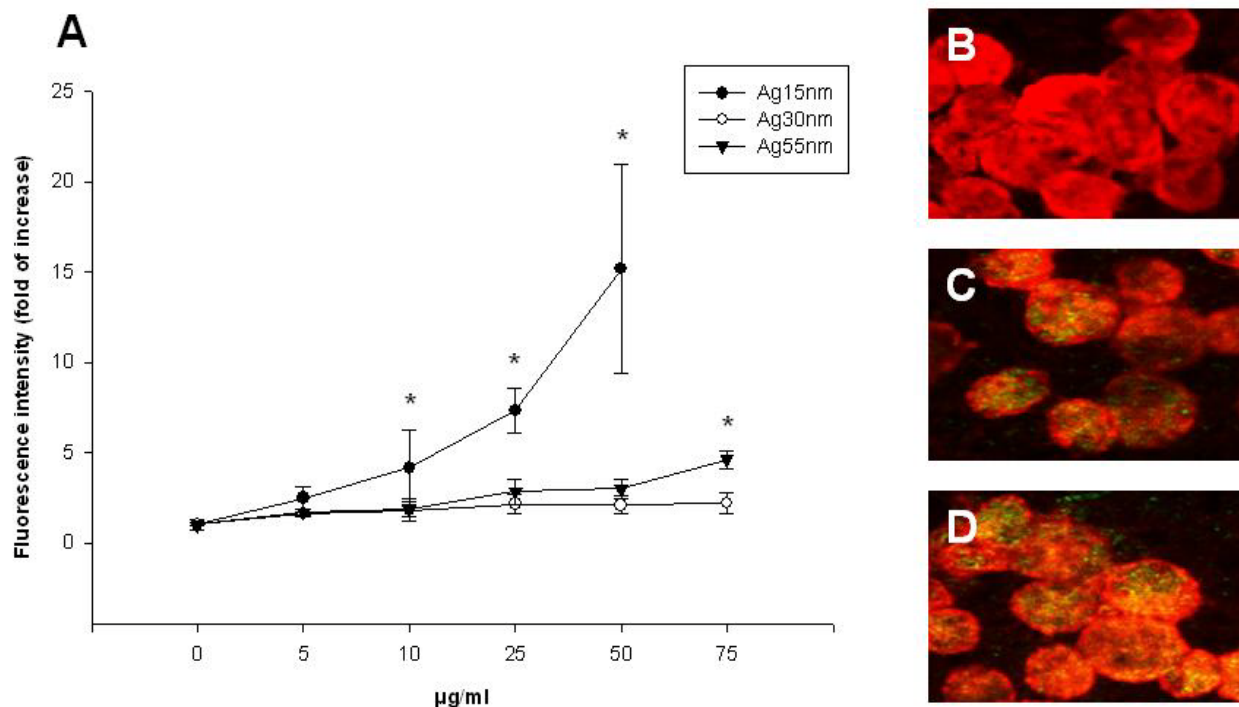


Figure 43. Effect of Ag nanoparticles on reactive oxygen species generation in macrophages. After 24 h incubation with Ag NPs, the fluorescent intensity of DCF was assessed via microplate reader (A) or fluorescence microscopy (200x) (B-D). **A.** Plot of mean data for ROS as fold increase in fluorescence \pm SD relative to control cells (NP-free media) of three independent experiments. (*) indicates a statistically significant difference compare to controls ($p < 0.05$); **B-D.** Fluorescent microscopy (200x) of cells following 24 h treatment with Ag-15 nm NPs. **B.** Control cells; **C.** Cells treated with 10 $\mu\text{g/mL}$ of Ag-15 nm; **D.** Cells treated with 25 $\mu\text{g/mL}$ of Ag-15 nm.

As described in the Materials and Methods section, the mitochondrial membrane potential was assessed in rat alveolar macrophages after exposure to silver NPs to further assess the mechanisms involved in toxicity. Loss of MMP in the MACs increased with concentration for the smaller two particles, while it was not significantly affected by exposure to Ag – 55 nm (Fig. 44). Using the microscopy method, all three particles appear to disrupt the MMP (Fig. 45).

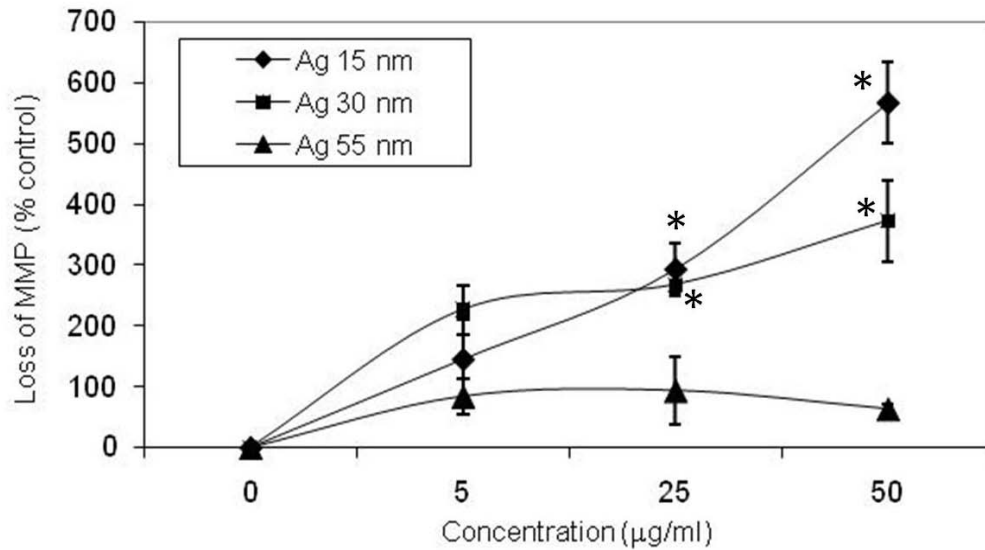


Figure 44. Assessment of mitochondrial membrane potential in macrophages. Fluorescent intensity data expressed as percent of control as means \pm SD of three independent experiments. (*) indicates a statistically significant difference compared to time-matched controls ($p < 0.05$).

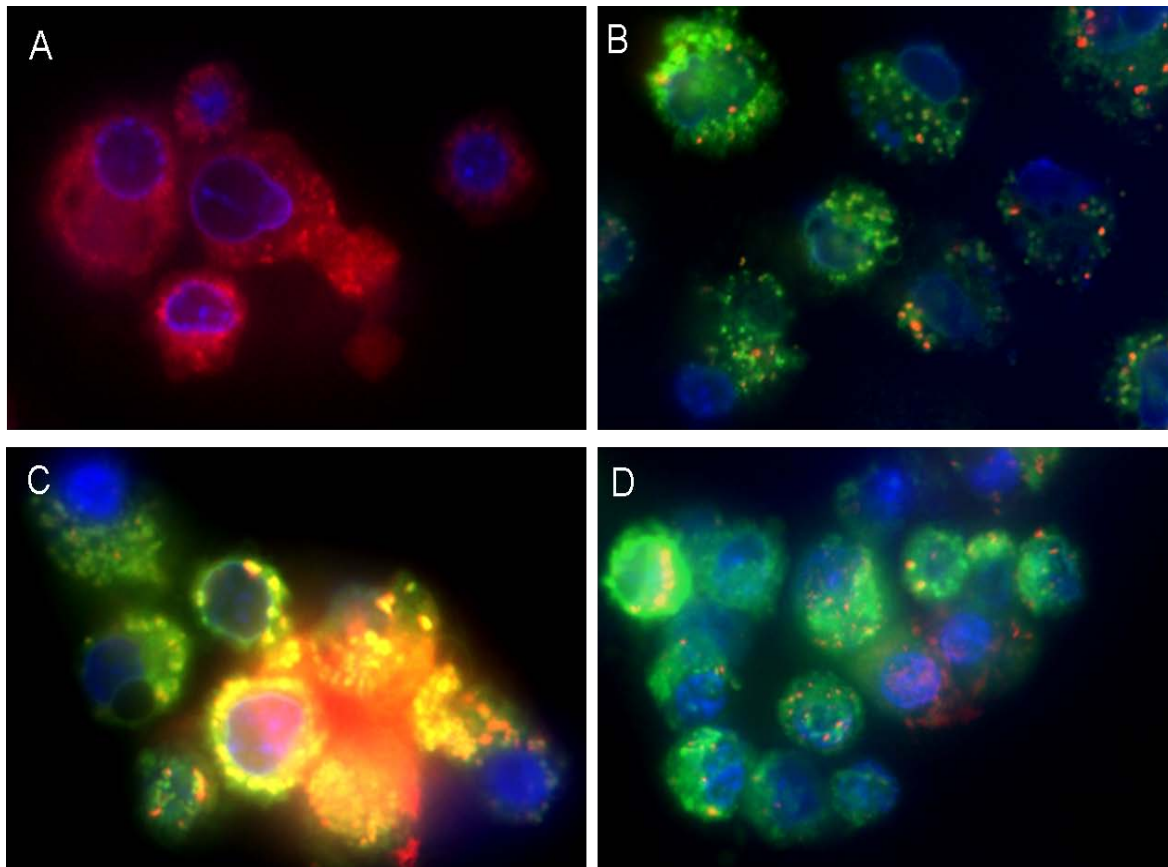


Figure 45. Qualitative assessment of macrophages exposed to silver to distinguish normal cells versus apoptotic cells by confocal microscopy. A. Control macrophages; B. Macrophages treated with 5 $\mu\text{g/mL}$ Ag 15 nm; C. Macrophages treated with 5 $\mu\text{g/mL}$ Ag 30 nm; D. Macrophages treated with 5 $\mu\text{g/mL}$ Ag 55 nm.

Silver nanoparticles disrupt GDNF signaling in spermatogonial stem cells independent of nanoparticle size and coating

To evaluate the changes in the physicochemical properties of the silver NPs, they were characterized prior to, during, and post-exposure. The TEM analysis verified the primary NP size and morphology (Fig. 46A-D) and showed similarities in spherical morphologies. The Ag 15-HC, Ag 10-PS, and Ag 25-PS all had mean sizes very close to the manufacturer specified sizes, while the Ag 25-HC and Ag 80-PS samples were slightly off the specified sizes (Fig. 46E and 47). Furthermore, the NP coating could be verified using the TEM analysis and the average NP coating was shown to be between 1-3 nm (Fig. 47). In addition, DLS was previously described and demonstrated that all of the silver NPs aggregated to some extent after being dispersed in water (Fig. 46F) [92]. Furthermore, the total carbon content, measured by XPS showed that for the polysaccharide synthesized samples was higher than the carbon content seen with the HC NPs (respectively 35-68 atomic percent C and C-H) (Fig. 46F). The Ag 25-PS had the thickest coating around 3 nm when viewed in the TEM and this corresponded to the XPS data which showed a higher C=O content. The Ag 25-HC TEM measurements did not show a significant change in primary particle size from pre-exposure to post-exposure conditions; however, a slight decrease in primary particle size is observed when measured intracellularly (Fig. 46E). DLS measurements showed that agglomerate sizes only decreased slightly between pre-exposure and post-exposure conditions (Fig. 46D). XPS analysis of Ag 25-HC pre-and post-exposure showed no significant changes in composition, which is verified by the TEM results (Fig. 46F).

Attempts to further characterize the NPs after uptake in the cells themselves was difficult due to the need for strong abrasive chemicals to remove the cellular debris which could have in turn impacted the NPs themselves, which is why the artificial fluid was chosen. Initially, the hypothesis was that the stability of the coating was impacting the change in the biological response and the post-exposure characterization analysis supports this hypothesis. While the Ag 10 nm-PS primary particle size decreases nearly 50 percent from pre-to post-exposure conditions, the intracellular primary particle sizes were observed to increase almost 3 fold (Fig. 46D). DLS results show a significant increase in agglomeration post-exposure at 4 fold the pre-exposure sizes (Fig. 46D). XPS results indicate a considerable decrease of C-H bonds from pre-to post-exposure along with an increase in the percentage of Ag, indicating a decrease in coating coverage of the surface of the particle (Fig. 46E). Also, the sulfur present was determined to be from a previously unknown dispersant aide, DAXAD, which was not present in the post-exposure results (Fig. 46E). The XPS data, along with the TEM and DLS data, leads to the conclusion that the coating was degraded, which in turn has caused the surface of the NP to be exposed to the lysosomal solution. After a period of time, the particle appears to be losing size due to the loss of the coating and the Ag ions dissociating into solution. This data strongly suggests the need to characterize nanomaterials at each step in the experimental process and demonstrates that the cellular environment has a major effect on the NP stability. Furthermore, the growth curve data supports previous studies which illustrated that silver NPs are more reactive in a size dependent fashion and illustrates that over time NP coatings can be degraded and biocompatibility can be lost.

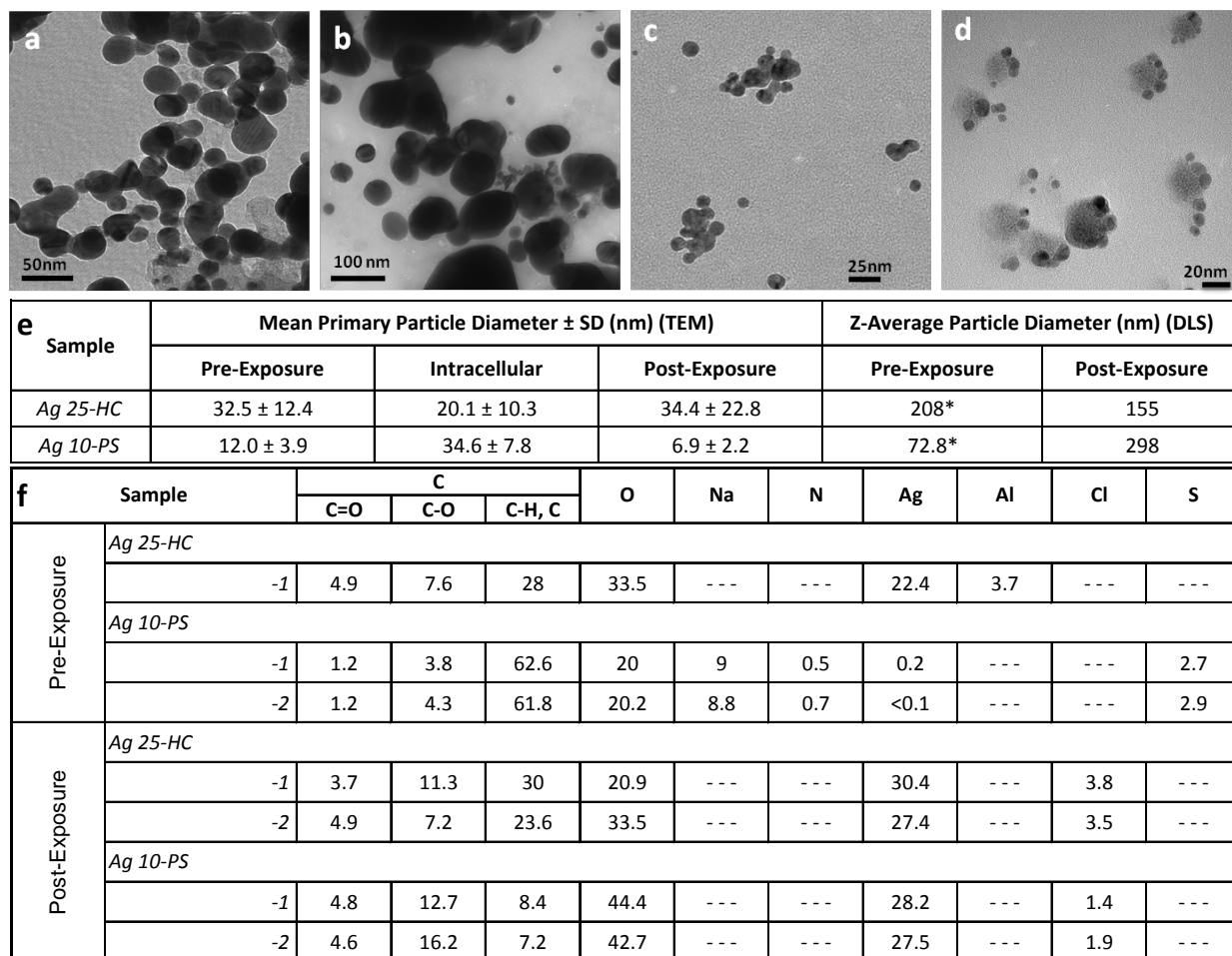
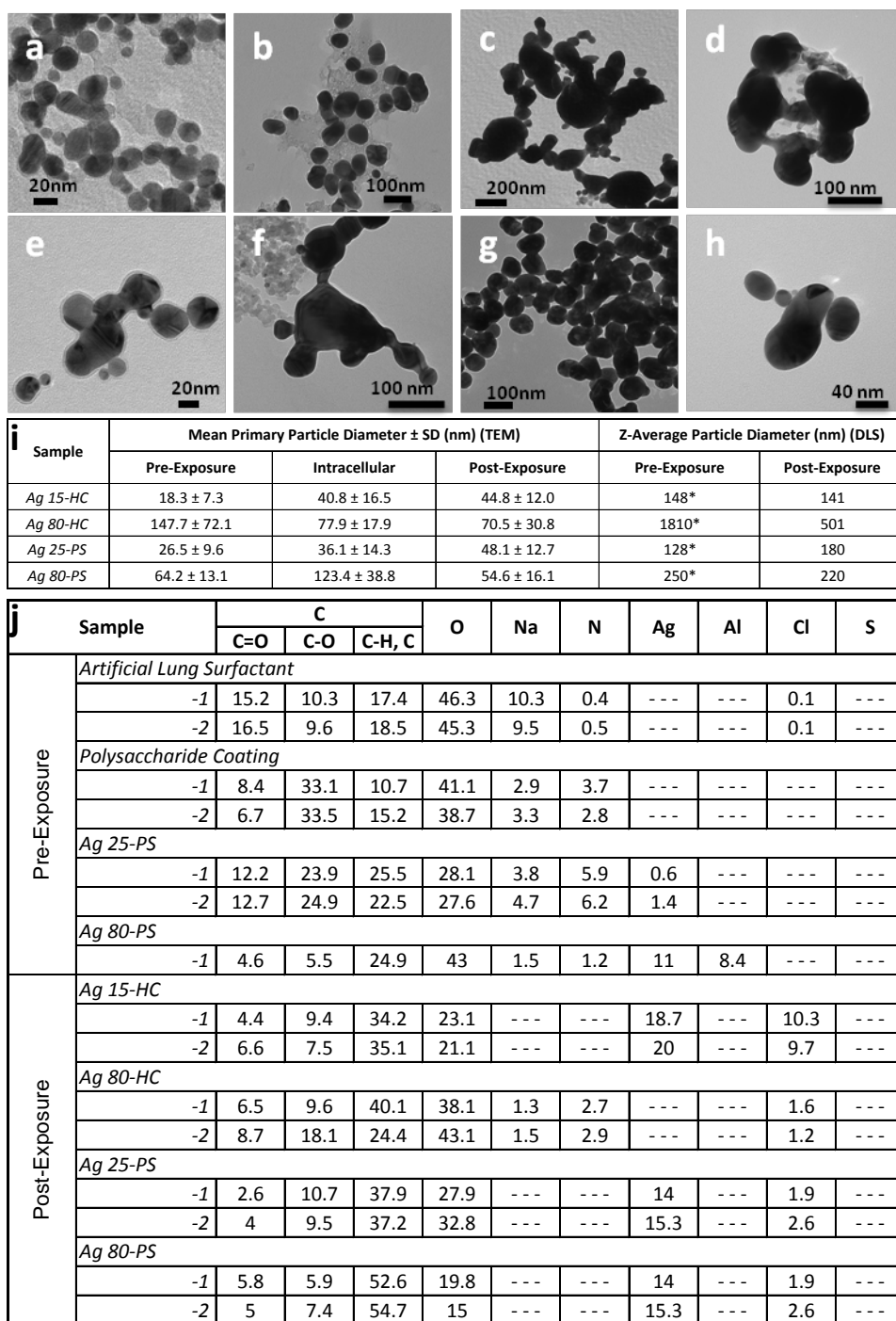


Figure 46. Characterization data for the Ag 25-HC and Ag 10-PS. TEM of NPs showing pre- and post-exposure morphologies. **A.** Ag 25 nm-HC pre-exposure; **B.** Ag 25 nm-HC post-exposure (72 h in lysosomal fluid); **C.** Ag 10 nm-PS pre-exposure; **D.** Ag 10 nm-PS post-exposure (72 h in lysosomal fluid); **E.** Comparison of TEM size distributions and DLS measurements at pre-exposure, intracellular (TEM only), and post-exposure conditions (previously reported in Murdock *et al.*, 2008 [63]); **F.** Comparison table of XPS data for Ag 25 nm-HC and Ag 10 nm-PS shown as approximate atomic percent elemental surface composition.

By examining the data obtained from the different techniques (XPS, TEM and DLS), it appears the coating on the Ag 10-PS particles has degraded, allowing the surface of the NP to be exposed to the lysosomal solution. After 72 hours, the mean primary particle size is decreased due to Ag dissociating into solution (Ag^+).

The Ag 15 nm-HC TEM measurements indicate that primary particle size increases from pre-exposure, to intracellular, to post-exposure (Fig. 47I). DLS measurements indicate that agglomerate sizes remain nearly the same from pre-exposure conditions to post-exposure conditions (Fig. 47I). Post-exposure XPS of Ag 15 nm-HC did not exhibit any abnormal measurements (Fig. 47I). A significant decrease in primary particle size was observed with the Ag 80 nm-HC via TEM, nearly a 50 percent decrease, from pre-exposure to intracellular and post-exposure conditions (Fig. 47I). Also, a significant decrease in agglomeration was observed by DLS post-exposure, greater than 70 percent, when compared to pre-exposure conditions (Fig.

47I). Post-exposure XPS revealed that no Ag was detected which indicates that the particles had mostly dissociated into ionic Ag (Fig. 47J). A slight increasing primary size trend was observed with the Ag 25 nm-PS from pre-exposure, to intracellular, to post-exposure conditions (Fig. 47I). DLS measurements of agglomeration sizes of the particles in solution only exhibited a slight increase from pre-exposure to post-exposure conditions (Fig. 47I). Significant decreases in the percentages of C=O and C-O were found from pre- to post-exposure conditions from the XPS measurements; however, a slight increase in C-H percentages was observed as well as no change in the percentage of O (Fig. 47J). For the Ag 80 nm-PS, primary particle size decreased slightly from pre-exposure to post-exposure; however, the intracellular primary size was increased 2 fold from the pre-exposure size (Fig. 47I). DLS results indicated a slight decrease in agglomeration from pre- to post-exposure conditions (Fig. 47I). XPS measurements revealed an increase of the percentage of C-H from pre-exposure to post-exposure conditions; however, the percentage of O decreased by 50 percent (Fig. 47J).



The size distribution of the Ag NPs was obtained through imaging on TEM and particle sizing using software. At least 300 NPs were measured via the software for each sample of Ag. Size distributions were acquired by inputting the 300 or more data points into SigmaPlot 10.0 and performing a histogram plot with automatic 'binning.' This gave a representative distribution of the Ag samples. Next, calculations were performed to give estimates of the number of NPs per sample, total surface area per sample, and total volume per sample based off the particle distributions. This yielded a fairly accurate estimate of the content and characteristics of each sample, which can be seen in Table 10. As far as the issue of concentration, weight/volume vs. number of particles/volume, this is a topic which has been discussed numerous times. To give an idea of how difficult it is to dose with a specific number of particles, take the samples from this experiment as an example. In Table 10, the mass of the samples were kept constant at 10 μg (from 10 $\mu\text{g/mL}$ concentration) and all other factors were calculated from the distribution of sizes found for each sample from the TEM. At least 300 particles were counted and measured to give a reasonably accurate distribution (Table 10). Particles were assumed to be approximately spherical in shape (which is verified with TEM pictures) and the density was assumed to be similar to bulk Ag (10490 kg/m^3). As can be seen in Table 10A, the number of particles per sample varies widely; however, the total surface area of the particles in the sample decreases with increasing particle size. Volume is constant across all samples since mass was kept constant. Now, if we compare the information in Table 10A to the information in Table 10B, where the numbers of particles in each sample were kept constant at 1×10^{12} , we can observe some of the issues which have been continuously argued about which parameter to keep constant. In this case, with a constant number of particles for each sample, the mass of each sample increases drastically with increasing average particle size. The total surface area and total volume taken up by the particles in each sample also increases with increasing particle size. If one parameter is picked to be constant, others will vary to compensate. To dose an *in vitro* experiment with a concentration of 52.3 $\mu\text{g/mL}$ for Ag 15-HC, for example, and compare the effect on viability with one dosed with 281.7 $\mu\text{g/mL}$ of Ag 25-HC and 32.2 mg/mL of Ag 80 nm, is not reasonable. It yields approximately the same number of particles per sample; however, considering the other variations in mass, surface area, and volume this does not provide a reasonable means of practical comparison between the samples. The turbidity of the Ag 80-HC sample would be extremely high, if not almost sludge-like, and could very well be simply smothering the cells causing reduced viability to be observed.

The only reasonable means of testing samples with equal number of particles is to have an extremely small sample size, such as 1,000 to 10,000 particles, which would limit the differences in the other physical parameters. However, at this time, no such dosing technique is known where NPs can be counted individually or such extremely small amounts of material can be weighed, handled, and distributed accurately. This leads back to previous discussions such as to which parameter one should keep constant to assess toxicity. Suggestions have been made that total surface area must be the standard for toxicity studies. Once again, the problem becomes variation in the other parameters when one is held constant. Possibly, the best scenario is to test all possibilities within one study and attempt to draw conclusions among the different exposure methods (i.e. constant number of particles, constant mass/volume, and constant surface area). However, this leads to extremely time consuming and lengthy experiments and higher costs for both toxicity supplies and nanomaterial supplies. Therefore, the most effective and capable means of exposure currently, to assess biological interactions and compare among different samples (of the same material), is by weight of the sample.

Table 10. Nanoparticle Parameters Used to Determine Dosing Metric.

a. Size distribution of the silver NPs with calculations of NP parameters with constant mass of 10 μg . **b.** Size distribution of the silver NPs with calculations of NP parameters with constant number of NPs (1×10^{12}).

a. Constant Mass (10 μg)

Sample	Estimate of Total Number of Nanoparticles	Estimate of Total Surface Area (nm^2)	Estimate of Total Volume (nm^3)
<i>Ag 15-HC</i>	7.8E+11	3.6E+14	9.5E+14
<i>Ag 25-HC</i>	1.6E+11	2.1E+14	9.5E+14
<i>Ag 80-HC</i>	3.0E+09	5.0E+13	9.5E+14
<i>Ag 10-PS</i>	1.8E+12	5.2E+14	9.5E+14
<i>Ag 25-PS</i>	2.5E+11	2.5E+14	9.5E+14
<i>Ag 80-PS</i>	9.2E+09	9.3E+13	9.5E+14

b.**Constant Number of Particles (1×10^{12})**

Sample	Estimate of Mass (mg) / 1mL	Estimate of Total Surface Area (nm^2)	Estimate of Total Volume (nm^3)
<i>Ag 15-HC</i>	0.05	1.2E+15	5.0E+15
<i>Ag 25-HC</i>	0.28	3.8E+15	2.7E+16
<i>Ag 80-HC</i>	32.23	8.5E+16	3.1E+18
<i>Ag 10-PS</i>	0.01	5.1E+14	1.3E+15
<i>Ag 25-PS</i>	0.15	2.5E+15	1.4E+16
<i>Ag 80-PS</i>	1.65	1.4E+16	1.6E+17

To demonstrate surface binding of NPs on the cells, the C18-4 cells were incubated for 24 hours with 10 $\mu\text{g/mL}$ HC- or PS-coated silver NPs, then processed for SEM (Fig. 48A-48I) or TEM (48J-48O).

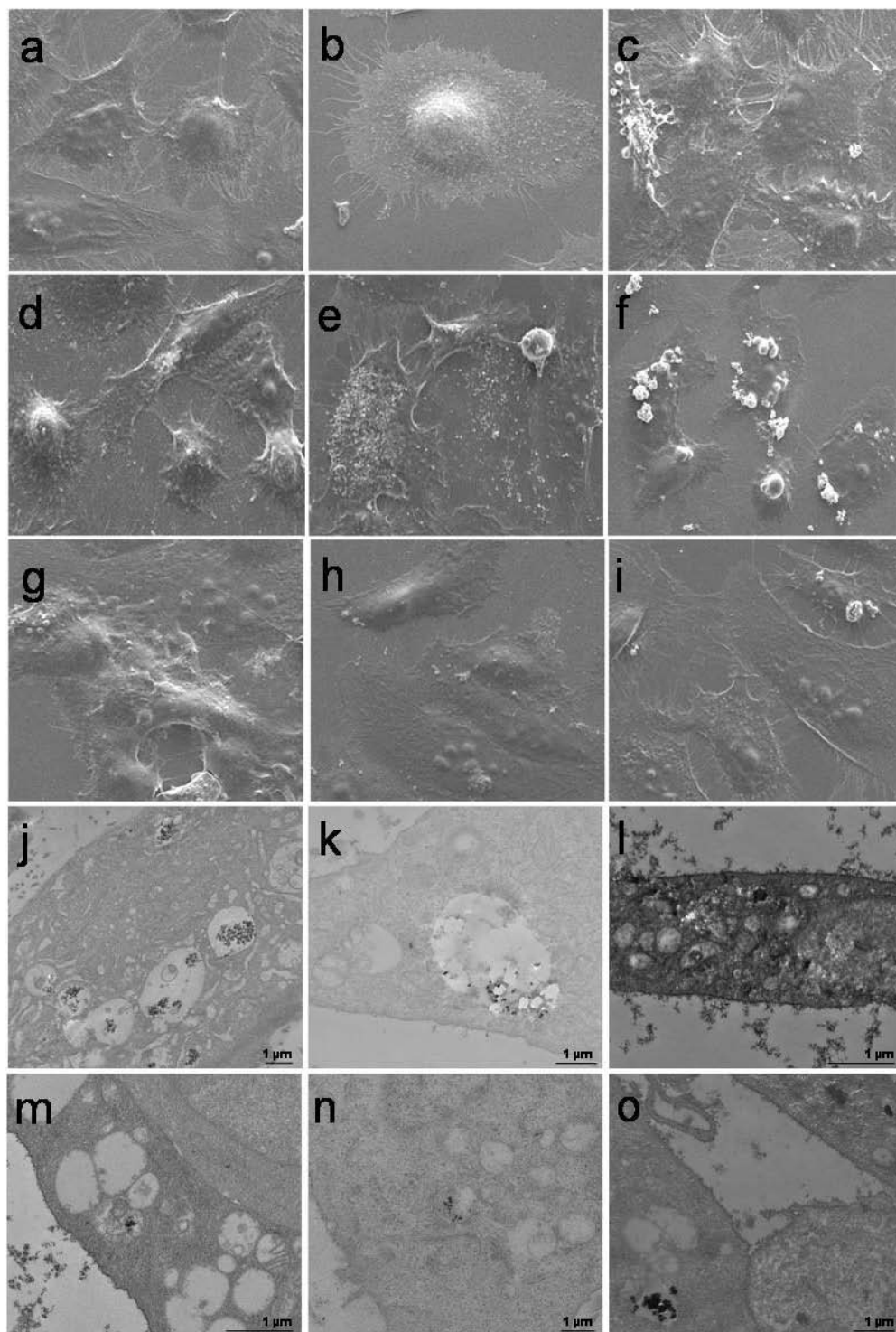


Figure 48. Demonstration of surface binding, internalization, and localization of Ag nanoparticles by germ-line stem cells. A. Control; B. Polysaccharide; C. Ag 130; D, J. Ag 15-HC; E, K. Ag 25-HC; F, L. Ag 80-HC; G, M. Ag 10-PS; H, N. Ag 25-PS; I, O. Ag 80-PS. White arrows denote agglomerates of Ag NPs on the cell surface and black arrows denote internalization into intracellular vacuoles. Original SEM images were taken at 1300x magnification and scale bars for TEM images are 1 micron.

The cell viability of C18-4 cells after six days of continuous exposure to silver NPs and daily treatment with GDNF was assessed based on mitochondrial function (Fig. 49A). GDNF was able to significantly promote cell growth when the NPs were not present, but the addition of silver NPs (regardless of size or coating) inhibited this effect. A growth curve of C18-4 cells continuously exposed to Ag 15-HC and Ag 10-PS silver NPs and treated daily with GDNF was also generated (Fig. 49B). The Ag 10-PS NPs were initially more biocompatible, but over time this is lost and there is no difference in growth between the two treatments. Furthermore, GDNF is unable to significantly promote proliferation when compared to the controls. The model of GDNF-induced proliferation in C18-4 cells is presented in figure 49C. The key mediators of this signaling pathway are identified. Potential targets for disruption of GDNF signaling in C18-4 cells that inhibit proliferation are shown in Figure 49D.

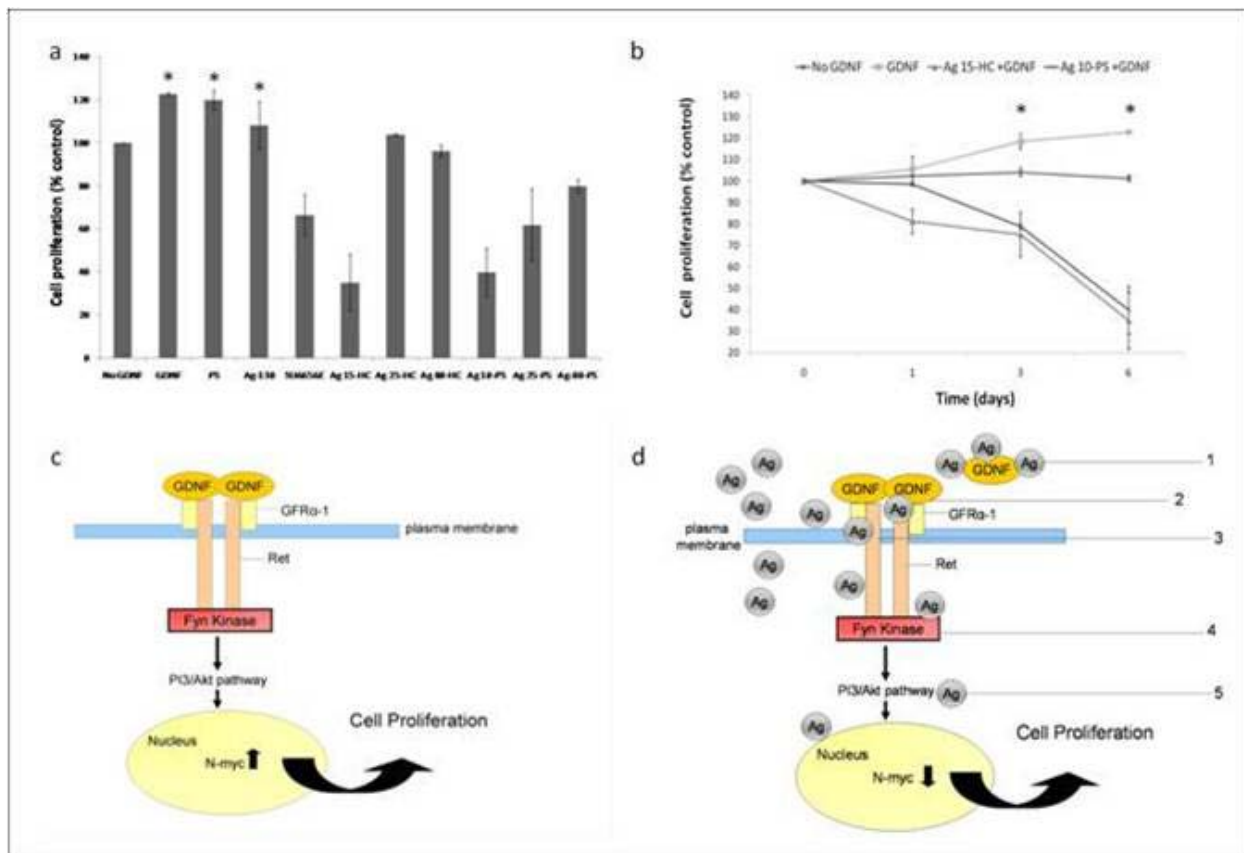


Figure 49. Proliferation of C18-4 cells treated with coated silver nanoparticles. **A.** Viability of C18-4 cells after six days of continuous exposure to silver NPs and daily treatment with GDNF (asterisk $P < 0.05$); **B.** Growth curve of C18-4 cells continuously exposed to Ag 15-HC and Ag 10-PS silver NPs and treated daily with GDNF (asterisk $P < 0.05$); **C.** Model of GDNF-induced proliferation in C18-4 cells, identifying key mediators of this signaling pathway; **D.** Potential targets for disruption of GDNF signaling in C18-4 cells that inhibit proliferation. 1) NPs bind to GDNF and preventing receptor binding, 2) NPs bind to receptors and prevent GDNF from binding, 3) NPs interact with the RET receptor and prevent activation of the receptor and downstream elements, 4) NPs bind to Fyn kinase and prevent activation of Fyn and downstream elements, and 5) NPs interact with proteins in the PI3/Akt pathway.

The amount of extracellular GDNF was assessed (Fig. 50). The presence of silver NPs did not alter the levels of free GDNF in the tissue culture media, indicating that the NPs were not binding to the growth factor, preventing it from binding the receptors (Fig. 50A). When C18-4 cells were treated with silver NPs regardless of size or coating, GDNF was able to activate the receptors (Fig. 50B).

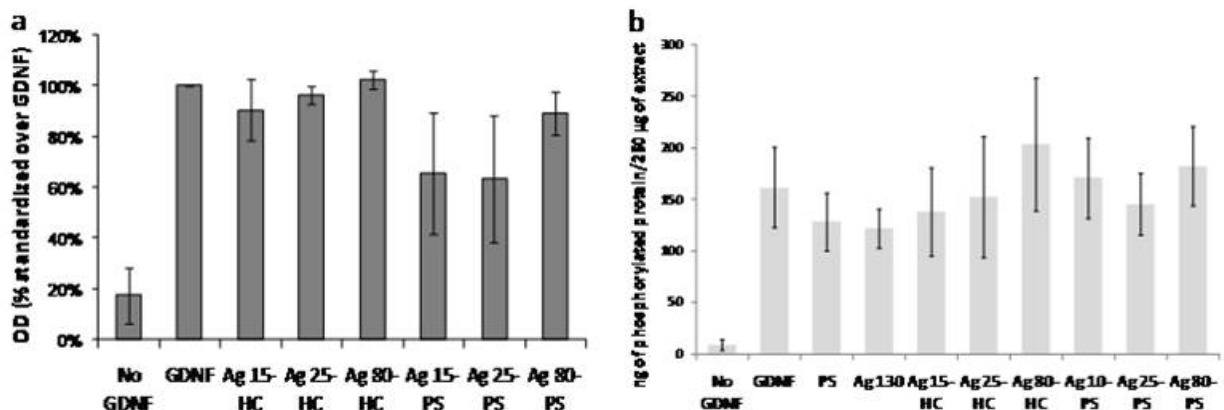


Figure 50. Effect of silver nanoparticles on the extracellular components of the GDNF signaling pathway. A. Extracellular GDNF in the presence of silver NPs; **B.** When C18-4 cells were treated with silver NPs regardless of size or coating, GDNF was able to activate the receptors.

Fyn kinase phosphorylation and activation was tested in the presence of coated silver NPs (Fig. 51). GDNF significantly increased Fyn phosphorylation in comparison with the control sample without GDNF ($P < 0.05$), while GDNF-induced phosphorylation was inhibited by the silver NPs. The purified Fyn kinase showed a significant size-dependent decrease of activity (asterisk: $P < 0.05$). Interestingly, the Ag-PS NPs inhibited the kinase activity more than the Ag-HC NPs, indicating that NP coatings have an effect on protein activity. A significant decline in Fyn kinase activity in C18-4 cells was observed in presence of the NPs (asterisk: $P < 0.05$). However, this decline was not size- or coating-dependent as seen in the *in vitro* assays. The mechanism of GDNF disruption by silver NPs is shown in Figure 52.

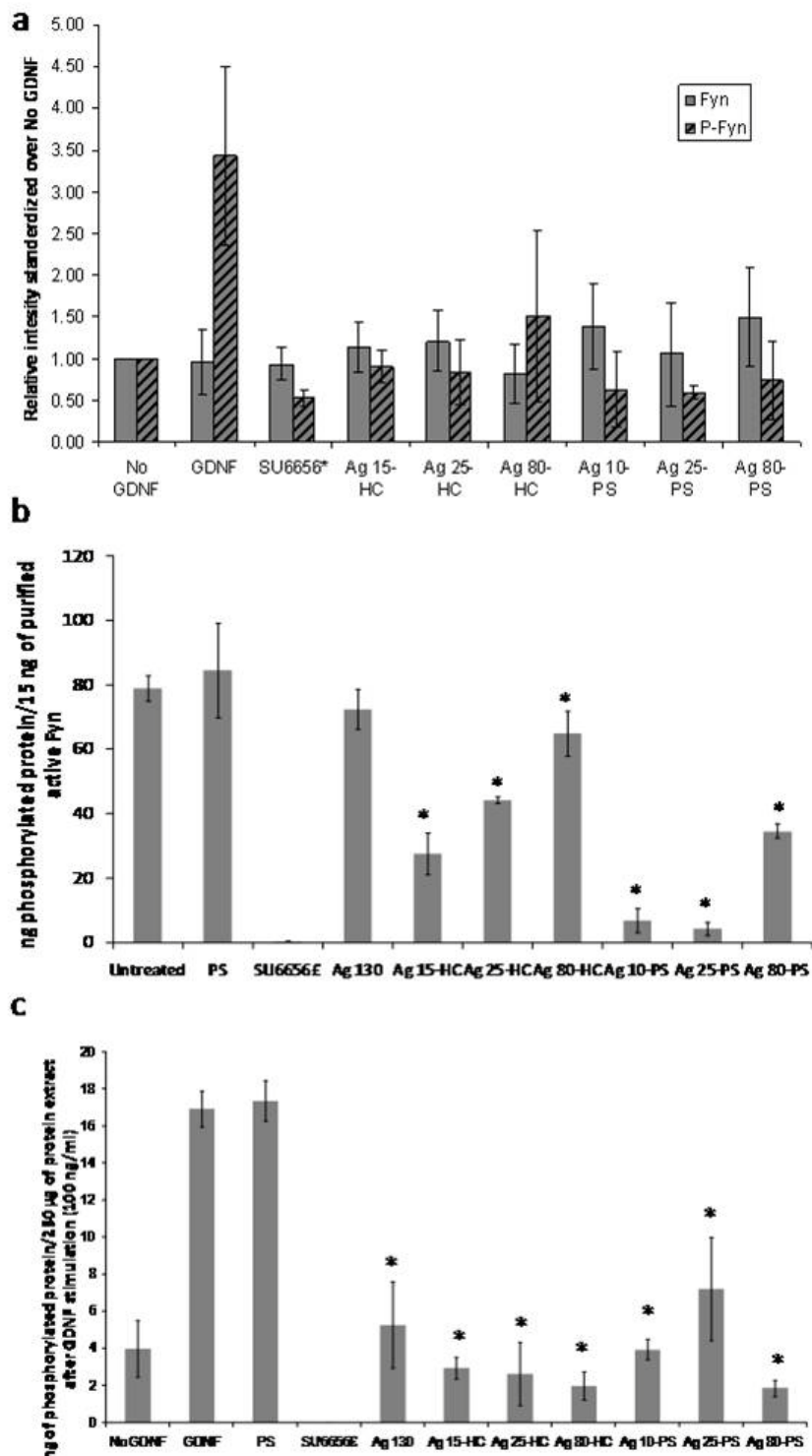


Figure 51. Fyn kinase phosphorylation and activation in the presence of coated silver nanoparticles. **A.** Effect of GDNF and GDNF + silver NPs on Fyn phosphorylation in comparison with the control sample without GDNF ($P<0.05$); **B.** The purified Fyn kinase showed a significant size-dependent decrease of activity (asterisk: $P<0.05$); **C.** A significant decline in Fyn kinase activity in C18-4 cells was observed in presence of the NPs (asterisk: $P<0.05$).

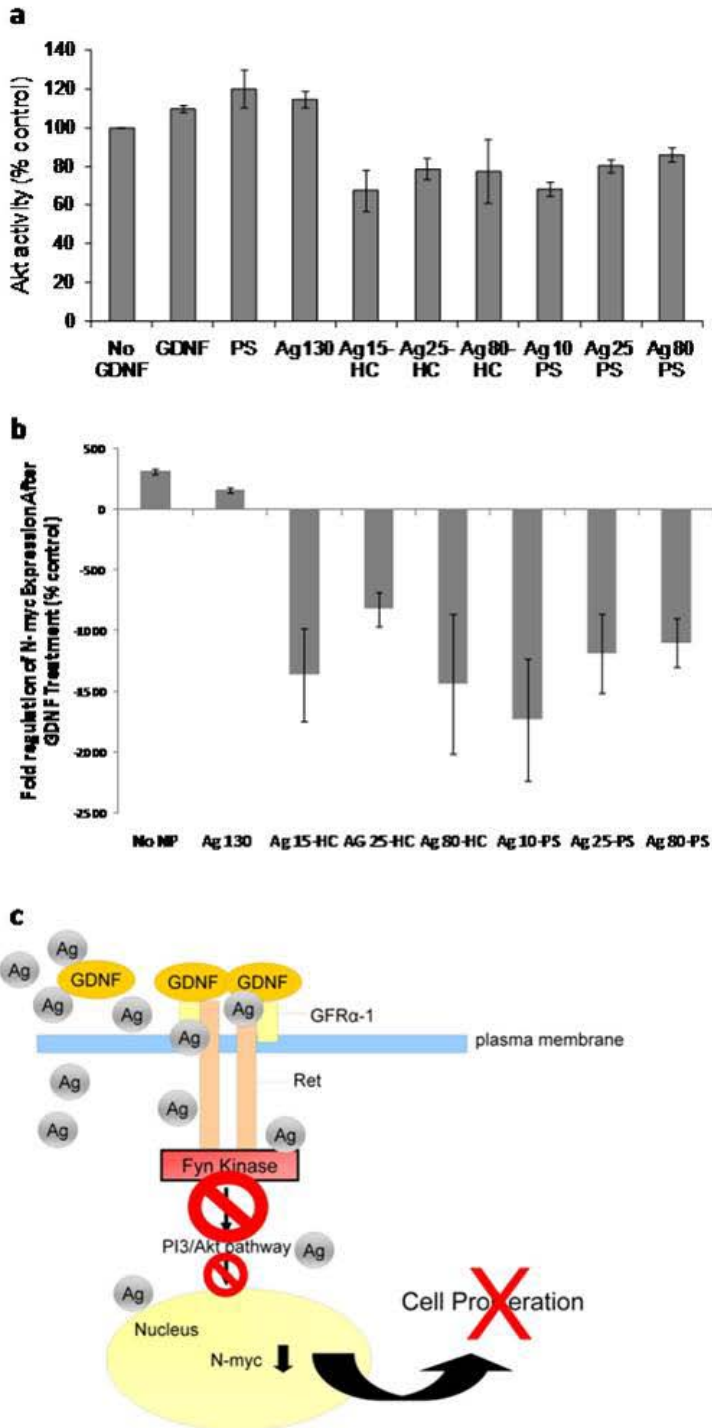


Figure 52. Mechanism of GDNF disruption by silver nanoparticles in C18-4 cells. **A.** Akt activity significantly declined in C18-4 cells treated with silver NPs and this effect was independent of size and coating (asterisk: $P < 0.05$); **B.** A significant decline in *N-myc* expression was demonstrated for C18-4 cells treated with silver NPs, similar to the Akt activity (**A**), and this effect occurred independent of NP size and coating; **C.** Model of C18-4 cell growth disruption by silver NPs. The silver NPs promoted a decrease in Fyn activity, which disrupted Akt activity and promoted a decline in *N-myc* expression, which led to a decline in cell proliferation.

Characterization and biocompatibility of “green” synthesized silver nanoparticles

The primary particle diameter of the Ag NPs produced by reducing AgNO₃ with epinephrine of varying concentrations ranged from 11 nm to 26 nm and depended upon the ratio of water and epinephrine in the solution. However, similar sizes of the particles were observed for the 1:1 (parts water to parts epinephrine) and the 10:3 ratios, which both produced particles of approximately 12 nm, as well as the 2:1 and the 20:1 ratios, which produced particles of approximately 25 nm see Table 11. DLS analysis of the epinephrine synthesized NPs was performed to examine the agglomerate size of the NPs in HEM, MEM, and Millipore water. For the epinephrine silver NPs dispersed in HEM, the agglomerate size varied greatly. For the 1:1, 2:1, and 10:3 ratios, the extent of agglomeration was measured at 65, 53, and 33 microns, respectively, and for the ratios of 10:1 and 20:1, the agglomerated sizes were measured at 1270 nm and 1320 nm. While dispersed in HEM, the epinephrine silver NP agglomerate size generally decreased with decreasing concentration of epinephrine. For the samples dispersed in MEM, the agglomerate size again varied greatly with a maximum at 29 microns (10:3 ratio) and a minimum at 248 nm (10:1 ratio), with no discernable trend based on concentration of epinephrine. In general, for the silver NPs dispersed in Millipore water, the agglomerate size was fairly constant, ranging from 30.5 microns to 48 microns, except for the 10:1 ratio which had an agglomerate size of 4640 nm. An interesting note is that the ratio of 10 parts water to 1 part epinephrine produced the third largest primary particle size, but consistently produced the smallest agglomerate size in all dispersants examined. Overall, the least agglomeration of the epinephrine synthesized silver NPs occurred while dispersed in MEM (summarized in Table 11).

TEM analysis of the silver NPs that used tea extract particles revealed primarily spherical NPs that were poly-dispersed, with most samples having two primary particle sizes (Table 11). For the 1:1 (parts water to parts tea extract) ratio, the larger primary particle size was measured to be 91.3 ± 20.9 nm, with a smaller primary particle size of 6.7 ± 2.9 nm. For the 2:1 ratio, a large primary particle size of 59.0 ± 19.7 nm was measured, with a smaller primary particle size of 9.2 ± 1.9 nm also present. For the 10:3 ratio, a larger size was measured at 71.1 ± 22.3 nm, with a smaller size at 6.1 ± 2.4 nm. The ratio of 10:1 was the only tea extract synthesized sample found to be mono-dispersed with a primary particle size of 49.8 ± 14.7 nm. Lastly the 20:1 ratio sample was measured to have a larger primary particle size of 25.9 ± 6.8 nm, with a smaller primary particle size of 3.8 ± 0.88 nm. In general, the primary particle size decreased when the concentration of tea extract in the solution was decreased. DLS analysis of the tea extract synthesized silver NPs was performed in HEM, MEM, and Millipore water. While dispersed in HEM, the agglomerate sizes ranged from 805 nm (1:1 ratio) to 1.81 microns (20:1 ratio). Unlike the epinephrine synthesized particles, the agglomerate size generally increased with decreasing concentration of tea extract when dispersed in HEM. When dispersed in MEM, the agglomerate size ranged from 291 nm (20:1 ratio) to 1.01 microns, with no distinguishable trend between the concentration of the tea extract and the agglomerate size. When dispersed in Millipore water, the agglomerate size ranged from 220 nm (20:1 ratio) to 661 nm (10:3 ratio). The agglomerate size increased with decreasing concentration of tea extract until the 10:3 ratio, and then decreased with decreasing tea extract concentration. In general, the tea extract synthesized particles had the least aggregation when dispersed in Millipore water.

Table 11. “Green” Synthesized Nanoparticles with Their Average Sizes as Powders and in Different Dispersants.

	Sample	TEM Particle Size (nm)	DLS Agglomerate Size (nm)		
			HEM	MEM	Water
Epinephrine	9% AgNO ₃ in 1:1	11.5 ± 4.7	6.51E+04	2980	3.05E+04
	12% AgNO ₃ in 2:1	25.8 ± 15.8	5.30E+04	7650	4.78E+04
	13% AgNO ₃ in 10:3	11.9 ± 3.9	3.29E+04	2.85E+04	4.48E+04
	15% AgNO ₃ in 10:1	17.3 ± 7.0	1270	248	4640
	16% AgNO ₃ in 20:1	24.2 ± 6.5	1320	2500	3.30E+04
Tea extract	9% AgNO ₃ in 1:1	A. 91.3 ± 20.9 B. 6.7 ± 2.9	805	497	510
	12% AgNO ₃ in 2:1	A. 59.0 ± 19.7 B. 9.2 ± 1.9	1370	1010	611
	13% AgNO ₃ in 10:3	A. 71.1 ± 22.3 B. 6.1 ± 2.4	1340	735	661
	15% AgNO ₃ in 10:1	A. 49.8 ± 14.7	1730	511	487
	16% AgNO ₃ in 20:1	A. 25.9 ± 6.8 B. 3.8 ± 0.88	1810	291	220

The cellular viability assay showed that, in most cases, the NPs synthesized using epinephrine induced a prolific response in the mitochondrial function in both the MAC and HaCaT cell lines at both 50 µg/mL and 100 µg/mL concentrations (Fig. 53 A, B). The highest increase in mitochondrial function of the MAC cells was seen in the 20:1 sample, with an increase of approximately 70-80 percent above the control cells, in both the 50 µg/mL and 100 µg/mL concentration. All other samples produced a 30-60 percent increase over the control in the MAC cell line at both 50 µg/mL and 100 µg/mL concentrations. In the HaCaT cell line, the highest increase in mitochondrial function was measured in the 100 µg/mL concentrations, with increases between 10-30 percent above the control. For most of the 50 µg/mL concentrations, the increase in HaCaT mitochondrial function was found to be 10-25 percent above the control. Along with cell viability, membrane integrity was examined by measuring the amount of LDH leaked by the cell. The MAC cells demonstrated the most membrane leakage, ranging 0-10 percent higher than the control, when exposed to 50 µg/mL concentrations. When the MAC cells were exposed to the 100 µg/mL concentration, most samples induced a slight decrease in membrane leakage. In general, the MAC cells exhibited no significant increase in membrane leakage when exposed to the silver NPs synthesized with epinephrine (Fig. 53). The HaCaT cells displayed minimal membrane leakage in all samples at both the 50 µg/mL and 100 µg/mL concentrations. When exposed to the 50 µg/mL of the 1:1, 2:1 and 10:3 ratio samples, a slight decrease of membrane leakage below the control was measured. No significant difference was measured between the control cells membrane leakage and the 10:1 and 20:1 ratio samples at 50 µg/mL. At a 100 µg/mL concentration of the 1:1 and 10:3 ratio samples, the HaCaT cells exhibited an increase in membrane leakage of 10-15 percent. For the ratios of 2:1, 10:1, and 20:1, there was no significant difference when compared to the control in membrane leakage at the 100 µg/mL concentration (Fig. 53D).

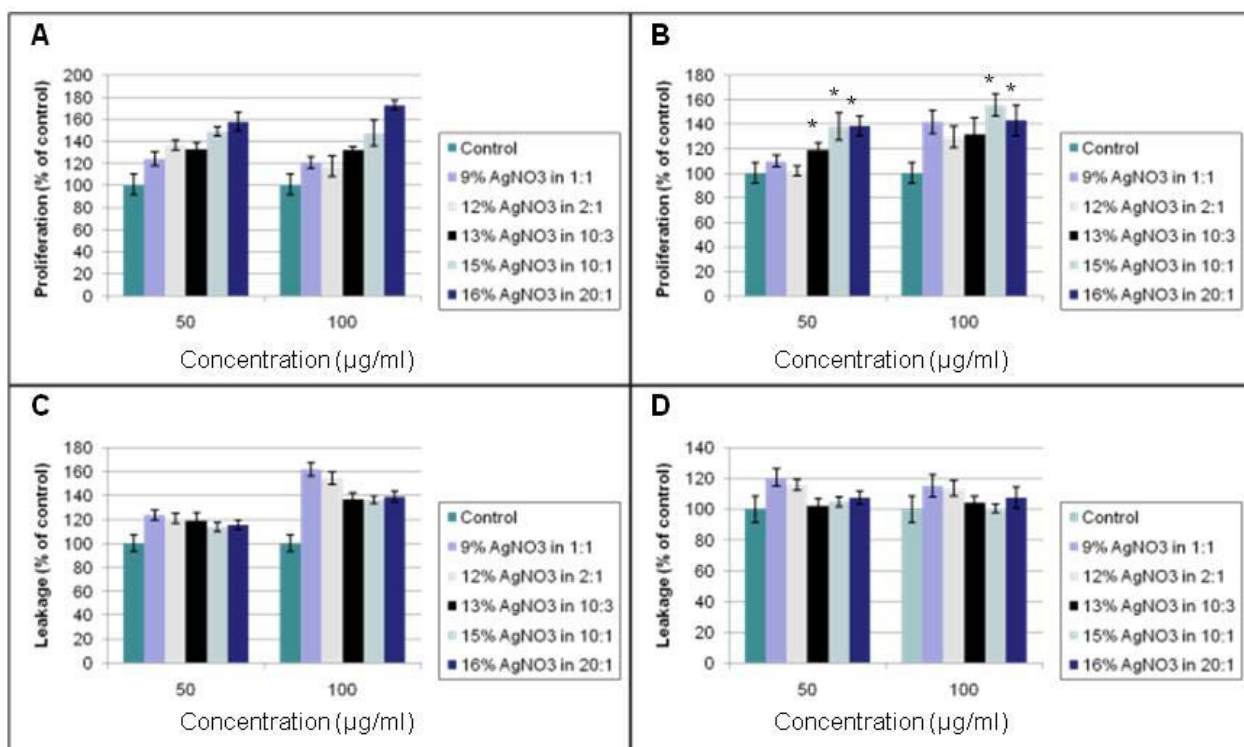


Figure 53. Epinephrine synthesized Ag nanoparticle cytotoxicity assays in MAC and HaCaT cell lines. A. Mac mitochondrial function; B. HaCaT mitochondrial function; C. Mac membrane leakage; D. HaCaT membrane leakage.

The cellular viability assay showed that the tea extract synthesized NPs induced a prolific response in the mitochondrial function in both the MAC and HaCaT cell lines at concentrations of 50 µg/mL and 100 µg/mL (Fig. 54 A, B). The highest increase in mitochondrial function of the MAC cells was seen in the 20:1 sample at 50 and 100 µg/mL, with an increase of approximately 110-120 percent above the control cells. In general, the sample's ability to increase mitochondrial function increased with decreased concentration of tea extract at both 50 µg/mL and 100 µg/mL concentrations. In the HaCaT cell line, the highest increase in mitochondrial function was measured in the 20:1 ratio at 100 µg/mL concentration, with an increase of approximately 50 percent above the control. For the higher concentrations of tea extract, the increase in mitochondrial function was between 4-40 percent for the 50 µg/mL concentration and 15-40 percent for 100 µg/mL concentration. Each sample showed a higher increase in the HaCaT mitochondrial function when exposed to 100 µg/mL than the 50 µg/mL concentration. As with the MAC cell line, the sample's ability to increase mitochondrial function increased with decreased concentration of tea extract at both 50 µg/mL and 100 µg/mL concentrations.

Again, membrane integrity was examined by measuring the amount of LDH leaked by the cell. The MAC cells demonstrated the most membrane leakage, ranging from 0-25 percent higher than the control, occurred when exposed to 100 µg/mL concentrations of all samples, with no discernable pattern. When the MAC cells were exposed to the 50 µg/mL concentration, the samples induced no significant difference in the 2:1, 10:1, and 20:1 samples. In the 1:1 and 10:3 ratio samples, an increase of membrane leakage was measured at 20 percent and 10 percent, respectively, above the control (Fig. 54C). The highest increase in membrane leakage for the

HaCaT cell line was measured 25 percent above the control, when exposed to 50 $\mu\text{g/mL}$ and 100 $\mu\text{g/mL}$ concentrations of the 1:1 ratio sample. When exposed to 50 $\mu\text{g/mL}$ and 100 $\mu\text{g/mL}$ concentrations, the 10:3 ratio sample for the HaCaT cells showed no significant increase in membrane leakage. At 100 $\mu\text{g/mL}$ concentration, the other samples induced a 5-25 percent increase in membrane leakage (Fig. 54D).

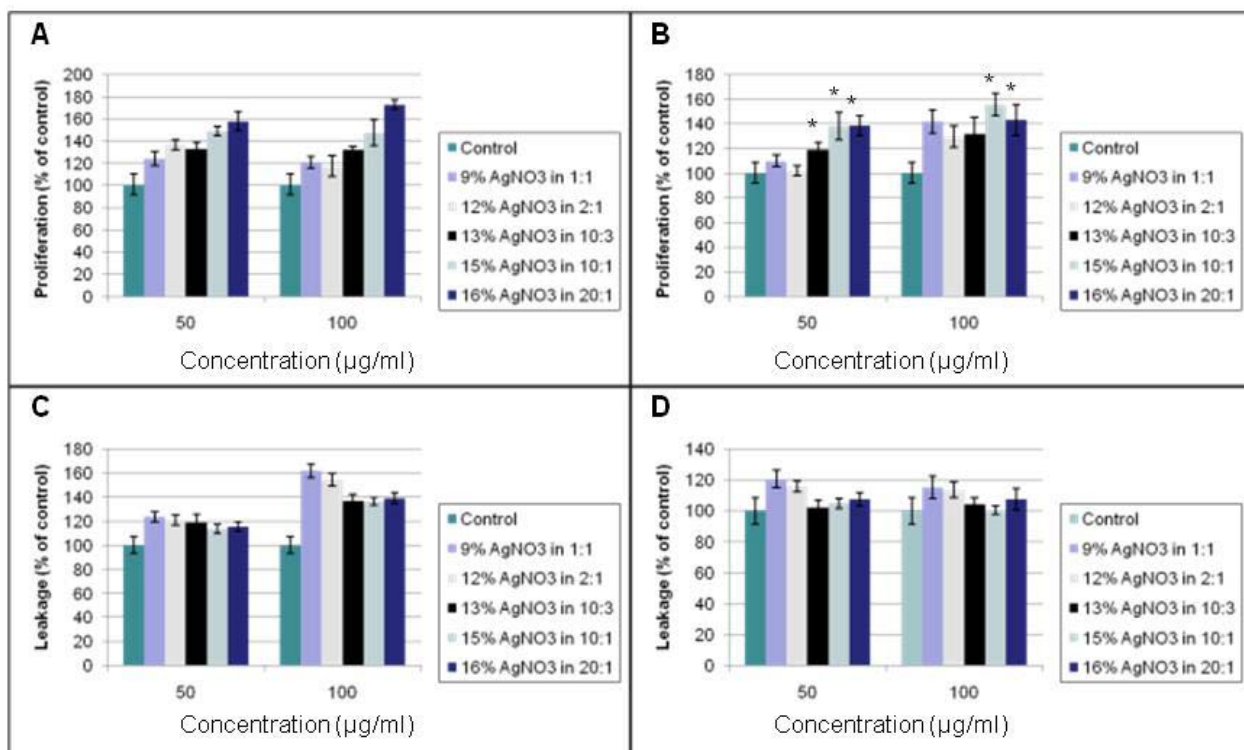


Figure 54. Tea Extract synthesized Ag nanoparticle cytotoxicity assays in MAC and HaCaT cell lines leakage. A. Mac mitochondrial function; B. HaCaT mitochondrial function; C. Mac membrane leakage; D. HaCaT membrane leakage.

The MAC control (Fig. 55A) showed healthy macrophage cells that were spherically symmetrical, consistent in size, and had a tendency to cluster. When the MAC cells were exposed to the 1:1 (water:epinephrine) ratio sample, few silver NPs were observed interacting with the cells (Fig. 55B). The particles that were seen interacting with the cells appeared to be on the cell membrane and not inside the cell. The exposed cells appeared to be slightly larger than the control cell but still maintained their spherical symmetry. When the MACs were exposed to the 2:1 ratio sample, silver NPs were seen interacting with the cell membrane boundary (Fig. 55C). Also, these cells appeared to be generally symmetrically and had a fairly consistent size when compared with the control cells. Figure 55D shows an image of the 10:3 ratio sample that has numerous cells interacting with the Ag NPs. The cell in the middle of the image has interacted with many silver NPs and has confined into a relatively small space; the relative brightness and proximity of particles has created a bright flare when imaged. Also, an occasional change in the cellular structure is seen throughout the culture. This can be seen at the bottom of the image (Fig. 55D), where the cell has a slight elongated appearance and has interacted with many NPs in close proximity causing the flare in the middle of the cell. When exposed to the 10:1 ratio sample there is a notable change in cell morphology; some cells became

elongated and damage to the cellular membrane was observed (Fig. 55E membrane damage seen in upper right corner). Also, there are many cells that were “decorated” with the silver NPs and still maintained their spherical symmetry and generally appeared healthy when compared with the control cells. Some of the NPs were on the surface of the cell; however, most are believed to be internalized by the cell. When the MAC cells were exposed to the 20:1 sample, the cells appeared slightly smaller and less symmetric than the controls and NPs are noted on the outskirts of the cell membrane (Fig. 55F). These NPs were most likely on the cell membrane barrier and had not been taken into the cell. In most cases, excluding the 10:1 ratio, the cells maintained their tendency to grow in clusters.

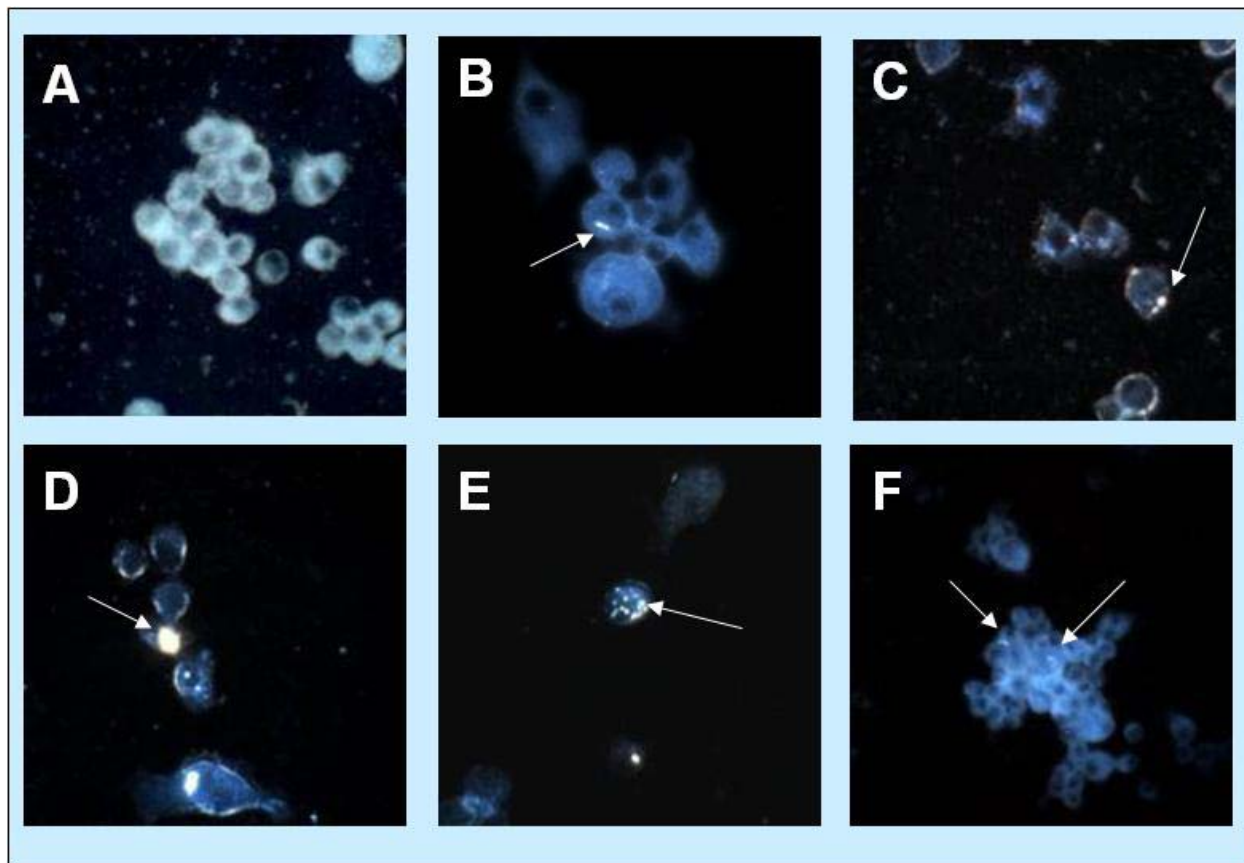


Figure 55. CytoViva images of MAC cell interactions with Ag nanoparticles. A. Control cells; B. 1:1 ratio of water to epinephrine; C. 2:1 ratio of water to epinephrine; D. 10:3 ratio of water to epinephrine; E. 10:1 ratio of water to epinephrine; F. 20:1 ratio of water to epinephrine.

The HaCaT control (Fig. 56A) revealed healthy HaCaT cells that consisted of confluent monolayers. When exposed to the 1:1 (water: epinephrine) ratio sample, the HaCaT cells showed very minimal interactions with the silver NPs (Fig. 56B). The particles that were observed interacting with the cells appeared as agglomerates on the cellular membrane and had no significant effect on the HaCaT cellular morphology. When the HaCaTs were exposed to the 2:1 ratio sample, more silver NPs were seen interacting with the cells but again appeared on the membrane boundary and caused no significant change in the morphology of the cells (Fig. 56C). Exposure to the 10:3 ratio sample exhibited the most interaction between the HaCaT cells and the silver epinephrine NPs. Numerous particles were observed interacting with the cell but most

still appeared to remain on the cell membrane, causing little to no change in cell morphology (Fig. 56D). When exposed to the 10:1 ratio sample, a minimal number of NPs were seen, and most were on the cell membrane. However, there was a slight change in the cellular morphology; cells appeared smaller and slightly elongated (Fig. 56E). When the HaCaT cells were exposed to the 20:1 sample, the cells appeared identical to the control cells in morphology and integrity. The only noticeable difference was the occasional NP seen on the cellular membrane (Fig. 56F). With all samples, the silver epinephrine NPs were seen interacting with the cell membrane and not taken into the cell as they had been in the MAC cell cultures.

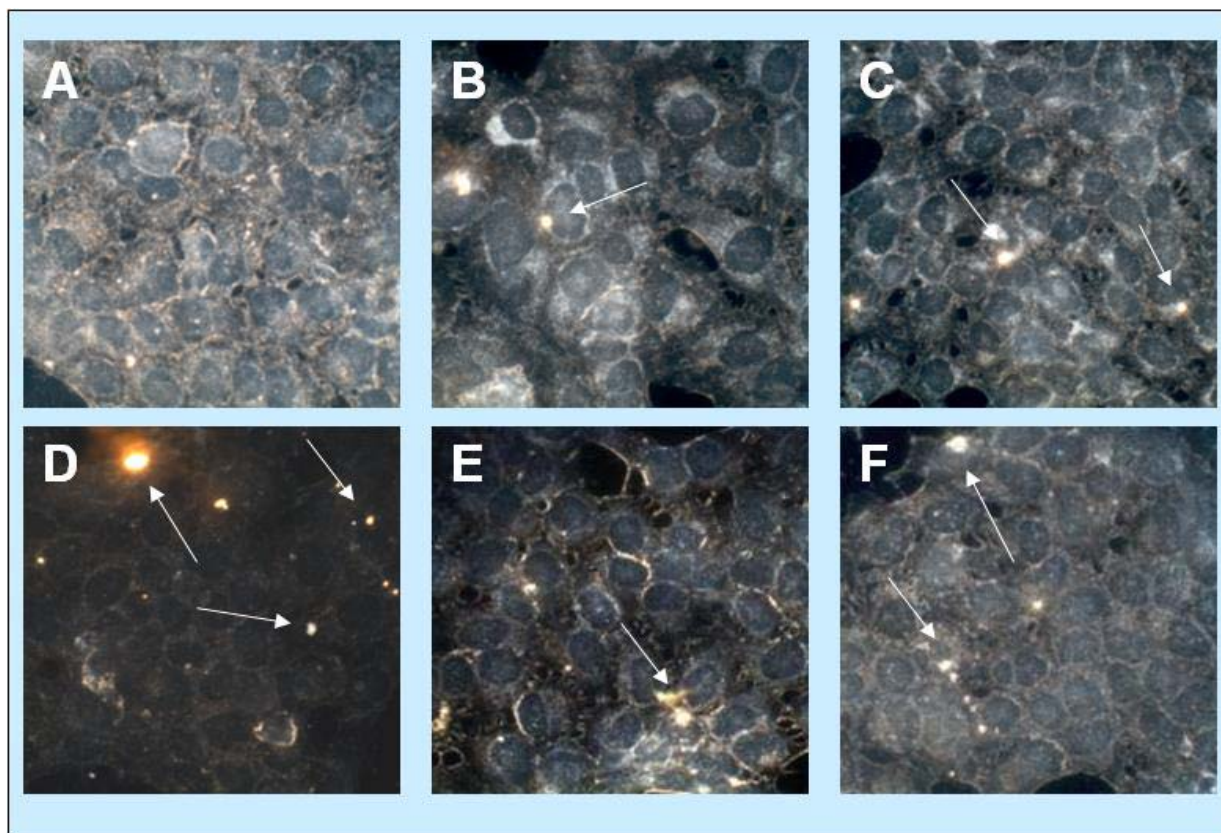


Figure 56. Cytoflourescence images of HaCaT cell interactions with Ag nanoparticles. A. Control cells; **B.** 1:1 ratio of water to epinephrine; **C.** 2:1 ratio of water to epinephrine; **D.** 10:3 ratio of water to epinephrine; **E.** 10:1 ratio of water to epinephrine; **F.** 20:1 ratio of water to epinephrine.

The image of the MAC control cells (Fig. 57A) shows cells that are symmetrical, have a consistent size, and with a tendency to cluster. When the MAC cells were exposed to the 15 $\mu\text{g/mL}$ concentration of the 1:1 ratio sample (Fig. 57B), the cells appeared to have immense interaction with the particles. Cells appeared elongated and decorated with NPs throughout the entirety of the cell. Most cells had grown tails that contained a large amount of silver NPs inside of them. It is believed that the majority of the NPs had been taken into the cell and had had adverse effects on cellular function. When the MAC cells were exposed to the 2:1 ratio sample, a drastic change in morphology of the cells occurred, with many having octopus-like protrusions. Fewer particles were observed interacting with the cells but seemed to have a great effect in changing the morphology of the cells; cells were no longer spherical, appeared enlarged, and had little to no symmetry (Fig. 57C). When exposed to the 10:3 ratio sample, the MAC cells

maintained the spherical morphology and symmetry. However, almost all cells observed showed extensive interaction with the NPs and, in most cases, showed a large degree of internalization of these NPs (Fig. 57D). When exposed to the 10:1 ratio sample, there was a notable increase in the size of the cells, and a decrease in definable plasma membrane (Fig. 57E). The NPs observed appeared to be attached to the cell membrane but not inside the cell itself. When the MAC cells were exposed to the 20:1 sample, the cells were less symmetric and had elongated, with some NPs interacting with the cellular membranes (Fig. 57F). Most of these NPs were most likely on the cell membrane barrier, with few having been taken into the cell. In the 10:1, 2:1, and 1:1 ratio samples, cells lost their tendency to grow in clusters, where the 10:3 and 20:1 ratio samples maintained this tendency.

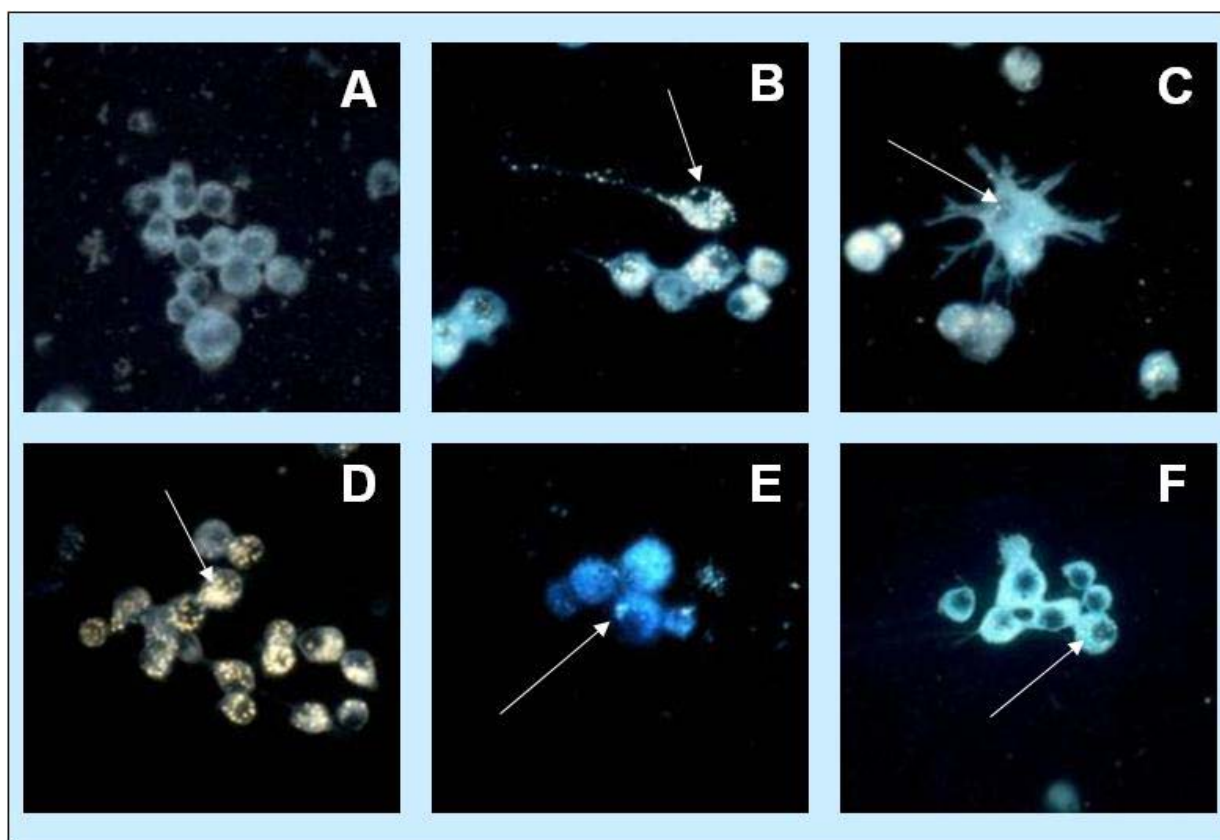


Figure 57. Cytoviva images of MAC cell interactions with Ag nanoparticles in MAC cells. A. Control cells; B. 1:1 ratio of water to tea extract; C. 2:1 ratio of water to tea extract; D. 10:3 ratio of water to tea extract; E. 10:1 ratio of water to tea extract; F. 20:1 ratio of water to tea extract.

The HaCaT control cells (Fig. 58A) showed cells that were a confluent monolayer. When the HaCaT cells were exposed to the 1:1 ratio sample (Fig. 58B), extensive interaction was observed between the HaCaT cells and the silver tea NPs; many particles were believed to have crossed the membrane barrier but had induced no significant change in cellular morphology. Observations of the HaCaT exposure to the 2:1 ratio sample revealed drastic cellular interactions with the silver NPs (Fig. 58C). As in the 1:1 ratio sample, the particles appeared to have crossed the membrane barrier but appeared to have no adverse effects on the cellular integrity. When exposed to the 10:3 ratio sample, the HaCaT cells observed showed

extensive interaction with the silver NPs; most particles again appeared to be internalized (Fig. 58D). When exposed to the 10:1 ratio sample, there was a notable decrease in the number of NPs interacting with the cells (Fig. 58E). However, these particles still appeared to be internalized into the cell membrane. When the HaCaT cells were exposed to the 20:1 sample, cells showed a dramatic decrease in interactions with the silver tea NPs (Fig. 58F). The few particles that were seen were still believed to be internalized by the cell along with a few interacting with the membrane barrier; however the cells appeared to have a loss of connectivity with surrounding cells. In general, the amount of interacting silver NPs decreased with decreasing concentrations of tea extract.

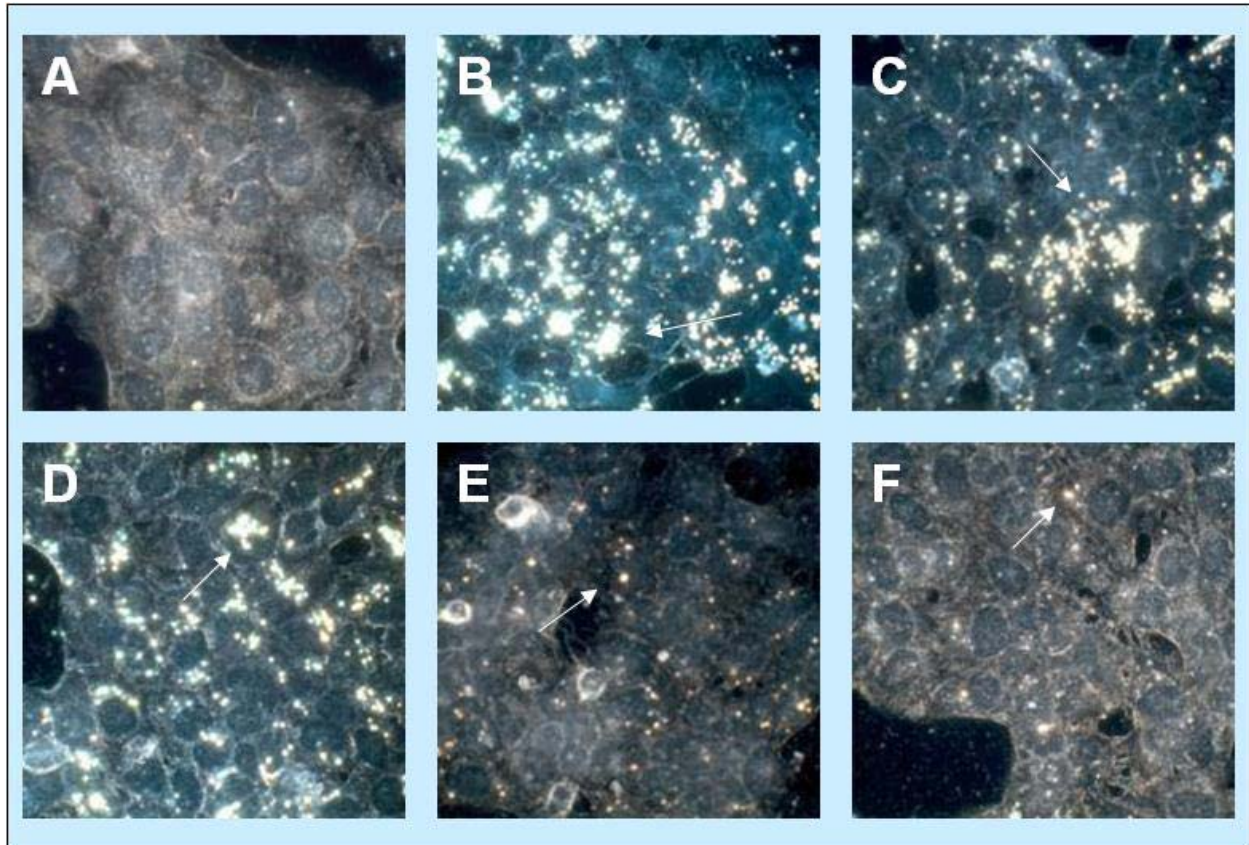


Figure 58. Cytofluorescence images of HaCaT cell interactions with Ag nanoparticles in MAC cells. A. Control cells; B. 1:1 ratio of water to tea extract; C. 2:1 ratio of water to tea extract; D. 10:3 ratio of water to tea extract; E. 10:1 ratio of water to tea extract; F. 20:1 ratio of water to tea extract.

In-vitro biocompatibility of silver nanoparticles anchored on multi-walled carbon nanotubes

The MWCNT tubes differ in chemical reactivity with CNx-MWCNTs being the most reactive (MWCNTs < COx-MWCNTs < CNx-MWCNTs). Figure 59 shows STEM images of the CNTs/Ag composites and their particle size distribution, the MWCNTs/Ag composite is presented in Figure 59A.-59C. with an average particle size of 6.64 ± 2.25 nm, Figure 59D.-1F. shows the COx-MWNTs/Ag, this composite present a bimodal histogram in the particle size, the first peak in ~ 8 nm and the second one in ~ 12 nm with an average size of 11.75 ± 4.65 nm. Finally Figure 59 G.-I. shows the CNx-MWNTs/Ag composite, the material exhibit a bimodal behavior in the particle size (~ 10 and ~ 13 nm) giving an average value of 13.25 ± 3.94 nm. The diameter distribution of silver NPs is shown in Figure 60. Figure 61 shows the X-ray diffraction patterns of the three composites, the G(002) peak correspond to graphite, the others belong to silver NPs, the particle size obtained from the XRD data using the Scherrer equation is illustrated in Table 12, the numbers are the miller index. Figure 62 shows the silver NPs anchored on the MWNT sidewall.

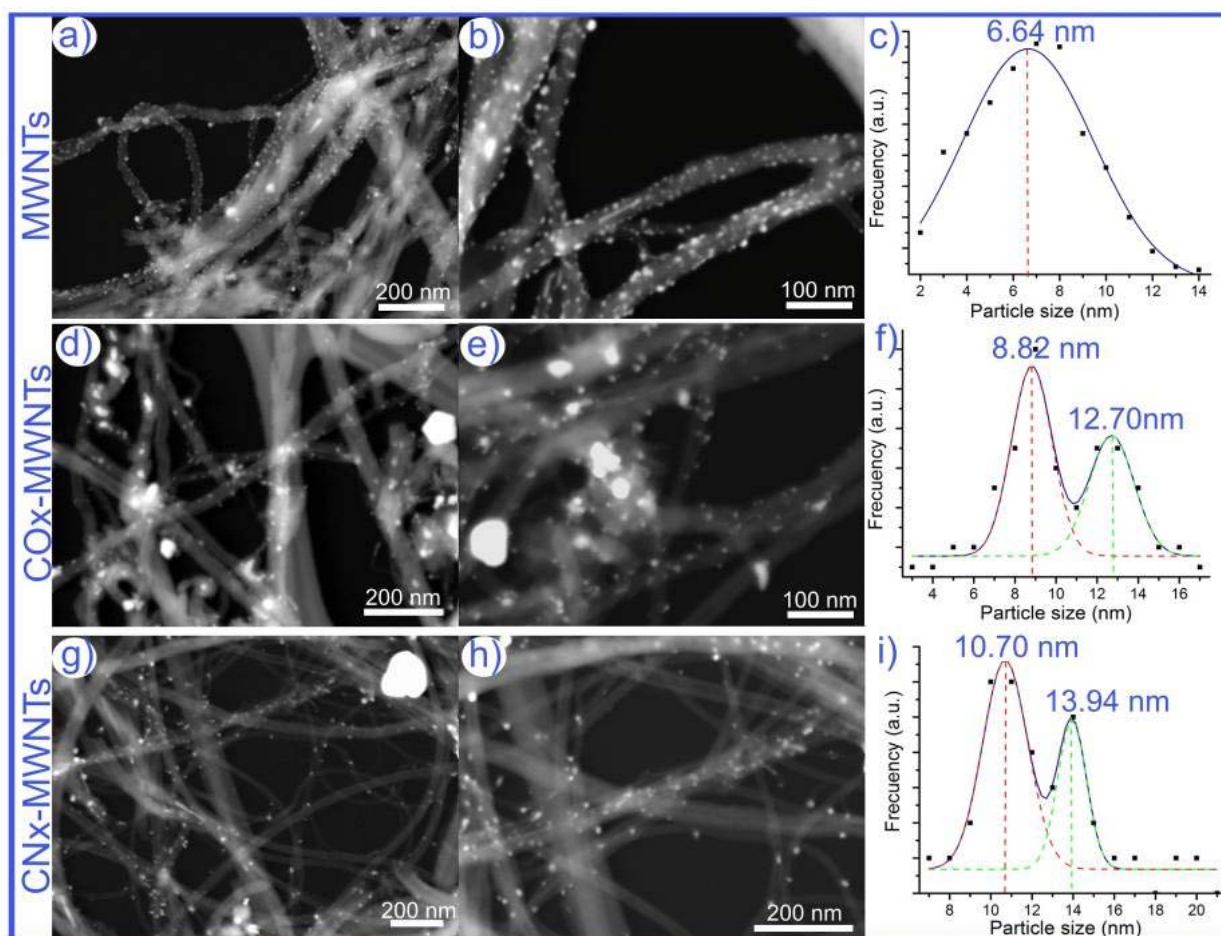


Figure 59. STEM images (A, B, D, E, G, H) and particle size determined via DLS (C, F, I). A,B. MWCNT; C. MWCNT 6.64 nm; D,E. COx-MWNTs; F. Cox-MWNT 8.82 nm and 12.70 nm; G,H. CNx-MWNT; I. CNx-MWNT 10.70 nm and 13.94 nm.

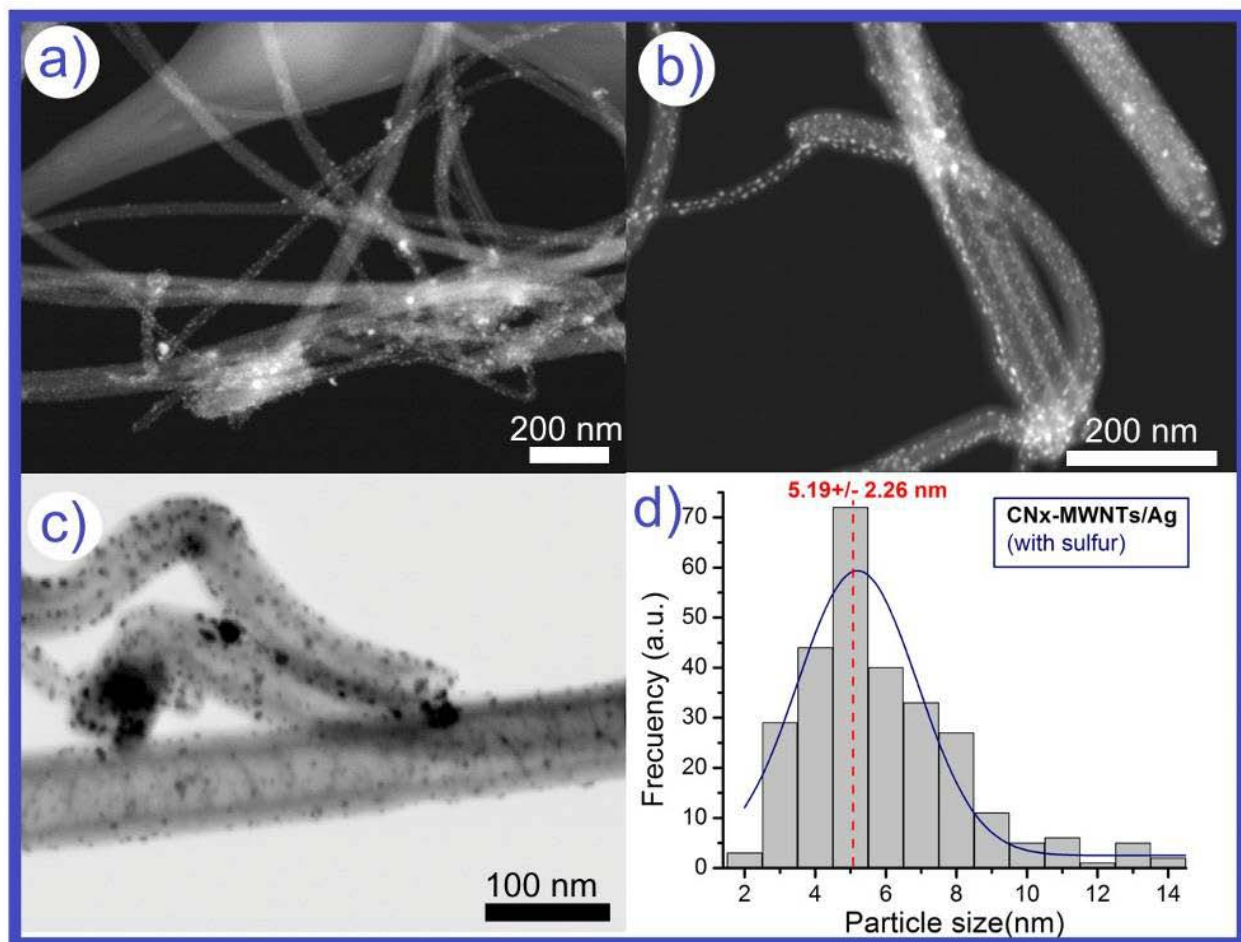


Figure 60. CNx-MWNTs/Ag-S composite characterization. A-C. SEM images of the CNx-MWNTs/Ag composite with sulfur on the surfaces. The composite exhibits high load of Ag particles; **D.** Ag particle size distribution with an average value of 5.19 ± 2.26 nm.

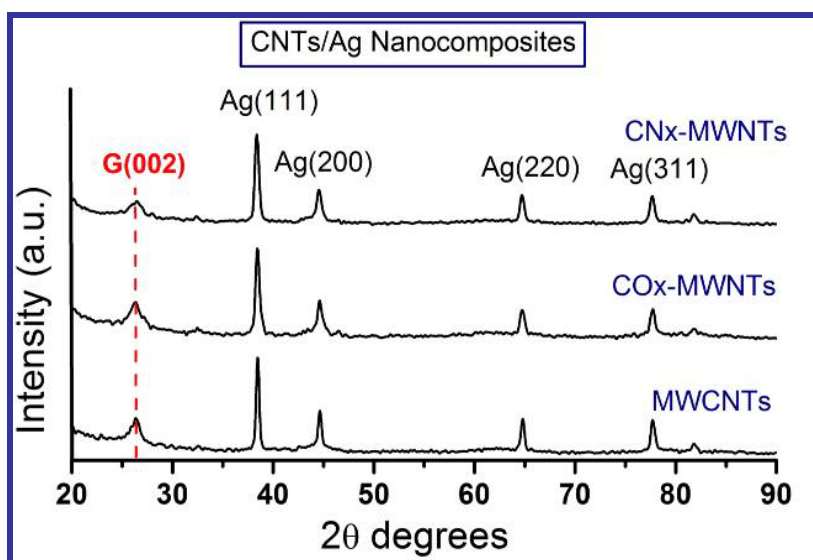


Figure 61. X-ray diffraction patterns of CNTs/Ag composites.

Table 12. Ag Particle Size on Different Types of CNTs.

Nanotubes	Ag(111) nm	Ag(200) nm
MWNT	27.94	27.78
COx-MWNTs	19.50	27.87
CNx-MWNTs	19.97	21.13

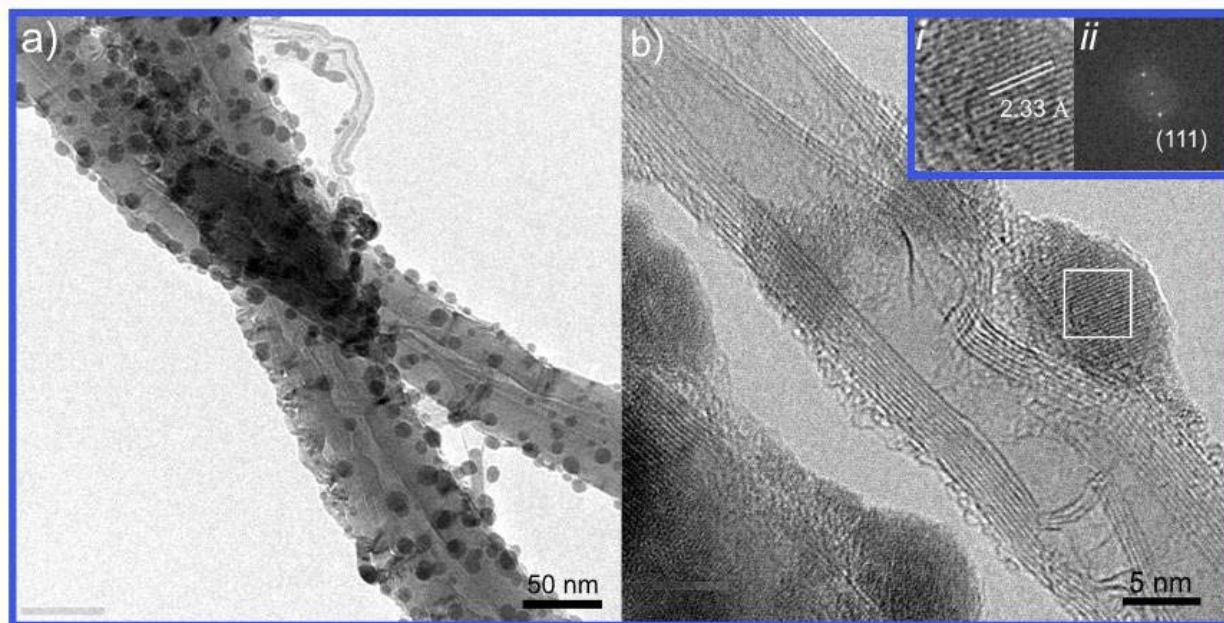


Figure 62. TEM images of MWNTs/Ag composites. A. A high number of NPs are shown anchored on the nanotube wall; **B.** Higher magnification of the MWNTs/Ag composite, the inset illustrates a magnification of Ag NP and their Fast Fourier Transform (FFT) showing the Ag (111) plane. *Characterization of nanomaterials work was done in collaboration with Prof. Mauricio Terrones, Advanced Materials Department, IPICYT, Mexico.*

The MTS results of the HaCaT cells exposed to varying concentrations of Ag-MWCNTs shows no toxicity at 24, 48 or 72 hours at any of the concentrations used. At concentrations of 25 $\mu\text{g/mL}$, 50 $\mu\text{g/mL}$ and 100 $\mu\text{g/mL}$ there is some toxicity shown at the 1 week time points. The Ag-CNx shows no toxicity at 24, 48, 72 or 168 hours for any of the concentrations. The Ag-COx shows no toxicity either, but they do show slightly increased cell viability at all concentrations and timepoints. All particles show increased cell viability particularly at all concentrations at the 48 hour timepoint (Fig. 63).

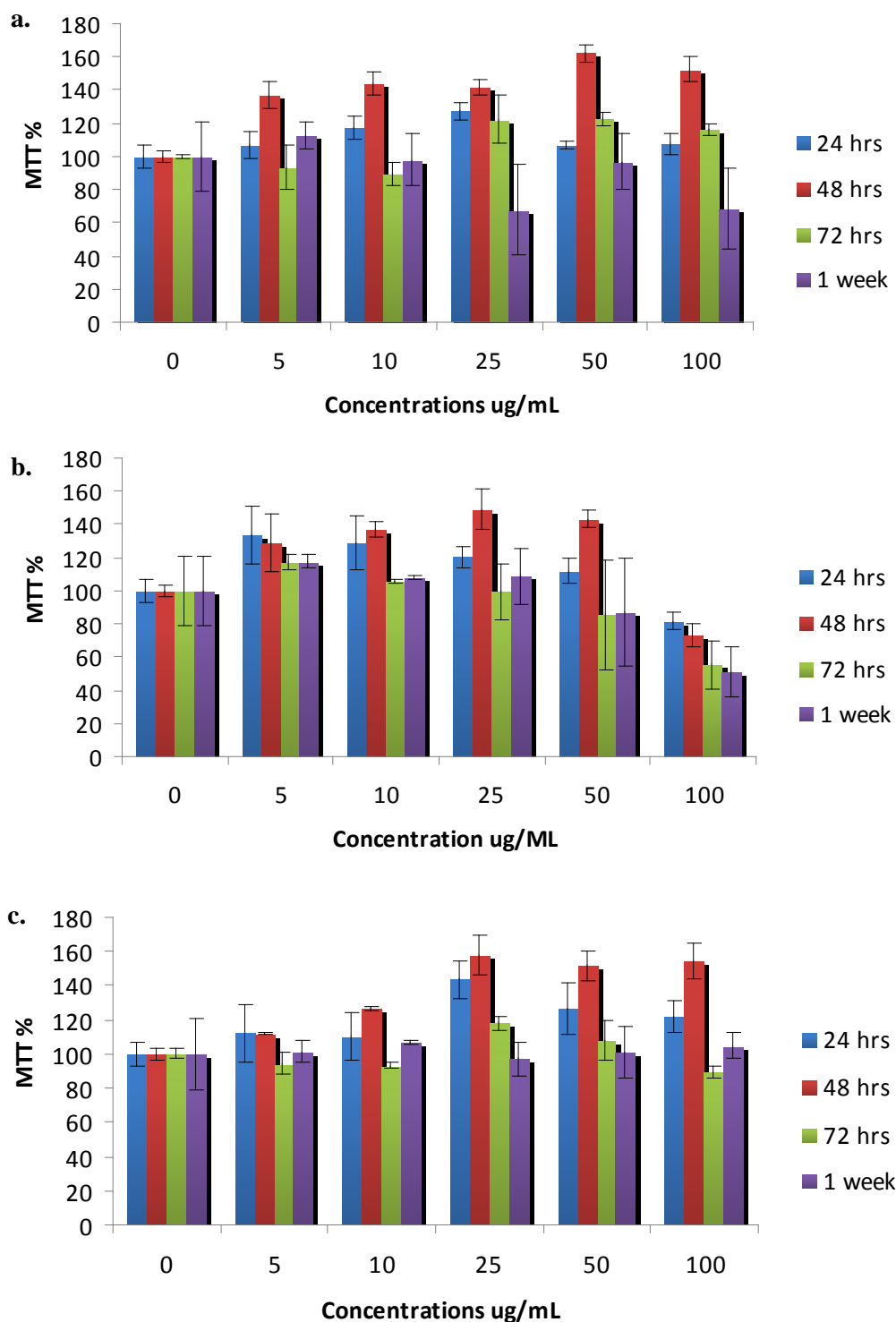


Figure 63. MTS results. **A.** MTS results of Ag-CNx at concentrations of 0, 5, 10, 25, 50 and 100 μ L in HaCaT cells exposed to the concentrations for 24, 48, 72 and 168 h; **B.** MTS results of Ag-MWCNT at concentrations of 0, 5, 10, 25, 50 and 100 μ L in HaCaT cells exposed to the concentrations for 24, 48, 72 and 168 h; **C.** MTS results of Ag-MWCNT at concentrations of 0, 5, 10, 25, 50 and 100 μ L in HaCaT cells exposed to the concentrations for 24, 48, 72 and 168 h.

All three functionalized MWCNT are entering the cells and binding to the nucleus or nuclear region based on the CytoViva imaging. We can also determine the binding due to the high concentration of MWCNTs in the images taken at 1 week. The cells had been washed and placed in exposure media for a week, therefore for the tubes to be present there must be binding in the nucleus. There appears to be some actin filament disruption caused by the Ag-MWCNT (Fig. 64 and 65).

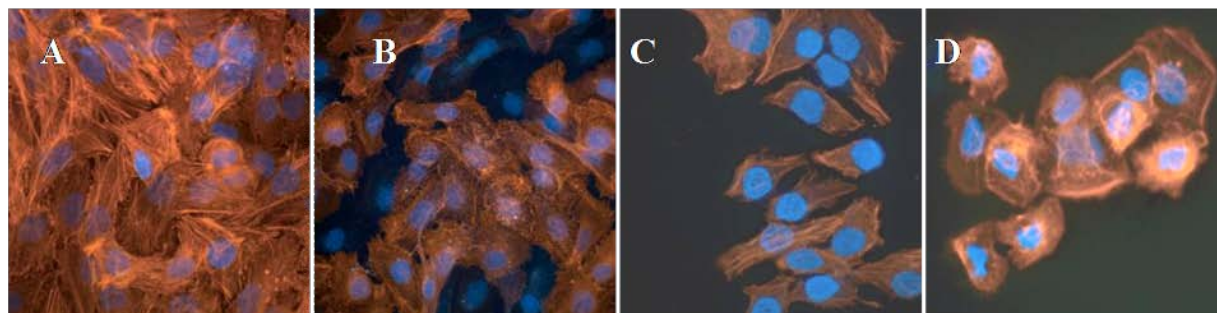


Figure 64. Control HaCaT cells at different time points. A. 24 h; B. 48 h; C. 72 h; D. 168 h.

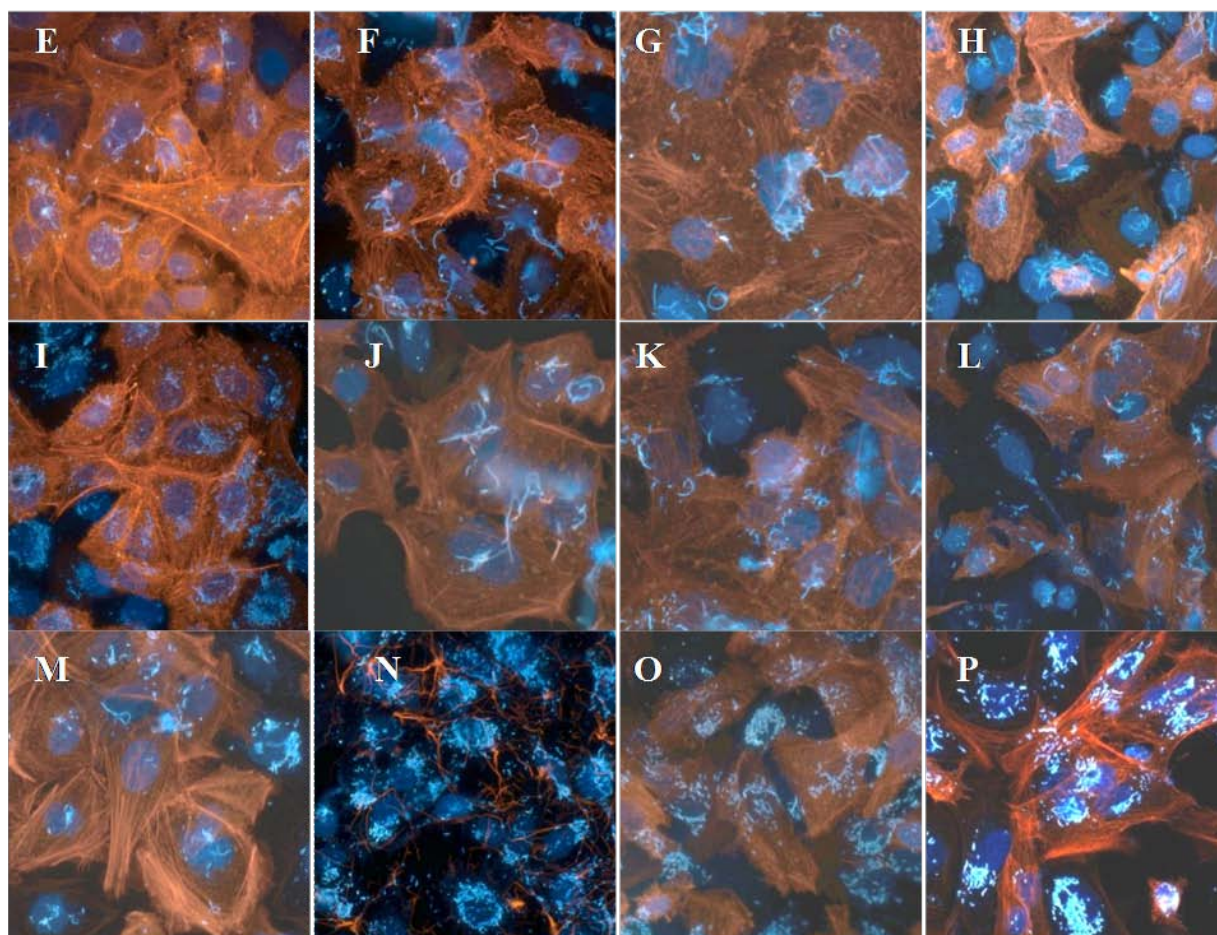


Figure 65. Exposed cells at different time points. Ag-MWCNTs at E. 24 h; F. 48 h; G. 72 h; H. 168 h, Ag-CNx at I. 24 h; J. 48 h; K. 72 h; L. 168 h, and Ag-COx at M. 24 h; N. 48 h; O. 72 h; P. 168 h.

Some of the actin filament disruption could be due to the exposure media, because the cells do not grow as well in this due to the lack of FBS. This is also indicated in the control cells, which appear to become rounded over time. Each picture with each particle type shows localized nuclear binding with the nucleus stained blue and the actin filaments stained red/orange. The particles appear as the bright spots. There appears to be limited actin filament disruption in comparison to the control pictures. Binding can be determined based on the number of particles seen even after the 1 week time period in the exposure media.

Biocompatibility of carbon foam substrates for osteoblasts growth

Previous studies have shown that surface topography greatly affects how cells grow on a substrate. Two types of microcellular carbon foam were researched versus flat graphite. In addition to topography, surface modifications can greatly affect how various cell lines grow and function. Carbon foam was coated with silicon dioxide, and collagen. After the carbon foam was coated and cells were seeded, they were viewed in an SEM. As shown in figure 66, the cell growth was seen extending across and within pores in the uncoated carbon foam (UC). Cell growth on SiO₂ coated samples was observed to have full growth on the surface and within pores with much less extensions across pores. Growth on collagen coated foam was very similar to silicon dioxide samples in that the cells cover the whole surface of the foam, but no cell extension was visible.

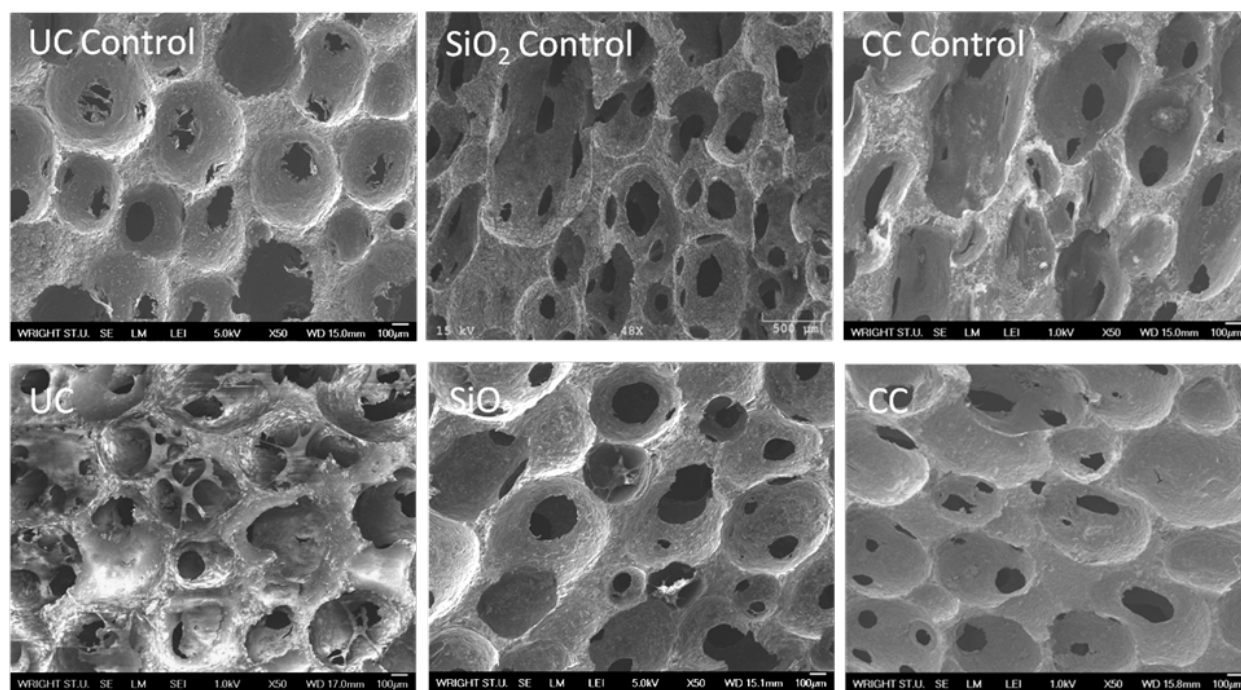


Figure 66. Osteoblast growth on carbon foams imaged via SEM. Cell growth was seen extending across and within pores in the uncoated carbon foam.

In order to view cell morphology, cell staining was performed for each of the surface coating samples. Under a fluorescence microscope a network of cells were seen spreading across the pores of uncoated foam substrates (Fig. 67). The amount of actin stain shown in each sample also varied between the coatings. Amount of actin seen in silicon dioxide coated foam

was much less than the uncoated, and collagen coated samples which could indicate stronger bonds between the cell and carbon foam.

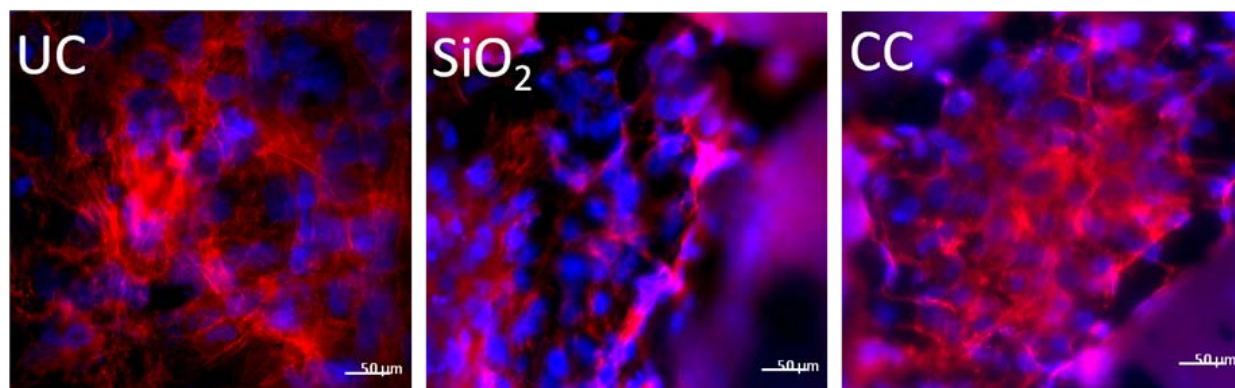


Figure 67. Fluorescent images of osteoblasts on carbon foam. These images show a network of cells spreading across the pores of uncoated foam substrates.

Mitochondrial function of human fetal osteoblasts was assessed as a measure of cell viability. As shown in figure 68, there was little to no toxicity of the carbon foam with osteoblast cells. This suggests that microcellular carbon foam, in addition to silicon dioxide and collagen coatings are biocompatible with this cell-line.

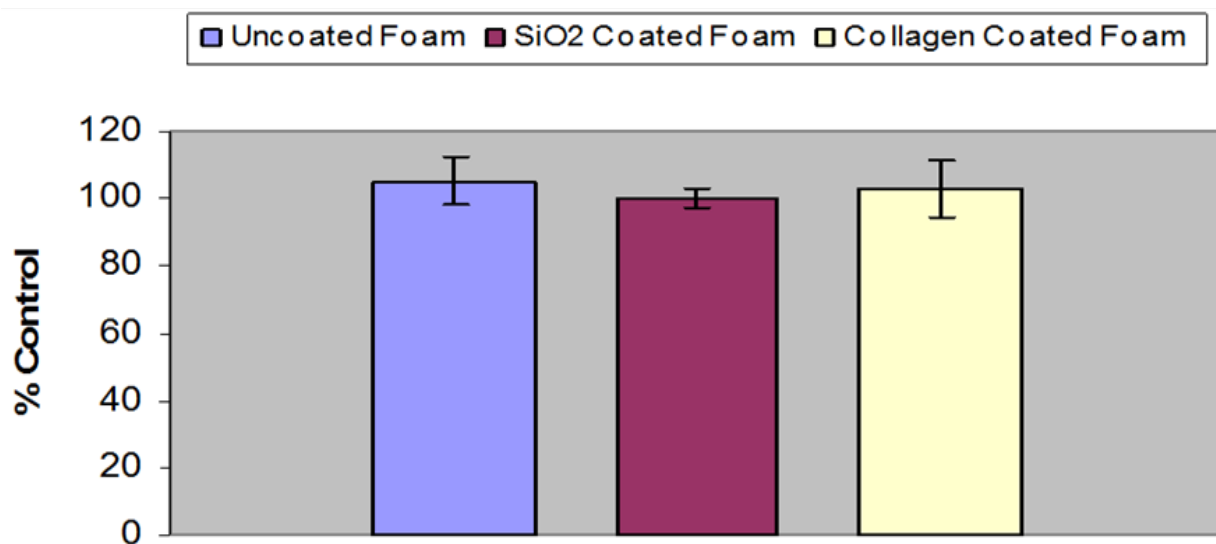


Figure 68. Mitochondrial function of human fetal osteoblasts as a measure of cell viability. Once the cells had grown for 72 h, cell viability was assessed by evaluating mitochondrial function using the CellTiter 96[®] AQueous One Solution assay.

CONCLUSIONS

Based on studies presented in this report, we have been able to develop many novel techniques in nanotoxicity research. In addition, we have uncovered unique properties of nanomaterials in biological systems that can be used in future applications. The knowledge obtained in each study is briefly summarized in the following paragraphs.

When studying the immune suppression in MRSA-infected human alveolar co-cultures, we were able to successfully establish an *in vitro* inhalation model to study the toxicity and biological effects of aluminum NPs. Furthermore, using this co-culture system, we evaluated how the presence of aluminum NPs alters cell viability, basic cell function, and the cells' ability to respond to pathogens at the molecular level. We discovered that while not necessarily toxic, these aluminum NPs impair the cells natural ability to respond to respiratory pathogens by altering gene activation and cytokine secretion.

The role of nanomaterial properties on their biological effects was evaluated in many of our studies. In evaluating the effect of crystal structure on toxicity of TiO₂, we were able to demonstrate that both size and crystal structure contributes to cytotoxicity and that the mechanism of cell death varies as a result of crystal structure. Based on these findings, the rutile TiO₂ ROS initiated apoptosis can be controlled for by treatment with antioxidants, thus making the anatase structure more toxic than the rutile.

The role of NP charge was shown in a study involving gold NPs, where both toxicity and real time PCR data show that charge on the surface of the NP plays a major role in its cytotoxicity. These findings reiterate the importance of thorough investigation of all NPs before use in any consumer products, especially medical devices to be used inside the body.

Shape was also shown to affect the biological interaction of gold NPs, where nanospheres were found to be non-toxic, which makes them great candidates for use in the medical community as drug delivery agents and treatments of certain cancers. The gold nanorods, on the other hand, seem to be extremely cytotoxic. Research has shown that CTAB, which was used as the capping agent in the synthesis of these rods, can be toxic to cells when used by itself. Future studies will test whether the amount of CTAB present in the nanorods solution is enough to cause the toxicity to the human keratinocytes. Nanospheres also capped with CTAB will also be tested to help determine if the CTAB is the cause of the toxicity or if it is really shape-dependent.

Amorphous silica NPs showed size- and dose-dependent toxicity and the smallest size (35 nm) at the highest concentration (200 µg/mL) generated the lowest reduced glutathione levels. ROS levels were similar in the controls and dosed cells, indicating mechanism of toxicity does not seem to be through oxidative stress.

Another study showed that NP toxicity can be size dependent, where cells exposed to silver NPs suffer morphological modifications, LDH leakage, mitochondrial dysfunction, increased generation of ROS, and reduced mitochondrial membrane potential. This preliminary data suggest that oxidative stress is likely to contribute to NP cytotoxicity for the 15 nm silver NPs. However, further study is required to characterize the nature of silver inside cells.

In a separate study evaluating the biological interactions of silver NPs, it was established that silver NPs, even at concentrations believed to be benign, were able to impair spermatogonial stem cell proliferation. This effect was due in part to a decrease of Fyn kinase phosphorylation and activity, which disrupted GDNF signal transduction and inhibited the up-regulation of *N-myc* (Fig. 6c), a transcription factor that activates key components of the cell cycle machinery in C18-

4 cells [72]. Moreover, this phenomenon was detectable at sub-toxic levels, and occurred regardless of NP size or surface coating. We have illustrated that not only do NPs have an effect on the cellular environment, but the cellular environment impacts the physicochemical properties of the NPs. This study demonstrates that when researchers coat materials to make them “biocompatible”, these materials must be fully characterized and evaluated within the cellular environment prior to claiming biocompatibility.

The effect of NP synthesis method was also shown in a study where silver NPs were synthesized using a “green” method involving the use of epinephrine or tea extract as a reducing and capping agent. NPs were successfully synthesized in an environmentally benign process, and these particles were nontoxic even at high concentrations (100 µg/mL). In fact, in most cases, these NPs created a prolific response in the cell models examined. These preliminary *in vitro* studies will need to be followed up by future *in vivo* studies before we can definitely say that they are more biocompatible, but this method of synthesis appears to be promising based on the initial *in vitro* studies.

The *in vitro* biocompatibility of silver NPs anchored on MWCNT was evaluated in order to determine the effect of NP immobilization on toxicity. The lack of toxicity combined with the particles ability to bind to the cell nucleus indicates a novel non-toxic method of delivering Ag NPs to the cell’s nucleus using MWCNTs exhibiting different doping groups. Further studies will be carried out to determine ROS production and binding using TEM.

Lastly, osteoblast growth on carbon foam substrates was shown to be a function of not only surface topography, but also surface modifications, which greatly influence bonding and morphology. Current and future research is being done on modifying the surface of microcellular carbon foam with the attachment of carbon nanotubes as well as applying an electric field to the samples. Various cell-lines will be grown in the same manner to view the effect of these modifications on their growth and proliferation. This study confirmed that the smaller pore size foam was much more suitable for cell growth than the larger pore sized foam.

BIN TRANSITIONS (FUTURE WORK)

As we end the Biological Interactions of Nanomaterials project, we look to the future to transition the knowledge gained during the time on this project toward applications. These applications include using nanomaterials to design biosensors for the detection of biomolecules. Detection may be accomplished at the intra-cellular levels, external to the body, or at any level in between. One of our future aims is to be able to exploit the unique properties of certain nanomaterials for the purpose of stand-off detection or control. Two initial ideas in this area, which involve the use of nanomaterials which are sensitive to electromagnetic radiation or magnetic fields, are presented in following sections.

External control of bio-functionalized nanoparticles for control of cell processes and signaling

A new initiative has been started to begin to apply some of the fundamentals which have been discovered through the Biological Interaction of Nanomaterials project. This new project, called the Nano-Biocontrol Project, has the following objectives:

- Functionalize nanomaterials (FNMs) with biomolecules
- Specifically target FNMs to DNA, RNA, or proteins
- Apply an EM field to the FNMs to cause the target to inactivate
- Design process to be reversible when EM field is removed
- Control cell function and processes

Gold NPs have recently been used in a wide array of applications for antimicrobial applications to sensors due to their unique properties. At the nanoscale level, gold exhibits unique physical, electrical, and chemical properties such as the ability to produce a visual color changes with particle size and aggregation. The solution will shift from red to blue as NPs aggregate more, and vice versa. The figure below shows this affect (Fig. 69).

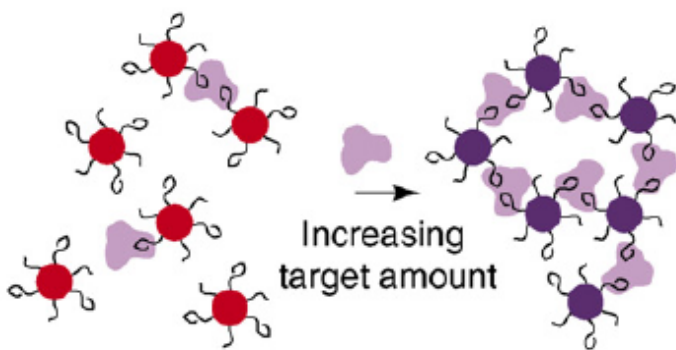


Figure 69. Color shift observed with increasing agglomeration of Au NPs.

Gold NPs also have a unique surface chemistry which allows proteins, DNA, and most other organic compounds to readily adhere to surface of the particle. This means these particles can serve as a platform for almost limitless applications. Gold NPs can also be “designed” in a wide variety of sizes and shapes fairly easily.

Aptamers are oligonucleic acid or peptide molecules that bind a specific target molecule. They can essentially be designed for almost any target as long as a sequence is known. Aptamers are currently being used in multiple potential applications such as for basic research and clinical purposes as macromolecular drugs and they can be combined with ribosome to self-cleave in the presence of their target molecule, also known as a riboswitch. The main disadvantage to aptamer use currently is that non-modified aptamers are cleared rapidly from the bloodstream, with a half-life of minutes to hours, mainly due to nuclease degradation and clearance from the body by the kidneys.

The aim of this project is to functionalize gold NPs with aptamers to increase the half-life of the aptamer as well as increase the specificity of the NP. Gold NPs with oligonucleotides attached to the surface have shown interesting properties with a targeted molecule, such as the ability to bind in such a manner to cause a change in color of the solution. The intensity of this color and even the color itself can be varied by certain factors creating a very useful biosensor with more than just a (+) or (-) feedback as it could distinguish concentration levels as well. Peptide aptamers are designed to interfere with other protein interactions inside cells by specifically binding to and preventing the binding of other molecules or proteins. It is also possible to use a substrate to hold NP with aptamer/ peptide/ ligand for detection of biomolecules. This can provide a functional nanoscale biosensor with an easy detection method. Figure 70 shows the functionalization of gold NPs with aptamers.

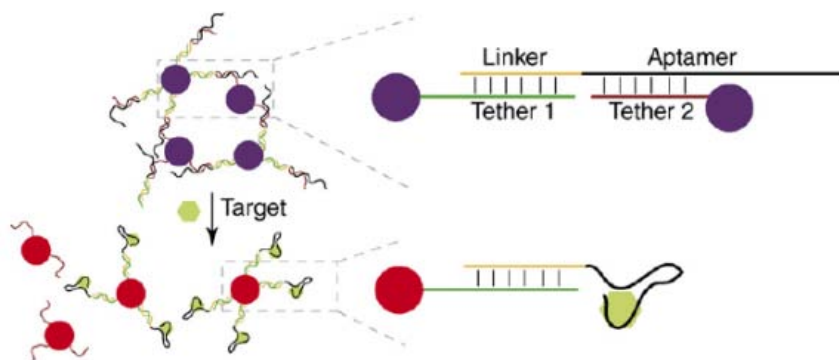


Figure 70. Gold NPs functionalized with aptamers.

The project plan is to design an independent operating, oscillating electromagnetic field producing circuit which can cause bio-functionalized gold NPs to heat up and cause its target to temporarily denature. The figure below shows a representation of the process (Fig. 71).

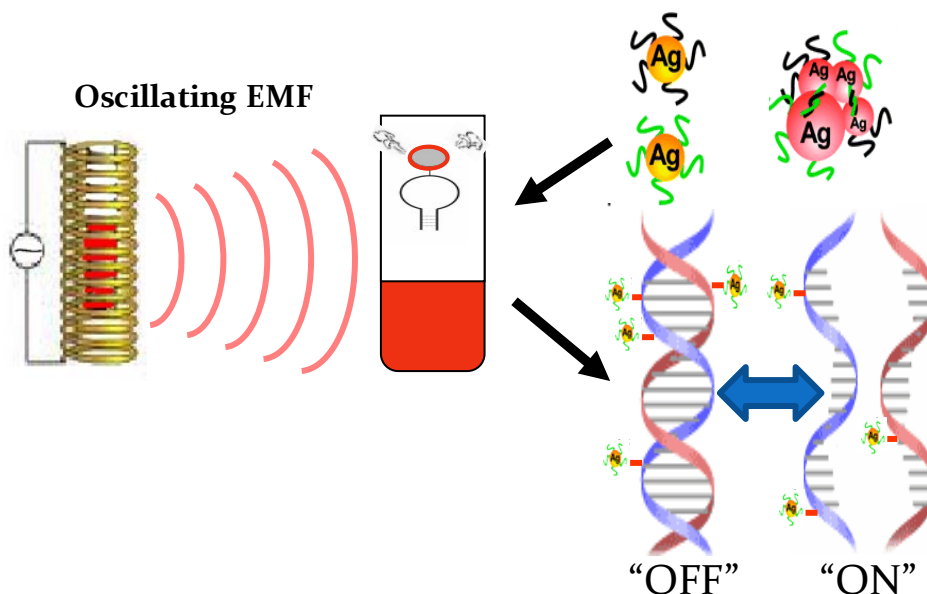


Figure 71. Representation of nano-biocontrol project.

The EMF producing component consists of a solenoid, with a modified centrifuge tube as a core, which is connected to a function generator to produce a controllable, oscillating magnetic field. As the current propagates upwards, winding through the coils, a magnetic field is induced inside the coils in the direction of the net current flow. The applied signal will be attempted at multiple frequencies, amplitudes, and times to determine the effect of these parameters on particle heating efficiency. The magnetic field in a solenoid is shown in the diagram below in figure 72. Also shown below are some of the equations used for calculations of various parameters in this project.

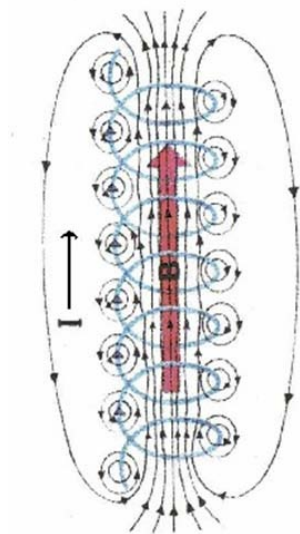


Figure 72. Magnetic field lines for a solenoid.

Equations used to determine various parameters:

- current
- number of coils
- signal frequency
- magnetic field strength
- exposure length
- energy transferred to particles
- heating of the particle

$$B_{max} = \frac{\mu_o N_B I_{max}}{l}$$

$$I = S_{AV} = \frac{E_{max}^2}{2\mu_o c} = \frac{c}{2\mu_o} B_{max}^2$$

$$\delta = \sqrt{\frac{2\rho}{2\pi f \mu_R \mu_o}}$$

$$Q = mc\Delta T$$

Major Project Steps:

- Synthesize NPs
- Design EMF Apparatus
- Test for Particle Heating
- Functionalize Nanoparticles with Simple Protein
- Test for Protein Denaturing and Reversibility of Process
- Functionalize Nanoparticles with a Target-Specific Oligonucleotide
- Test for Specific Binding of Functionalized Nanoparticles to Target
- Test for Control of Target
- Test Functionalized Nanoparticles In Vitro and Determine Cellular Impact
- Test for Control of Target In Vitro
- Au NPs

Completed Steps:

- Au NP formed using sodium citrate reduction method
- Initial trials yielded Au NP sizes which were too large for this application and needed to be decreased to below 10 nm

- Filtering of Au NP solution seems to be unnecessary since the particle size distribution is very narrow
 - In some cases it actually contaminated the sample
- Au NP Batch 5 produced the necessary sized particles (5 nm) with a small size distribution
- This was achieved by using a small amount of sodium borohydride with the sodium citrate

Current Work:

- Testing of EMF apparatus with Au NPs to determine heating effects
- Functionalization of Au NPs with oligonucleotides for target specific interaction
- Test for target (protein, DNA, etc.) denaturing with EMF applied to FNMs
 - Detect using spectrophotometer (UV-Vis)
- Run samples in DLS to assess extent of unfolding due to heating

Modulation of the immune system using electromagnetic nanoparticles: Potential application to reverse sleep deprivation and increase human performance

The recent strategy of the Air Force Research Laboratory (AFRL) is to enhance Intelligence, Surveillance, and Reconnaissance (ISR) technologies called Universal Situational Awareness (USA). This proposal engages the Applied Biotechnology, Human Effectiveness Directorate (RHPB) in this mission and provides an innovative approach to reverse sleep deprivation and enhance cognitive performance of war fighters. In the present study natural killer cells will be used as an immune model to examine the interaction of magnetic nanomaterials with the immune system. The interactions will show the activation of various cytokines involved in immune cell responses. Secondly the Natural Killer cells (NKC) will be used to show how the magnetic nanomaterials are able to modulate the production of cytokines. The cytokines produced by NK cells help to activate other areas of the immune system (T cells) and are the first line of defense against viruses. The natural killer cells have been show to decrease in times of sleep deprivation and stress such as wartime. The decrease in the NK cell activity allows warfighters to become susceptible to illness leading to a decrease in human performance and cognition. By modulating the immune production of cytokines the effects of stress and sleep deprivation on the warfighter's immune system can be reversed. The basic aspect of this proposal is the fundamental study to know how magnetic nanomaterials affect the immune system when it is exposed to the materials. The applied aspect is to develop nanoparticles as immune cell modulators to increase human performance optimization efficiently during stressful conditions.

Objectives:

- Synthesize biofunctionalized nanomaterials and translocate them into desired location into cells in a non-threatening way as a means to modulate cellular behavior.
- The understanding of how engineered nanoparticles of different geometries interact with cells and their receptors
- Molecular events involved in nanoparticle– membrane receptor binding, endocytosis and subsequent signaling activation.

- Modulating immune molecular activity using biofunctionalized nanoparticles under the influence of electro-magnetic field or infra red radiation
- Identify novel immune biomolecules involved in human performance optimization and enhance their activity to assist to reverse sleep deprivation, enhance cognition and performance

In the present study NK cells will be used as an immune model to examine the interaction of magnetic nanomaterials with the immune system and their response. The interactions will show the activation of various cytokines involved in immune cell responses. Secondly, the Natural Killer cells will be used to show how the magnetic nanomaterials are able to modulate the production of cytokines. The cytokines produced by NK cells help to activate other areas of the immune system (T cells) and are the first line of defense against viruses. The natural killer cells have been shown to decrease in times of sleep deprivation and stress such as wartime [136]. The decrease in the NK cell activity allows warfighters to become susceptible to stress conditions leading to a decrease in human performance and cognition. By modulating the immune production of cytokines the effects of stress and sleep deprivation on the warfighter's immune system can be reversed.

The basic aspect of this proposal is the fundamental study to know how magnetic nanomaterials affect the immune system when it is exposed to the materials. The applied aspect is to develop nanoparticles as immune cell modulators to increase human performance optimization efficiently during stressful conditions.

Air Force Relevance:

Air Force Pilots are expected to fly missions lasting 10-25 hours with mid air fueling, leading to extreme sleep deprivation. Many airmen also find sleep difficult under stressful wartime conditions leading to sleep deprivation. This sleep deprivation has an important impact on the health of these airmen. According to Gomez et al. [137] during intense training, the levels of natural killer cells decreased leading to an increase in respiratory infections [136]. Dimitrov et. al [138] also showed the effects of sleep on the immune system, they showed after sleep the levels of IL-12 were increased and the response of the immune system was greatly enhanced. IL-12 activates natural killer cells therefore these results also show that natural killer cells are increased with sleep. If more natural killer cells were activated the immune response would be left unchanged in times of sleep deprivation and airmen would be able to perform optimally. The effects of sleep deprivation on the immune system show reductions in biomolecules leading to reduction of warfighter performance optimization. Using a technique called magnetism based interaction capture; the expression of certain biomolecules can be enhanced leading to an increase in activation of the immune system and enhanced warfighter performance.

Approach:

Natural Killer Cells (NKC) are important in the innate immune response and specialize in killing stressful infected cells such as virus infected cells and abnormal growing cells. NK cells are large granular lymphocytes that do not express T cell receptors, or immunoglobulins. On the outside of NKCs is the ability to recognize MHC (Major histocompatibility complex) proteins and if a cell carries the MHC protein it is not killed by NKCs. Interleukin 12, which is produced by dendritic cells and macrophages activates Natural Killer cells. NKCs are also activated by several other cytokines such as gamma interferon. Using magnetic nanoprobe

the intracellular signaling pathway involved with activation of natural killer cells can be determined and the activation of the natural killer cells can be enhanced. By inducing a magnetic field the superparamagnetic nanoparticles will be drawn to the areas where the natural killer cells have been depleted and IL-12 is needed to activate the cells.

Based on previous research in sleep deprivation [136,139] NK cells were chosen as a cell model. NK cells were ordered from the ATCC (#CRL-2408) with IL-2 transfected in the cells, allowing for easier growth. The media used was minimum essential media without ribosomes, with the addition of 18 mg Inositol, 4.4 mg Folic acid, 2 mLs β -mercaptoethanol, 5 mL L-glutamine, 0.75 g sodium bicarbonate, 62.5 mL Horse serum, 62.5mL FBS normal. The cells were grown in 10 mL of media, which was changed every 2-3 days.

The magnetic nanoparticles will be synthesized as superparamagnetic iron oxide nanoparticles with a fluorescent tagging and silica shell. They will be linked with a molecule of interest to the NK cell receptor which will allow for binding and uptake into the cell. The uptake and binding will be measured with cytokine production. Synthesis of biofunctionalized nanomaterials will be conducted in collaboration with materials scientists.

- Uptake and translocation to the desired location into cells
 - The superparamagnetic nanoparticles will be added to the NK cells and their toxicity will be determined using MTT, LDH and ROS assays. After it is determined that the particles are non-toxic they will be linked with a molecule of interest to the NK cell receptors. By using a ligand the particles will be brought directly to the NK cells and their uptake can be measured using confocal microscopy.
- How engineered nanoparticles of different geometries interact with cells and their receptors.
 - The receptors involved in binding could be several receptors on the NK cell surface such as FcR, CD3 or killer cell lectin like receptor [137]. Particles of different size and geometry will be synthesized and used to determine, which binding receptors are able to bind the particles and activate different cytokines. As shown in figure 73, the NK cells have inhibitory and stimulatory receptors, which will have specific binding for the various geometries of particles to be used.

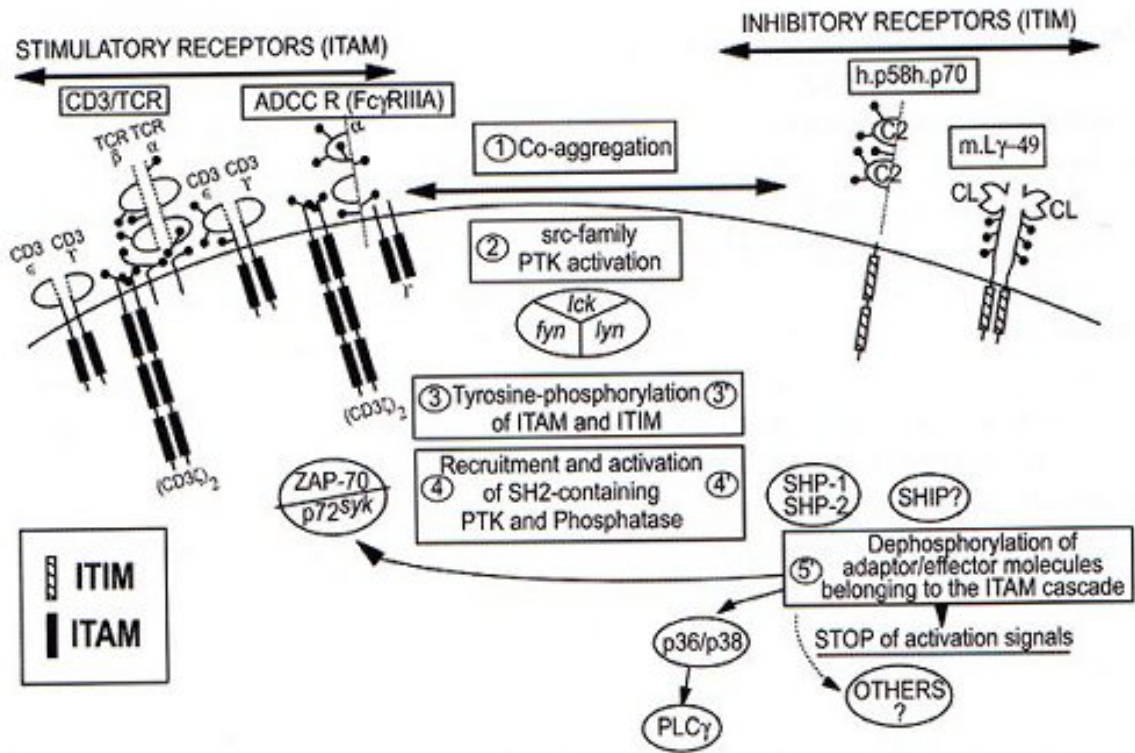


Figure 73. The stimulatory and inhibitory receptors on the surface of NK cells and the signaling pathways involved with their activation. *NeuroImmune Biology: Vol. 3: The Immune-Neuroendocrine Circuitry* [140].

- Molecular events involved in nanoparticle– membrane receptor binding, endocytosis and subsequent signaling activation
 - Endocytosis of the particles is possible through the FcR receptor as shown in figure 74. The particles could also possibly bind to the CD3 and Lectin like killer receptor [137]. After binding these receptors induce a signaling pathway which can be measured by the inflammatory response, gene expression and cytokine production.

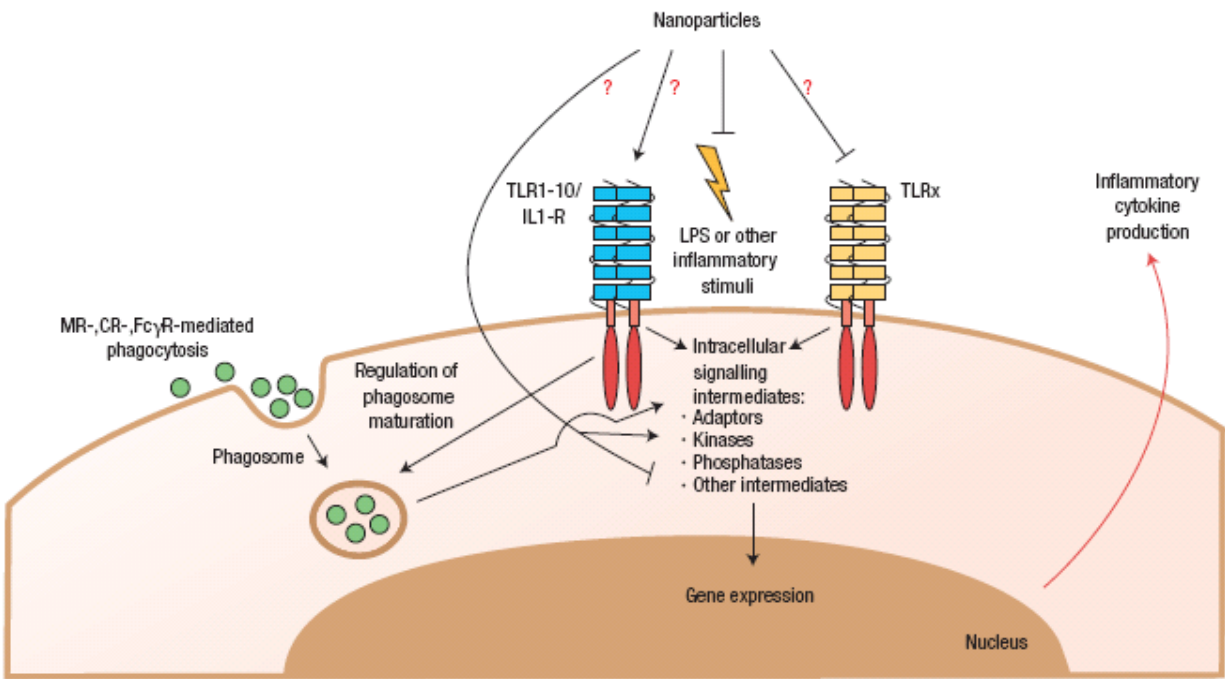


Figure 74. FcR receptor mediated phagocytosis and the effects on gene expression and inflammatory cytokine production. Nature, August 2007(2) 469-478 [141].

- Control or modulate immune molecular activity using biofunctionalized nanoparticles under the influence of electro-magnetic field or infra red radiation
 - By using the iron oxide superparamagnetic nanoparticles the binding of these particles to the NK cell receptors can be increased by induction of the magnetic field. The magnetic field will be able to guide the particles to the receptor leading to an increase in activity of NK cells and an increased cytokine response. The magnetic field will allow for the control of the immune cells and the ability to modulate them in times of stress and sleep deprivation.
- Identify novel immune biomolecules involved in human performance optimization and enhance their controlled activity to assist to reverse sleep deprivation, enhance cognition and performance.
 - IL-1, IL-6 and TNF-alpha are secreted by the immune cell macrophages which act inside the brain to create the stress response. In a study by Maier and Miller, it was found that by blocking these cytokines or the binding of them to the receptors the “stress or sick response” was stopped. If these cytokines were administered without any actual stress the individuals felt stressed without reason. The process works by IL-1 binding to the vagus nerve causing the brain to secrete its own IL-1 leading to the increase and thus the “sickness response.” Stress can trigger the same response, but instead of starting in the body the cytokines are released in the brain and cause the person to feel stress. By blocking the release of IL-1 the warfighters would feel more aware, less depressed and less anxious therefore increasing their cognition and performance [142].

REFERENCES

- [1] The Royal Society. (2004). Nanoscience and Nanotechnologies: Opportunities and Uncertainties. RS Policy document 19/04.
- [2] Kim, D., Zhang, Y., Voit, W., Rao, K., Kehr, J., Bjelke, B., and Muhammed, M. (2001). Superparamagnetic iron oxide nanoparticles for bio-medical applications. *Scripta Mater.* **44**, 1713-1717.
- [3] Murugan, R. and Ramakrishna, S. (2005). Development of nanocomposites for bone grafting. *Composites Sci. and Technol.* **65**, 2385-2406.
- [4] Sinha, V. and Trehan, A. (2003). Biodegradable microspheres for protein delivery. *J. Control. Release* **90**, 261-280.
- [5] Wu, Y., Yang, W., Wang, C., Hu, J., and Fu, S. (2005). Chitosan nanoparticles as a novel delivery system for ammonium glycyrrhizinate. *Int. J. Pharmaceutics* **295**, 235-245.
- [6] Kimbrell, G. (2006). Nanomaterials in Personal Care Products and FDA Regulation. The International Center for Technology Assessment. www.icta.org. 13 September 2006.
- [7] Ringer, S. and Ratinac, K. (2004). On the role of characterization in the design of interfaces in nanoscale materials technology. *Microsc. Microanal.* **10**, 324-335.
- [8] Wang, S., Young, R. S., Sun, N. N., Witten, M. L. (2002). In vitro cytokine release from rat type II pneumocytes and alveolar macrophages following exposure to JP-8 jet fuel in co-culture. *Toxicology* **173** (3), 211-219.
- [9] Ansoborlo, E., Henge-Napoli, M. H., Chazel, V., Gibert, R., Guilmette, R. A. (1999). Review and critical analysis of available in vitro dissolution tests. *Health Phys.* **77**(6), 638-645.
- [10] Zinderman, C. E., Conner, B., Malakooti, M. A., LaMar, J. E., Armstrong, A., Bohnker, B. K. (2004). Community-acquired methicillin-resistant *Staphylococcus aureus* among military recruits. *Emerg. Infect. Dis.* **10**(5), 941-944.
- [11] Ellsworth, D. K., Verhurst, D., Spitler, T. M., and Sabacky, B. J. (2000). Titanium nanoparticles move to the marketplace. *Chem. Innov.* **30**(12), 30-35.
- [12] Wold, A. (1993). Photocatalytic properties of TiO₂. *Chem. Mater.* **5**, 280-283.
- [13] Renwick, L. C., Brown, D., Clouter, A., and Donaldson, K. (2004). Increased inflammation and altered macrophage chemotactic responses caused by two ultrafine particle types. *Occup. Environ. Med.* **61**(5), 442-447.
- [14] Warheit, D. B., Webb, T. R., Sayes, C. M., Colvin, V. L., and Reed, K. L. (2006). Pulmonary instillation studies with nanoscale TiO₂ rods and dots in rats: toxicity is not dependent upon particle size and surface area. *Toxicol. Sci.* **91**(1), 227-236.
- [15] Grassian, V. H., O'Shaughnessy, P.T., Adamcakova-Dodd, A., Pettibone, J. M., Thorne, P. S. (2007). Inhalation exposure study of titanium dioxide nanoparticles with a primary particle size of 2 to 5 nm. *Environ. Health Perspect.* **115**(3), 397-402.
- [16] Sayes, C. M., Wahi, R., Kurian, P. A., Liu, Y., West, J. L., Ausman, K. D., Warheit, D. B., Colvin, V. L. (2006) Correlating nanoscale titania structure with toxicity: A cytotoxicity and inflammatory response study with human dermal fibroblasts and human lung epithelial cells. *Tox. Sci.* **92**(1), 174-185.
- [17] Gurr, J. R., Wang, A. S., Chen, C. H., and Jan, K. Y. (2005). Ultrafine titanium dioxide particles in the absence of photoactivation can induce oxidative damage to human bronchial epithelial cells. *Toxicology* **213**(1-2), 66-73.

- [18] Long, T. C., Saleh, N., Tilton, R. D., Lowry, G. V., and Veronesi B. (2006). Titanium dioxide (P25) produces reactive oxygen species in immortalized brain microglia (BV2): Implications for nanoparticle neurotoxicity. *Environ. Sci. Technol.* **40**(14), 4346-4352.
- [19] Bucher, J., Masten, S., Moudgil, B., Powers, K., Roberts, S., and Walker, N. (2004). Developing Experimental Approaches for the Evaluation of Toxicological Interactions of Nanoscale Materials. Final Workshop Report 3–4 November 2004, 1–37; University of Florida, Gainesville, FL.
- [20] Oberdörster, G., Oberdörster, E., and Oberdörster, J. (2005a). Nanotoxicology: An emerging discipline evolving from studies of ultrafine particles. *Environ. Health Perspect.* **113**, 823–839.
- [21] Oberdörster, G., Maynard, A., Donaldson, K., Castranova, V., Fitzpatrick, J., Ausman, K., Carter, J., Karn, B., Kreyling, W., Lai, D., et al. (2005b). Principles for characterizing the potential human health effects from exposure to nanomaterials: Elements of a screening strategy. *Particle Fibre Toxicol.* **2**, 8.
- [22] Nel, A., Xia, T., Mädler, L., and Li, N. (2006). Toxic potential of materials at the nanolevel. *Science* **311**(5761), 622-627.
- [23] Shukla, R., Bansal, V., Chaudhary, M., Basu, A., Bhonde, R. R., and Sastry, M. (2005). Biocompatibility of gold nanoparticles and their endocytotic fate inside the cellular compartment: A microscopic overview. *Langmuir*, **21**, 10644-10654.
- [24] Connor, E.E., Mwamuka, J., Gole, A., Murphy, C.J., and Wyatt, M.D. (2005). Gold nanoparticles are taken up by human cells but do not cause acute cytotoxicity. *Small.* **1** (3), 325-327.
- [25] Murphy, C. J., Gole, A. M., Hunyadi, S. E., and Orendorff, C. J. (2006). One-dimensional colloidal gold and silver nanostructures. *Inorg. Chem.* **45**(19), 7544-7554.
- [26] Pan Y, Neuss S, Leifert A, Fischler M, Wen F, Simon U, Schmid G, Brandau W, and Jähnen-Dechent W. (2007). Size-Dependent Cytotoxicity of Gold Nanoparticles. *Small.* **3** (11), 1941 – 1949.
- [27] Pernodet, N., Fang, X., Sun, Y., Bakhtina, A., Ramakrishnan, A., Sokolov, J., Ulman, A., and Rafailovich, M. (2006). Adverse effects of citrate/gold nanoparticles on human dermal fibroblasts. *Small.* **2**(6), 766-73.
- [28] Goodman, C. M., McCusker, C. D., Yilmaz, T., and Rotello, V. M. (2004). Toxicity of gold nanoparticles functionalized with cationic and anionic side chains. *Bioconjug Chem.* **15**(4), 897-900.
- [29] Roy, I., Ohulchanskyy, T., Bharali, D., Pudavar, H., Mistretta, R., Kaur, N., and Prasad, P. (2005). Optical tracking of organically modified silica nanoparticles as DNA carriers: A nonviral, nanomedicine approach for gene delivery. *PNAS* **102**, 279-284.
- [30] Csögör, Z. S., Nacken, M., Sameti, M., Lehr, C.-M. and Schmidt, H. (2003). Modified silica particles for gene delivery. *Materials Sci. Engin. C.* **23**, 93-97.
- [31] Hoet, P.H.M., Brueske-Hohlfeld, I., and Salata, O. (2004). Nanoparticles – known and unknown health risks. *J. Nanotox.* **2**, 1-2.
- [32] Wang, W., Gu, B., Liang, L., and Hamilton, W. (2003a). Fabrication of near infrared photonic crystals using highly-monodispersed submicrometer SiO₂ spheres. *J. Phys. Chem. B.* **107**, 12113-12117.
- [33] Wang, W., Gu, B., Liang, L., and Hamilton, W. (2003b). Fabrication of two- and three-dimensional silica nanocolloidal particle arrays. *J. Phys. Chem. B.* **107**, 3400–3404.

- [34] Donaldson, K., Stone, V., Tran, C. L, Kreyling, and Borm, P. J. A. (2004). Nanotoxicology. *Occup. Environ. Med.* **61**, 727-728.
- [35] Hardman, R. (2006). A toxicologic review of quantum dots: Toxicity depends on physicochemical and environmental factors. *Environ Health Persp.* **114**, 165-172.
- [36] Service, R. (2005). Calls rise for more research on toxicology of nanomaterials. *Science* **310**, 1609.
- [37] Vinardell, M. P. (2005). *In vitro* cytotoxicity of nanoparticles in mammalian germ-line stem cell. *Tox. Sci.* **88**, 285-286.
- [38] Zhou, Y. and Yokel, R. (2005). The chemical species of aluminum influence its paracellular flux and uptake into Caco-2 cells, a model of gastrointestinal absorption. *Tox. Sci.* **87**, 15-26.
- [39] Lam, C-W., James, J. T., McClustkey, R., and Hunter, R. (2004). Pulmonary toxicity of single-wall carbon nanotubes in mice 7 and 90 days after intratracheal instillation. *Tox. Sci.* **77**, 126-134.
- [40] Warheit, D. B., Laurence, B. R., Reed, K. L., Roach, D. H., Reynolds G. A. M., and Weff, T. R. (2004). Comparative pulmonary toxicity assessment of single-wall carbon nanotubes in rats. *Tox. Sci.* **77**, 117-125.
- [41] Lademann, J., Weigmann, H., Rickmeyer, C., Barthelmes, H., Schaefer, H., Mueller, G., and Sterry, W. (1999). Penetration of titanium dioxide microparticles in a sunscreen formulation into the horny layer and the follicular orifice. *Skin Pharmacol Appl.* **12**, 247-256.
- [42] Alt, V., Bechert, T., Steinrucke, P., Wagener, M., Seidel, P., Dingeldein, E., Domann, E., and Schnettler, R. (2004). An *in vitro* assessment of the antibacterial properties and cytotoxicity of nanoparticulate silver bone cement. *Biomaterials* **25**, 4383-4391.
- [43] Panacek, A., Kvitek, L., Prucek, R., Kolar, M., Vecerova, R., Pizurova, N., Sharma, V. K., Nevecna, T., and Zboril, R. (2006). Silver colloid nanoparticles: synthesis, characterization, and their antibacterial activity. *J. Phys. Chem. B Condens. Matter Mater. Surf. Interfaces. Biophys.* **110**, 16248-16253.
- [44] Lok, C. N., Ho, C. M., Chen, R., He, Q. Y., Yu, W. Y., Sun, H., Tam, P. K., Chiu, J. F., and Che, C. M. (2007). Silver nanoparticles: Partial oxidation and antibacterial activities. *J. Biol. Inorg. Chem.* **12**(4), 527-534.
- [45] Hussain, S., Meneghini, E., Moosmayer, M., Lacotte, D., and Anner, B. M. (1994). Potent and reversible interaction of silver with pure Na,K-ATPase and Na,K-ATPase-liposomes. *Biochim. Biophys. Acta* **1190**, 402-408.
- [46] Hussain, S. M., Hess, K. L., Gearhart, J. M., Geiss, K. T., and Schlager, J. J. (2005). *In vitro* toxicity of nanoparticles in BRL 3A rat liver cells. *Toxicol. In Vitro* **19**, 975-983.
- [47] Braydich-Stolle, L., Hussain, S., Schlager, J. J., and Hofmann, M. C. (2005). *In vitro* cytotoxicity of nanoparticles in mammalian germline stem cells. *Toxicol. Sci.* **88**, 412-419.
- [48] Colvin, V. L. (2003). The potential environmental impact of engineered nanomaterials. *Nat. Biotechnol.* **21**:1166-1170.
- [49] Foley, S., Crowley, C., Smaih, M., Bonfils, C., Erlanger, B. F., Seta, P., and Larroque, C. (2002). Cellular localisation of a water-soluble fullerene derivative. *Biochem. Biophys. Res. Commun.* **294**, 116-119.

- [50] Jani, P., Halbert, G. W., Langridge, J., and Florence, A. T. (1990). Nanoparticle uptake by the rat gastrointestinal mucosa: Quantitation and particle size dependency. *J. Pharm. Pharmacol.* **42**, 821-826.
- [51] Lipscomb, M. F. (1989). Lung defenses against opportunistic infections. *Chest* **96**, 1393-1399.
- [52] Lee, K. P., Trochimowicz, H. J., and Reinhardt, C. F. (1985). Pulmonary response of rats exposed to titanium dioxide (TiO₂) by inhalation for two years. *Toxicol. Appl. Pharmacol.* **79**, 179-192.
- [53] Brown, D. M., Wilson, M. R., MacNee, W., Stone, V., and Donaldson, K. (2001). Size-dependent proinflammatory effects of ultrafine polystyrene particles: a role for surface area and oxidative stress in the enhanced activity of ultrafines. *Toxicol. Appl. Pharmacol.* **175**, 191-199.
- [54] Muller, M., Mackeben, S., and Muller-Goymann, C. C. (2004). Physicochemical characterisation of liposomes with encapsulated local anaesthetics. *Int. J. Pharm.* **274**, 139-148.
- [55] Hardman, S., Cope, A., Swann, A., Bell, P. R., Naylor, A. R., and Hayes, P. D. (2004). An in vitro model to compare the antimicrobial activity of silver-coated versus rifampicin-soaked vascular grafts. *Ann. Vasc. Surg.* **18**(3), 308-313.
- [56] Lansdown, A. B. (2006). Silver in health care: Antimicrobial effects and safety in use. *Curr. Probl. Dermatol.* **33**, 17-34.
- [57] Heggers, J., Goodheart, R. E., Washington, J., McCoy, L., Carino, E., Dang, T., Edgar, P., Maness, C., and Chinkes, D. (2005). Therapeutic efficacy of three silver dressings in an infected animal model. *J. Burn Care Rehabil.* **26**(1), 53-56.
- [58] Davenport, K. and Keeley, F. X. (2005). Evidence for the use of silver-alloy-coated urethral catheters. *J. Hosp. Infect.* **60**(4), 298-303.
- [59] Sun, R. W., Chen, R., Chung, N. P., Ho, C. M., Lin, C. L., and Che, C. M. (2005). Silver nanoparticles fabricated in Hepes buffer exhibit cytoprotective activities toward HIV-1 infected cells. *Chem. Commun. (Camb)*. **40**, 5059-5061.
- [60] Kim, J. S., Kuk, E., Yu, K. N., Kim, J. H., Park, S. J., Lee, H. J., Kim, S. H., Park, Y. K., Park, Y. H., Hwang, C. Y., Kim, Y. K., Lee, Y. S., Jeong, D. H., and Cho, M. H. (2007). Antimicrobial effects of silver nanoparticles. *Nanomedicine* **3**(1), 95-101.
- [61] Valko, M., Morris, H., and Cronin, M. (2005). Metals, toxicity and oxidative stress. *Curr. Med. Chem.* **12**(10), 1161-1208.
- [62] Liu, Y., Li, J., Qiu, X., and Burda, C. (2006). Novel TiO₂ nanocatalysts for wastewater purification: tapping energy from the sun. *Water Sci. Technol.* **54**(8), 47-54.
- [63] Murdock, R. C., Braydich-Stolle, L., Schrand, A.M., Schlager, J.J., and Hussain, S.M. (2007). Characterization of nanomaterial dispersions in solution prior to in vitro exposure using dynamic light scattering technique. *Toxicol. Sci.* (Epub ahead of print).
- [64] Elechiguerra, J. L., Burt, J. L., Morones, J. R., Camacho-Bragado, A., Gao, X., Lara, H. H., and Yacaman, M. J. (2005). Interaction of silver nanoparticles with HIV-1. *J. Nanobiotechnol.* **3**, 6.
- [65] Samuel, U. and Guggenbichler, J. P. (2004). Prevention of catheter-related infections: The potential of a new nano-silver impregnated catheter. *Int. J. Antimicrob. Agents.* **23** Suppl 1, S75-S78.

- [66] Percival, S. L., Bowler, P. G., and Dolman, J. (2007). Antimicrobial activity of silver-containing dressings on wound microorganisms using an *in vitro* biofilm model. *Int. Wound J.* **4**(2), 186-191.
- [67] Vigneshwaran, N., Kathe, A. A., Varadarajan, P. V., Nachane, R. P., and Balasubramanya, R. H. (2007). Functional finishing of cotton fabrics using silver nanoparticles. *J. Nanosci. Nanotechnol.* **7**(6), 1893-1897.
- [68] Cioffi, N., Ditaranto, N., Torsi, L., Picca, R. A., De Giglio, E., Sabbatini, L., Novello, L., Tantillo, G., Bleve-Zacheo, T., and Zambonin, P. G. (2005). Synthesis, analytical characterization and bioactivity of Ag and Cu nanoparticles embedded in poly-vinyl-methyl-ketone films. *Anal. Bioanal. Chem.* **382**(8), 1912-1918.
- [69] Pryor, J. L., Hughes, C., Foster, W., Hales, B. F., and Robaire, B. (2000). Critical windows of exposure for children's health: The reproductive system in animals and humans. *Environ. Health Perspect.* **108**(S3), 491-503.
- [70] Dym, M. and Fawcett, D. (1970). The blood-testis barrier in the rat and the physiological compartmentation of the seminiferous epithelium. *Biol. Reprod.* **3**, 308-326.
- [71] Setchell, B. P. (1967). The blood-testicular fluid barrier in sheep. *J. Physiol.* **189**(Suppl), 63P-65P.
- [72] Setchell, B. P., Voglmayr, J. K., and Waites, G. M. H. (1969). A blood-testis barrier restricting passage from blood into rete testis fluid but not into lymph. *J. Physiol.* **200**, 73-85.
- [73] Setchell, B. P and Waites, G. M. H. (1975). Male reproductive system. In Section 7: Handbook of Physiology (American Physiology Society), Washington DC.
- [74] Setchell, B. P. (1970). The testis: Testicular blood supply, lymphatic drainage and secretion of fluid. In Book Title (book editors), pp. 101-239, Academic Press, New York.
- [75] Setchell, B. P. (1978). The mammalian testis. Cornell University Press, London.
- [76] Kim, J. S., Yoon, T. J., Yu, K. N., Kim, B. G., Park, S. J., Kim, H. W., Lee, K. H., Park, S. B., Lee, J. K., and Cho, M. H. (2006). Toxicity and tissue distribution of magnetic nanoparticles in mice. *Toxicol. Sci.* **89**, 338-347.
- [77] Braydich-Stolle, L., Hussain, S., Schlager, J., and Hofmann, M. C. (2005). **In vitro** cytotoxicity of nanoparticles in mammalian germ-line stem cells. *Toxicol. Sci.* **88**, 412-419.
- [78] Meng, X., Lindahl, M., Hyvonen, M. E., Parvinen, M., de Rooij, D. G., Hess, M. W., Raatikainen-Ahokas, A., Sainio, K., Rauvala, H., Lakso, M., Pichel, J. G., Westphal, H., Saarma, M., and Sariola, H. (2000). Regulation of cell fate decision of undifferentiated spermatogonia by GDNF. *Science* **287**(5457), 1489-1493.
- [79] Kanatsu-Shinohara, M., Ogonuki, N., Inoue, K., Miki, H., Ogura, A., Toyokuni, S., and Shinohara, T. (2003). Long-term proliferation in culture and germline transmission of mouse male germline stem cells. *Biol. Reprod.* **69**, 612-619.
- [80] Kubota, H., Avarbock, M. R., and Brinster, R. L. (2004). Growth factors essential for self-renewal and expansion of mouse spermatogonial stem cells. *Proc. Natl. Acad. Sci. U. S. A.* **101**, 16489-16494.
- [81] Hofmann, M. C., Braydich-Stolle, L., and Dym, M. (2005). Isolation of male germ line stem cells; influence of GDNF. *Dev. Biol.* **279**, 114-124.
- [82] Braydich-Stolle, L., Kostereva, N., Dym, M., and Hofmann, M. C. (2007). Role of Src family kinases and N-Myc in spermatogonial stem cell proliferation. *Dev. Biol.* **304**(1), 34-45.

- [83] Lee, J., Kanatsu-Shinohara, M., Inoue, K., Ogonuki, N., Miki, H., Toyokuni, S., Kimura, T., Nakano, T., Ogura, A., and Shinohara, T. (2007). Akt mediates self-renewal division of mouse spermatogonial stem cells. *Development* **134**(10), 1853-1859.
- [84] Oatley, J. M., Avarbock, M. R., and Brinster, R. L. (2007). Glial cell line-derived neurotrophic factor regulation of genes essential for self-renewal of mouse spermatogonial stem cells is dependent on Src family kinase signaling. *J. Biol. Chem.* **282**(35), 25842-25851.
- [85] You, C. C., De, M., and Rotello, V. M. (2005). Monolayer-protected nanoparticle-protein interactions. *Curr. Opinion Chem. Biol.* **9**(6), 639-646.
- [86] Wilhelm, C., Billotey, C., Roger, J., Pons, J. N., Bacri, J.-C., and Gazeau, F. (2003). Intracellular uptake of anionic Superparamagnetic nanoparticles as a function of their surface coating. *Biomaterials* **24**(6), 1001-1011.
- [87] Hoshino, A., Kujioka, F., Oku, T., Suga, M., Sasaki, Y. F., Ohta, T., Yasuhara, M., Suzuki, K., and Yamamoto, K. (2004). Physicochemical properties and cellular toxicity of nanocrystals quantum dots depend on their surface modification. *Nano Lett.* **4**(11), 2163-2169.
- [88] Chen, C., Xing, G., Wang, J., Zhao, Y., Li, B., Tang, J., Jian, G., Wang, T., Sun, J., Xing, L., Yuan, H., Gao, Y., Meng, H., Chen, Z., Zhao, F., Chai, Z., and Fang, X. (2005). Multi-hydroxylated $[\text{Gd}@\text{C}_{82}(\text{OH})_{22}]_n$ nanoparticles: Antineoplastic activity of high efficiency and low toxicity. *Nano Lett.* **5**(10), 2050-2057.
- [89] Gupta, A. K. and Gupta, M. (2005). Synthesis and surface engineering of iron oxide nanoparticles for biomedical applications. *Biomaterials* **26**, 3995-4021.
- [90] Lesniak, W., Bielinska, A. U., Sun, K., Janczak, K. W., Shi, X., Baker, J. R., Jr., and Balogh, L. P. (2005). Silver/dendrimer nanocomposites as biomarkers: Fabrication, characterization, in vitro toxicity, and intracellular detection. *Nano Lett.* **5**(11), 2123-2130.
- [91] Dumortier, H., Lacotte, S., Pastorin, G., Marega, R., Wu, W., Bonifazi, D., Brian J.-P., Prato, M., Muller, S., and Bianco A. (2006). Functionalized carbon nanotubes are non-cytotoxic and preserve the functionality of primary immune cells. *Nano Lett.* **6**(7), 1522-1528.
- [92] Lemarchand, C., Gref, R., Lesieur, S., Hommel, H., Vacher, B., Besheer, A., Maeder, K., and Couvreur, P. (2005). Physico-chemical characterization of polysaccharide-coated nanoparticles. *J. Control. Release* **108**(1), 97-111.
- [93] Wang, X. and Li, Y. (2007). Monodisperse nanocrystals: General synthesis, assembly, and their applications. *Chem. Commun.* **2007**, 2901-2910.
- [94] Sun, Y. and Xia, Y. (2002). Shape-controlled synthesis of gold and silver nanoparticles. *Science* **298**(5601), 2176-2179.
- [95] Chen, J., McLellan, J.M., Siekkinen, A., Xiong, Y., Li, Z.-Y., Xia, Y. (2006). Facile synthesis of gold-silver nanocages with controllable pores on the surface. *J. Am. Chem. Soc.* **128**(46), 14776-14777.
- [96] Stone, J. W., Sisco, P. N., Goldsmith, E. C., Baxter, S. C., and Murphy, C. J. (2007). Using gold nanorods to probe cell-induced collagen deformation. *Nano Lett.* **7**(1), 116-119.
- [97] Wiley, B., Sun, Y., and Xia, Y. (2007). Synthesis of silver nanostructures with controlled shapes and properties. *Acc. Chem. Res.* **40**(10), 1067-1076.

- [98] Du, J., Han, B., Liu, Z., and Liu, Y. (2007). Control synthesis of silver nanosheets, chainlike sheets, and microwires via a simple solvent–thermal method. *Cryst. Growth Des.* **7**(5), 900-904.
- [99] Wiley, B., Herricks, T., Sun, Y., and Xia, Y. (2004). Polyol synthesis of silver nanoparticles: Use of chloride and oxygen to promote the formation of single-crystal, truncated cubes and tetrahedrons. *Nano Lett.* **4**(10), 2057.
- [100] Wiley, B. J., Chen, Y., McLellan, J. M., Xiong, Y., Li, Z-Y., Ginger, D., Xia, Y. (2007). Synthesis and optical properties of silver nanobars and nanorice. *Nano Lett.* **7**(4), 1032-1036.
- [101] Xiong, Y., Cai, H., Wiley, B. J., Wang, J., Kim, M. J., and Xia, Y. (2007). Synthesis and mechanistic study of palladium nanobars and nanorods. *J. Am. Chem. Soc.* **129**(12), 3665-3675.
- [102] Fang, J., You, H., Kong, P., Yi, Y., Song, X., and Ding, B. (2007). Dendritic silver nanostructure growth and evolution in replacement reaction. *Cryst. Growth Des.* **7**(5), 864-867.
- [103] Narayan, A., Landstrom, L., and Boman, M. (2003). Laser-assisted synthesis of ultra small metal nanoparticles. *Appl. Surf. Sci.* **208**, 137-141
- [104] Song, H., Rioux, R. M., Hoefelmeyer, J. D., Komor, R., Niesz, K., Grass, M., Yang, P., and Somorjai, G.A. (2006). Hydrothermal growth of mesoporous SBA-15 silica in the presence of PVP-stabilized Pt nanoparticles: synthesis, characterization, and catalytic properties. *J. Am. Chem. Soc.* **128**(9), 3027-3037.
- [105] Wang, C.C., Chen, D. H., and Huang, T. C. (2001). Synthesis of palladium nanoparticles in water-in-oil microemulsions. *Colloids Surf. A.* **189**(1-3), 145-154.
- [106] Nadagouda, M. N. and Varma, R. S. (2006). Green and controlled synthesis of gold and platinum nanomaterials using vitamin B2: Density-assisted self-assembly of nanospheres, wires, and rods. *Green Chem.* **8**, 516-518.
- [107] Raveendran, P., Fu, J., and Wallen, S. L. (2003). *J. Am. Chem. Soc.* **125**, 13940.
- [108] Nadagouda, M. N. and Varma, R. S. (2007). Green approach to bulk and template-free synthesis of thermally stable reduced polyaniline nanofibers for capacitor applications. *Green Chem.* **9**, 632.
- [109] Naik, R. R., S. J. Stringer, Agarwal, G., Jones, S. E., and Stone, M. O. (2002). Biomimetic synthesis and patterning of silver nanoparticles. *Nature Mater.* **1**, 169-172.
- [110] Nadagouda, M. N. and Varma, R. S. (2007). Preparation of novel metallic and bimetallic cross-linked poly (vinyl alcohol) nanocomposites under microwave irradiation. *Macromol. Rapid Commun.* **28**(4), 465-472.
- [111] Nadagouda, M. N. and Varma, R. S. (2007). Synthesis of thermally stable carboxymethyl cellulose/metal biodegradable nanocomposite films for potential biological applications. *Biomacromolecules* **8**, 2762-2767.
- [112] Nadagouda, M. N. and Varma, R. S. (2007). A greener synthesis of core (Fe, Cu)-shell (Au, Pt, Pd, and Ag) nanocrystals using aqueous Vitamin C. *Cryst. Growth Des.* **7**(12), 2582-2587.
- [113] Nadagouda, M. N. and Varma, R. S. (2007). Microwave-assisted shape-controlled bulk synthesis of noble nanocrystals and their catalytic properties. *Cryst. Growth Des.* **7**(4), 686-690.

- [114] Nadagouda, M. N. and Varma, R. S. (2007). Microwave-assisted shape-controlled bulk synthesis of Ag and Fe nanorods in poly(ethylene glycol) solutions. *Cryst. Growth Des.* **8**(1), 291-295.
- [115] Dahl, J. A., Maddux, L. S., and Hutchison, J. E. (2007). Toward greener nanosynthesis. *Chem. Rev.* **107**(6), 2228-2269.
- [116] Kumar, A., Vemula, P. K. Ajayan, P. M., and John, G. (2008). Silver nanoparticles embedded anti-microbial paints based on vegetable oil. *Nat. Mater.* **7**, 236-241.
- [117] Anastas, P.T. and Warner, J.C. (1998). *Green Chemistry: Theory and Practice*; Oxford University Press Inc., New York.
- [118] Nadagouda, M. N. and Varma, R. S. (2008). Green synthesis of silver and palladium nanoparticles at room temperature using coffee and tea extract. *Green Chem.* **10**, 859-862.
- [119] Hernandez-Sanchez, B.A., Boyle, T.J., Lambert, T.N., Daniel-Taylor, S.D. (2006). *IEEE T. Nanobiosci.* **5**.
- [120] Gu, M., Yuan, X., Kang, C., Zhao, Y., Tian, N., Pu, P., and Shengy J. (2007). Surface biofunctionalization of PLA nanoparticles through amphiphilic polysaccharide coating and ligand coupling: Evaluation of biofunctionalization and drug releasing behavior. *Carbohydr. Polym.* **67**, 417-426.
- [121] Kumar, S., Harrison, N., Richards-Kortum, R., and Sokolov, K. (2007). Plasmonic nanosensors for imaging intracellular biomarkers in live cells. *Nano Lett.* **7**, 1338-1343.
- [122] www.sharperimage.com
- [123] Alt, V., Bechert, T., Steinrucke, P., Wagener, M., Seidel, P., Dingeldein, E., Domann, E., and Schnettler, R. (2004). *Biomaterials* **25**(18), 4383.
- [124] Georgia Institute of Technology, Copyright 2006 NNIN-1025, <http://www.nnin.org/doc/NNIN-1025.pdf>.
- [125] Hogan, H. (2008). Socks with Nanosilver could present problems. *Nanophotonics*, June 2008.
- [126] Carlson, C., Hussain, S., Schrand, A., Braydich-Stolle, L., Hess, K., Rochelle, J., Schlager, J. (200x). Unique cellular interaction of silver nanoparticles: Size dependent generation of reactive oxygen species. *J. Phys. Chem. B* **112**(43), 13608-13619.
- [127] Morones J. R., Elechiguerra, J. L., Camacho, A., Holt, K., Kouri, J. B., Ramirez, J. T., and Yacaman, M. J. (2005). The bactericidal effect of silver nanoparticles. *Nanotechnology* **16**(10), 2346-2353.
- [128] Schrand, A. M., Braydich-Stolle, L. K., Schlager, J. J., Dai, L., and Hussain, S. M. (2008). Can silver nanoparticles be useful as potential biological labels? *Nanotechnology* **19**, 235104-235117.
- [129] Fan, S., Chapline, M. G., Franklin, N. R., Tombler, T. W., Cassell, A.M., and Dai, H. (1999). Self-oriented regular arrays of carbon nanotubes and their field emission properties. *Science* **283**, 512-514.
- [130] Wong, S. S., Joselevich, E., Woolley, A. T., Cheung, C. L., and Lieber, C. M. (1998). Covalently functionalized nanotubes as nanometre-sized probes in chemistry and biology. *Nature* **394**, 52-55.
- [131] Yao, Z., Postma, H.W.C., Balents, L., and Dekker, C. (1999). Carbon nanotube intramolecular junctions. *Nature* **402**, 273-276.
- [132] Shvedova A., Castranova, V., Kisin, E., Schwegler-Berry, D., Murray, A., Gandelsman, V., Maynard, A., and Baron, P. (2003). Exposure to carbon nanotube material: assement

- of cytotoxicity using human keratinocyte cells. *J. Toxicol. Environ. Health, Part A*. **66**, 1909-1926.
- [133] Hu, H., Ni, Y., Montana, V., Haddon, R. C., and Parpura, V. (2004). Chemically functionalized carbon nanotubes as substrates for neuronal growth. *Nano Lett.* **4**(3), 507–511.
 - [134] Elias, K.L., Price, R.L., and Webster, T.J. (2002). Enhanced functions of osteoblasts on nanometer diameter carbon fibers. *Biomater.* **23**, 3279-3287.
 - [135] Grabinski C., Hussain, S., Lafdi, K., Braydich-Stolle, L., Schlager, J. (2007). Effect of particle dimension on biocompatibility of carbon nanotubes. *Carbon* **45**, 2828-2835.
 - [136] Quade, G, PhD. Hairy cell Leukemia, National Cancer Institute. www.meb.uni-bonn.de/cancer.gov/CDR0000258013.html.
 - [137] Gomez-Merino, D., Drogou, C., Chennaoui, M., Tiollier, E., Mathieu, J., and Guezennec, C. Y. (2005). Effects of combined stress during intense training on cellular immunity, hormones and respiratory infections. *Neuroimmunomodulat.* **12**(3), 164-172.
 - [138] Dimitrov, S., Lange, T., Nohroudi, K., and Born J. (2007). Number and function of circulating human antigen presenting cells regulated by sleep. *Sleep* **30**(4), 401-411.
 - [139] Delves, P. J. and Roitt, I. M. (2000). The immune system- First of two parts. *New Engl. J. Med.* **343**, 37-49.
 - [140] Beczi, I. and Szentivanyi, A. (eds). (2006). *NeuroImmune Biology: Vol. 3: The Immune-Neuroendocrine Circuitry: History and Progress*. Elsevier Science, ISBN:0-444-50851-1.
 - [141] Dobrovolskaia, M.A. and McNeil, S.E. (2007). Immunological properties of engineered nanomaterials. *Nature* **2**, 469-478.
 - [142] Maier, S. and Miller, N. Lecture at APA's 2001 Annual Convention.
 - [143] Malvern Instruments Ltd. (2005). Zetasizer Nano Series User Manual. MAN0317 Issue 2.2. Worcestershire, UK.
 - [144] Skebo, J.E, Grabinski, C.M., Schrand, A.M., Schlager, J.J., and Hussain, S.M. (2007). Assessment of metal nanoparticle agglomeration, uptake, and interaction using high-illuminating system. *Int. J. Toxicol.* **26**(2), 135-141.
 - [145] Wagner, A.J., Bleckmann, C.A., Murdock, R.C., Schrand, A.M., Schlager, J.J., and Hussain, S.M. (2007). Cellular interaction of different forms of aluminum nanoparticles in rat alveolar macrophages. *J. Phys. Chem. B* **111**(25), 7353-7359.
 - [146] Gómez-Lechón, M. J., O'Connor, E., Castell, J. V., and Jover, R. (2002). Sensitive markers used to identify compounds that trigger apoptosis in cultured hepatocytes. *Tox. Sci.* **65**(2), 299-308.
 - [147] Lennon, S., Martin, S., and Cotter, T. (1991). Dose-dependent induction of apoptosis in human tumour cell lines by widely diverging stimuli. *Cell. Prolif.* **24**(2), 203-214.
 - [148] McCabe, Jr. (2003). Mechanisms and consequences of silica-induced apoptosis. *Tox. Sci.* **76**, 1-2.

ABBREVIATIONS

A549	Human alveolar epithelial cell-line
Ag	Silver
Al	Aluminum
Al ₂ O ₃	Aluminum oxide
ANOVA	One-way Analysis of Variance
ASC	Aeronautical System Center
ATCC	American Type Culture Collection
Au	Gold
BDAC	Benzyldimethylhexadecylammonium chloride
BIN	Biological Interactions of Nanomaterials
C18-4 cell line	Transfected type A Spermatogonia with large T antigen gene
C ₆₀	Fullerene
CN _x -MWCNT	MWCNT doped with nitrogen
CO ₂	Carbon dioxide
CO _x -MWCNTs	MWCNT functionalized with carbonyl groups
CTAB	Hexadecyltrimethylammonium bromide
DCFH-DA	2',7'-Dichlorodihydrofluorescein diacetate
DLS	Dynamic light scattering
DMEM/Ham's F-12	Dulbecco's modified Eagle's medium/Nutrient F-12 Ham's media
EDAX	Energy dispersive analysis using x-ray
EDTA	Ethylenediaminetetraacetic acid

ESH	Environmental, Safety and Health
FBS	Fetal bovine serum
FFT	Fast fourier transform
FNM	Functionalize nanomaterial
GDNF	Glial cell line-derived neurotrophic factor
HaCaT	Human keratinocyte cell-line
HEM	HaCaT exposure media
HBSS	Hank's balanced salt solution
HC	Hydrocarbon
HEL-30	Mouse keratinocyte cell-line
hFOB	Human fetal osteoblasts
HRP	Horseradish peroxidase
IL-1 β , IL-1, IL-6	Pro-inflammatory cytokines
LDH	Lactate dehydrogenase
LDV	Laser doppler velocimetry
MAC	Rat alveolar macrophage cell-line
MEM	Macrophage exposure media
MHC	Major histocompatibility complex
mL	Milliliter
MMP	Mitochondrial membrane potential
MRSA	Methicillin-resistant Staphylococcus aureus
MTS	3-(4,5-dimethylthiazol-2-yl)- 5-(3-carboxymethonyphenol)-2-(4-sulfophenyl)-2H-tetrazolium

MURI	Multidisciplinary Research Initiative
MWCNT	Multi-walled carbon nanotubes
N	Normal
NKC	Natural killer cells
ng	Nanogram
nm	Nanometer
NP	Nanoparticle
OA	Oleic acid
OD	Optical density
PBS	Phosphate buffered saline
PCR	Polymerase chain reaction
Pen/strep	Penicillin/streptomycin
PES	Phenazine ethosulfate
PS	Polysaccharide
RET	Rearranged during transfection
ROS	Reactive oxygen species
SD	Standard deviation
SEM	Scanning electron microscopy
SFK	Src family kinase
SiO ₂	Silicon dioxide (Silica)
STEM	Scanning transmission electron microscopy
SWCNT	Single-walled carbon nanotubes
TEM	Transmission electron microscopy

TiO ₂	Titanium dioxide
TNF α	Pro-inflammatory cytokines
U937	Human alveolar macrophage cell-line
UC	Uncoated
UV	Ultra-violet
XPS	X-ray photoelectron spectroscopy
XRD	X-ray diffraction
ZnO	Zinc oxide
μ L	Microliter
μ m	Micrometer